**Dissertation zur Erlangung des Doktorgrades**
**der Fakultät fuer Chemie und Pharmazie**
**der Ludwig-Maximilians-Universität Muechen**

# Regulation of endolysosomal Two-Pore-Channel activity by the Calcium-Caffeine-Zinc sensitivity Protein (CCZ1)


Zhuo Yang
aus
Dandong, Liaoning, China
2025

# Erklärung

Diese Dissertation wurde im Sinne von §7 der Promotionsordnung vom 28. November 2011 von Herrn Prof. Dr. Martin Biel betreut.

# Eidesstattliche Versicherung

Diese Dissertation wurde eigenständig und ohne unerlaubte Hilfe erarbeitet.

München, 22.09.2025 .

Zhuo Yang

Dissertation eingereicht am 24.06.2025

Erstgutachter: Prof. Dr. Martin Biel

Zweitgutachter: Prof. Dr. Susanne Koch

Mündliche Prüfung am 16.09.2025

# Abstract

TPC2 (Two-Pore Channel 2) is a cation channel passing $Na^+$ and $Ca^{2+}$ that is primarily localized on late endosomes and lysosomes. It is activated by the endogenous second messengers $PI(3,5)P_2$ and NAADP, whose levels are modulated by various cellular stimuli. Dysregulation of TPC2 has been implicated in multiple disorders and pathological processes, including Alzheimer's disease, Parkinson's disease, non-alcoholic fatty liver disease and the migration of cancer cells. Both genetic ablation and pharmacological inhibition of TPC2 have demonstrated therapeutic benefits in disease models. So far, only a few proteins, including mTORC1, OCaR1 and Rab7a, have been shown to affect TPC2 activity. Moreover, it remains to be studied whether these proteins directly bind to the channel or affect channel activity via indirect pathways.

This study aimed at identifying novel TPC2 regulatory proteins and delineating their contributions to TPC2-mediated pathological processes. Using various cancer cell lines, CRISPR-Cas9–mediated gene ablation, lysosomal patch-clamp recordings, FRET-based assays, and other techniques, Rab7a-mediated enhancement of TPC2 channel activity was confirmed, and a novel and essential role of CCZ1 in facilitating this interaction was uncovered. Notably, even constitutively active Rab7a[QL] failed to potentiate TPC2 activity in the absence of CCZ1, suggesting that CCZ1 has other impacts on TPC2 function rather than simply acting through Rab7a.

Further characterization of TPC2 in *CCZ1* deficient cells revealed markedly increased channel efficacy, a left-shifted EC50 for $PI(3,5)P_2$, and the emergence of voltage dependence. Moreover, specific TPC2 activation by the synthetic TPC2 agonist TPC2-A1P elicited stronger migration and proliferation responses in *CCZ1* knockout (KO) SK-MEL5 cells relative to wild-type (WT) cells, corroborating the increased sensitivity and maximal current response in the KO cells.

Taken together, CCZ1 was identified as a novel regulatory protein for TPC2, whose loss significantly enhances TPC2 function and sensitivity to its agonists, thereby promoting more aggressive cancer cell migration and proliferation. These results advance the understanding of the complex regulatory landscape of TPC2 and suggest that targeting the TPC2–CCZ1 axis could offer new opportunities for therapeutic intervention in TPC2-related diseases.

# Zusammenfassung

TPC2 (Two-Pore Channel 2) ist ein $Na^+$ und $Ca^{2+}$ permeabler Kationenkanal, der vorwiegend in späten Endosomen und Lysosomen lokalisiert ist. Er wird durch die endogenen second Messenger $PI(3,5)P_2$ und NAADP aktiviert, deren zelluläre Konzentrationen durch verschiedene Stimuli reguliert werden. Eine Fehlregulation von TPC2 ist in mehrere Erkrankungen und pathologische Prozesse involviert, darunter die Alzheimer-Krankheit, die Parkinson-Krankheit, die nicht-alkoholische Fettleber-erkrankung sowie die Migration von Krebszellen. Sowohl die genetische Inaktivierung als auch die pharmakologische Hemmung von TPC2 haben in murinen Krankheitsmodellen vielversprechende therapeutische Effekte gezeigt. Ob TPC2 über $PI(3,5)P_2$ und NAADP hinaus von anderen zellulären Molekülen, insbesondere von Proteinen reguliert werden kann, ist weitgehend unerforscht. Bisher ist nur von wenigen Proteinen (z.B. mTORC1, OCaR1 und Rab7a) bekannt, dass sie die Aktivität von TPC2 beeinflussen. Es bleibt jedoch in den meisten Fällen offen, ob diese Regulation aus einer direkten Bindung an den Kanal resultiert oder indirekt vermittelt ist.

In der vorliegenden Studie wurde das Ziel verfolgt, neue regulatorische Proteine von TPC2 zu identifizieren und deren Beitrag zu TPC2-vermittelten pathologischen Prozessen zu untersuchen. Mithilfe verschiedener Krebszelllinien, durch CRISPR-Cas9-vermittelte Gen-Ausschaltung, lysosomale Patch-Clamp-Messungen, FRET-basierte Assays und andere Methoden konnte die durch Rab7a vermittelte Verstärkung der TPC2-Kanalaktivität bestätigt werden und eine essenzielle Rolle von CCZ1 für diese Interaktion gezeigt werden. Bemerkenswerterweise konnte selbst die konstitutiv aktive Rab7a[QL] Mutante TPC2 Ströme nicht in Abwesenheit von CCZ1

verstärken, was darauf hindeutet, dass CCZ1 zusätzliche Auswirkung auf die TPC2-Funktion hat, anstatt ausschließlich über Rab7a zu wirken.

Eine weiterführende Charakterisierung von TPC2 in *CCZ1* defizienten Zellen zeigte eine deutlich gesteigerte Kanalaktivität, eine nach links verschobene EC50 für $PI(3,5)P_2$ und das Auftreten einer Spannungsabhängigkeit. Darüber hinaus führte die spezifische Aktivierung von TPC2 durch den synthetischen TPC2 Agonisten A1P in *CCZ1* Knockout (KO) SK-MEL5 Zellen zu stärkerer Migration und Proliferation im Vergleich zu Wildtyp-Zellen, was in Übereinstimmung mit einer erhöhten Sensitivität und maximale Stromantwort in den KO Zellen ist.

Zusammenfassend wurde CCZ1 als ein neuartiges regulatorisches Protein für TPC2 identifiziert, dessen Verlust zu einer gesteigerten TPC2 Aktivität führt und die Empfindlichkeit des Kanals gegenüber seinen Agonisten signifikant erhöht. Dies führt in Tumorzelllinien zu einer verstärkten Zellmigration und Proliferation. Diese Ergebnisse erweitern das Verständnis der komplexen Regulierung von TPC2 und deuten darauf hin, dass eine therapeutische Beeinflussung der TPC2–CCZ1-Achse neue Möglichkeiten in der Behandlung TPC2-assoziierter Erkrankungen bieten könnte.

Table of Contents

# 1 Introduction

## 1.1 Discovery of Caffeine-Calcium-Zinc sensitivity 1 (CCZ1)

The *CCZ1* gene was initially identified and characterized in yeast, where its genetic deletion in diploid strains led to hypersensitivity to caffeine, calcium, zinc and defective sporulation [1]. The hypersensitivity to divalent ions suggested that the protein encoded by the *CCZ1* gene (CCZ1) is involved in vacuolar function. Further studies by Kucharczyk demonstrated that overexpressing Ypt7, the yeast orthologue of the mammalian small GTPase Rab7, could rescue the phenotypes observed in *CCZ1* KO yeast strains [1, 2]. This discovery not only highlighted the functional and physical interaction between CCZ1 and Ypt7 but also suggested that CCZ1 acts as a guanin nucleotide exchange factor (GEF) required to activate Ypt7/Rab7. The name "CCZ1", originally based on its hypersensitivity phenotype, was retained, and widely adopted in subsequent research.

## 1.2 Structure of MCC

Over the last years, the understanding of CCZ1 has been significantly expanded in terms of its protein structure, essential partner proteins and diverse functional roles.

The CCZ1 protein is highly conserved and forms a stable 1:1 complex with the protein MON1 across all species studied so far, referred to as the MON1-CCZ1 complex (MC1). MC1 functions as a guanine nucleotide exchange factor (GEF) for Ypt7/Rab7 by catalyzing the exchange of GDP for GTP [3-7], which process will be further described in detail in section 1.5 (**Figure 1**).

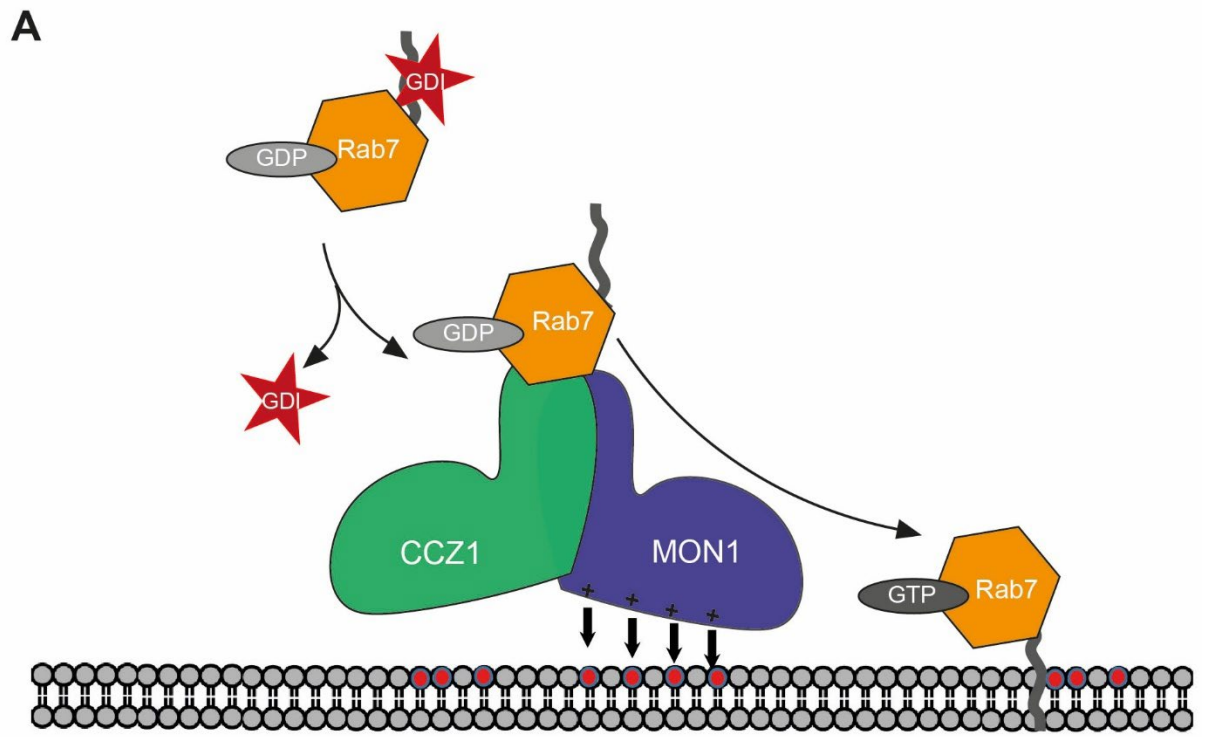


**Figure 1 MC1 is a Rab7 GEF**

CCZ1 and MON1 build a complex and recruit onto endolysosomal membranes. Electrostatic interactions (indicated by black arrows) between positively charged amino acids in MON1 and negatively charged phospholipids in the membrane (red circles) facilitate this process. Following recruitment to the membrane, MC1 binds Rab7-GDP catalyzing the exchange of GDP by GTP. Finally, activated Rab7-GTP becomes membrane bound by integration of its geranyl-geranyl tail. GDI, the guanine-nucleotide dissociation inhibitor, interferes with Rab7 activation by masking the geranyl anchor.

Recent cryogenic-electron microscopy (Cryo-EM) structures of MC1 in fungi, Drosophila, and human have provided detailed insights into the intra-complex interactions. Both MON1 and CCZ1 contain three “Longin domains” (LDs), defined by a highly conserved N-terminal domain with a profilin-like fold, which is critical for membrane trafficking and fusion processes [8, 9]. Within MC1, The LD1 domains of MON1 and CCZ1 constitute the catalytic core, responsible for GDP-to-GTP exchange (**Figure 2A**), whereas the LD2 and LD3 domains may be involved in membrane

recruitment and interactions with other partner proteins. Indeed, although electronic surface potential mapping of MC1 across different species remains unavailable, studies in fungi revealed that LD2 and LD3 of MON1 harbor extensive positively charged surfaces, whereas LD1 and LD3 of CCZ1 exhibit negatively charged regions. The remaining domains of the MC1 complex show a more uniform distribution of charge and hydrophobicity. These large positively charged regions likely mediate membrane association, as basic interfaces in peripheral membrane proteins commonly interact electrostatically with negatively charged phospholipid head groups [10].

In metazoans, including mouse and man, the MC1 complex is assembled with another protein, designated RMC1 (also known as C18orf8 or Bulli in flies [11]), to a trimeric complex (MON1-CCZ1-RMC1, shortly MCC) [5, 9, 10]. RMC1 lacks Longin domains but interacts with LD2 and LD3 of CCZ1 and LD2 of MON1 through its C-terminal region (**Figures 2A-B**). Notably, this interaction does not affect the catalytic conformation of the MON1-CCZ1 core. Instead, RMC1 seems to play an auxiliary role by increasing the stability of the complex in the cytosol. Functional studies reveal that *RMC1* KO results in a milder phenotype compared to knockout of *MON1* or *CCZ1*, supporting its role in stabilizing MCC rather than directly influencing catalytic efficiency [7].

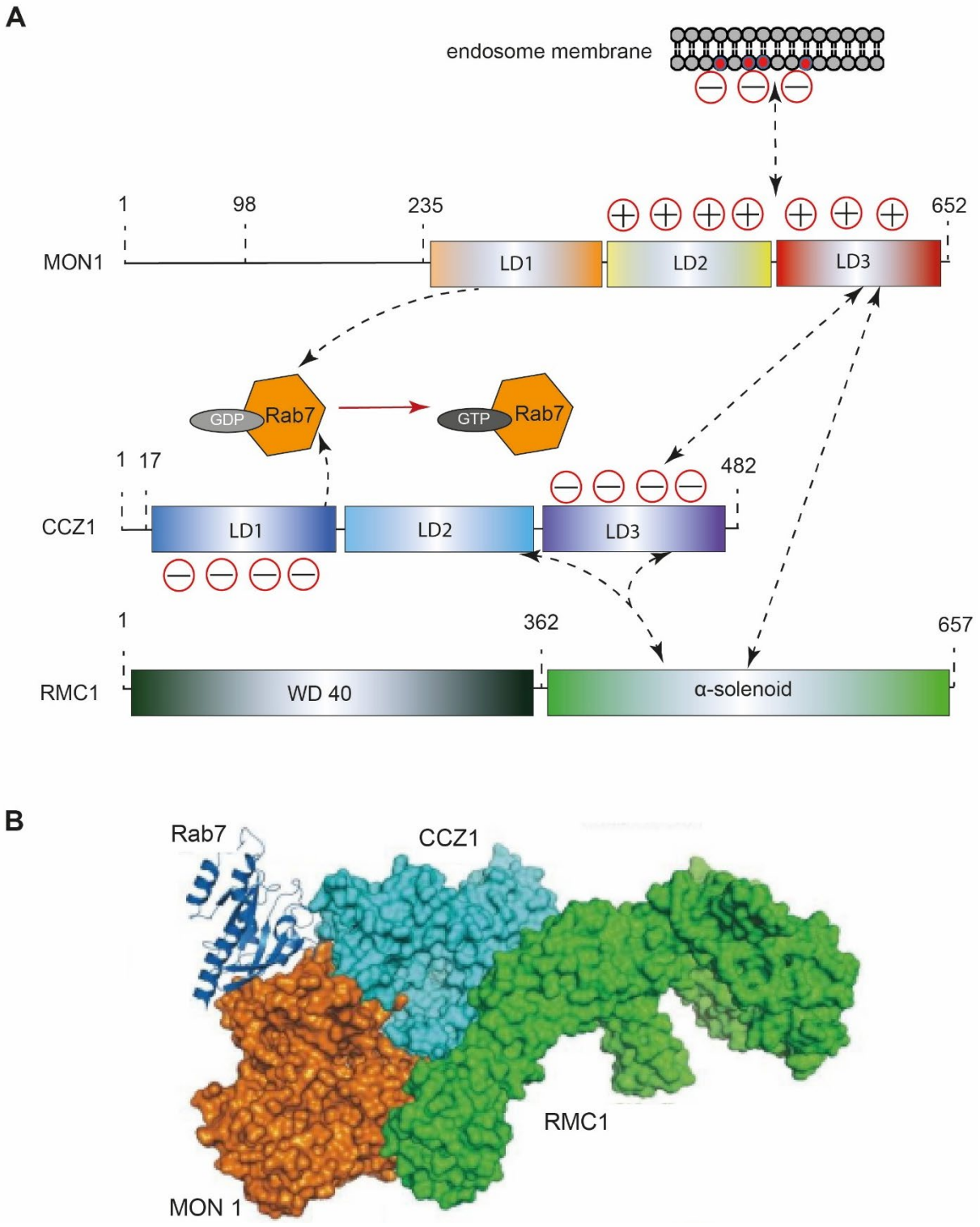


**Figure 2 Structure of the Rab7 GEF complex**

(**A**) Schematic domain arrangement of human MON1-CCZ1-RMC1 subunits. LD1s of MON1 and CCZ1 form catalytic core to activate Rab7-GDP into Rab7-GTP, positive charged amino acids in LD2 and LD3 domains of MON1 facilitate membrane integration with negative

phospholipids (indicated as red heads) on endosome membrane, α-solenoid domain of RMC1 recruits to MC1 via interaction with LD3 of MON1 and LD2 and LD3 of CCZ1. WD40, α-solenoid and LDs (LD1 to LD3) are indicated with different colors. **(B)** Surface representation of human MCC complex with Rab7 (dark blue) in ribbon model (RMC1 shows in hell green, MON1 in orange and CCZ1 in turquoise). Reproduced from Tang et al. [12], Figure 1E.

## 1.3 Diverse functions of MCC

The MCC complex participates in multiple cellular pathways by guiding Rab7 to various organelles. Since different organelles display distinct phosphoinositide profiles and there is no evidence that MCC selectively recognizes these lipid species, additional factors must direct its organelle-specific targeting.

MON1 can bind Rab5 in early endosomes via its N-terminal region and, as a result, promotes the recruitment of Rab7 on early endosomes and drives early-to-late endosome maturation [13]. However, under starvation conditions, Rab7 is recruited to pre-autophagosomes rather than early endosomes to enhance autophagy through interactions involving MCC and other proteins. Specifically, CCZ1 directly binds LC3 and redirects MCC recruitment from early endosomes to pre-autophagosomes [14]. In parallel, NRBF2—a component of the class III phosphatidylinositol 3-kinase complex that localizes to autophagosomes—also interacts with the MCC, enhancing its GEF activity toward Rab7 on autophagosomes [15] and thereby promoting autophagy. In osteoclasts, secretory lysosomal trafficking from the perinuclear region to the cell surface is essential for bone resorption. MC1 interacts with the a3 subunit of lysosomal V-ATPase, facilitating Rab7 localization to secretory lysosomes and establishing a direct a3–Rab7 interaction that promotes their movement toward the cell surface [16, 17]. Additionally, C5orf51, another MCC interactor, is crucial for Rab7 recruitment to

depolarized mitochondria destined for lysosomal degradation, as its loss disrupts Rab7 localization under mitophagy [18].

Genetic ablation of *CCZ1* in Caenorhabditis elegans embryos disrupts early development by impairing autophagic processing of lipid droplets and apoptotic corpses. Consequently, enlarged vesicles containing undigested cargo accumulate, leading to over 90% embryonic lethality [19, 20]. Although no human disorders are directly linked to *CCZ1* mutations, *HSP4*—a gene implicated in Hermansky–Pudlak syndrome (an autosomal recessive disorder characterized by faulty intracellular vesicle trafficking, melanosomal defects, hypopigmentation, and reduced visual acuity)—is a homolog of *CCZ1* acting as Rab32 and Rab38 GEF [21].

In both yeast and mammalian cells, *CCZ1* ablation disrupts vacuole and lysosome morphology, leading to fragmented vacuoles, autophagosomes accumulation, and enlarged lysosomes [1, 22-24], underscoring the essential role of CCZ1 in endosomal pathway and lysosome fusion. Recent studies further highlight the pathophysiological relevance of CCZ1 through its regulatory function in endosomal trafficking. For instance, *CCZ1* inactivation impedes Filovirus infection by trapping viral particles within early endosomal vesicles, thereby inhibiting viral replication [25]. In cervical squamous cell carcinoma (CSCC), elevated CCZ1 mRNA levels correlate with poor prognosis, and *CCZ1* knockdown reduces tumor cell proliferation, suggesting that CCZ1 could serve as both a diagnostic biomarker and a therapeutic target in CSCC [26]. Moreover, in Alzheimer's disease (AD), reduced Rab7 activity contributes to impaired autophagy. Overexpression of the MC1 complex enhances Rab7 function, accelerates autophagic flux, and promotes the degradation of amyloid-β (Aβ) and phosphorylated tau (P-tau), highlighting the CCZ1–MON1–Rab7 axis as a promising therapeutic target for AD [27].

## 1.4 Rab7 isoforms and their activation circle

Rab7 is a small GTPase belonging to the Ras-like GTPase superfamily and is highly conserved across species [28-30]. In mammalian cells, Rab7 has two homologues: Rab7a and Rab7b [31]. Both proteins share substantial homology (50% sequence identity and 65% similarity) but fulfil different roles in intracellular transport. Rab7a is primarily localized to late endosomes and lysosomes, where it regulates the maturation of early endosomes into late endosomes and mediates the fusion of late endosomes with lysosomes [32-34]. Additionally, Rab7a can be recruited to autophagosomes or defective mitochondria, facilitating their maturation or fusion with lysosomes for cargo degradation [35-39]. In contrast, Rab7b is only partially associated with lysosomes and predominantly found in the Golgi apparatus. Its localization suggests a critical role in the transport from endosomes to the trans-Golgi network (TGN) [40, 41]. In this thesis, the focus is on the interplay between MCC, Rab7a and TPC2 (TPC2 will be introduced in detail in section 1.6-1.10) due to their overlapping subcellular location, and hereafter Rab7a is referred to as Rab7 unless otherwise specified.

Despite their distinct subcellular locations, Rab7 isoforms undergo the same activation-deactivation cycle (**Figure 3**). Newly synthesized Rab7 proteins are recognized by Rab Escort Protein (REP) and delivered to Rab Geranyl-Geranyl Transferase (RabGGT) for the addition of geranyl-geranyl groups to the C-terminus [42, 43]. Once modified, Rab7 associates with GDP Dissociation Inhibitor (GDI), which stabilizes the GDP-bound form of Rab7 and prevents the geranyl-geranyl tail from interacting with membranes [44]. This interaction keeps GDP-bound Rab7 inactive and cytosolically distributed. To initiate activation, GDI Displacement Factor (GDF) removes GDI, exposing the geranyl-geranyl anchor and recruiting Rab7 to the membrane [45, 46]. At

the membrane, guanine nucleotide exchange factors (GEFs), namely MCC, facilitate the exchange of GDP for GTP, activating Rab7. The activated Rab7-GTP dissociates from the MCC and becomes membrane-associated, where it can interact with its downstream effector proteins. The MCC complex exhibits a transient "kiss-and-run" interaction with Rab7 during this process [47-49]. Inactivation of Rab7 is mediated by GTPase-activating proteins (GAPs), which accelerate the hydrolysis of GTP to GDP [50]. The resulting GDP-bound Rab7 then reassociates with GDI, returning to the cytosol and completing the cycle. This tightly regulated cycle ensures precise spatiotemporal control of Rab7 activity in cellular processes.

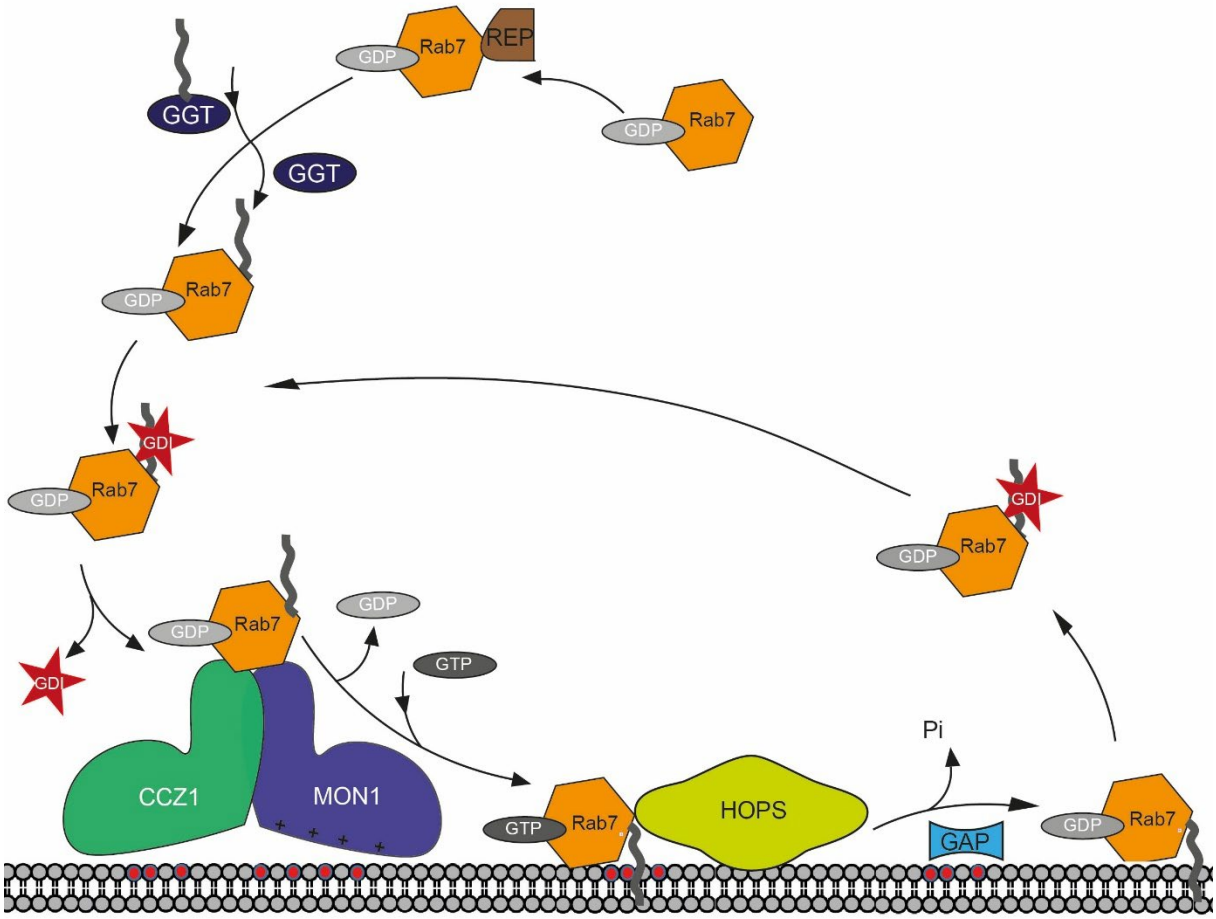


**Figure 3 Activation and deactivation cycle of Rab7**

Newly synthesized Rab7 proteins are first recognized by REP and delivered to RabGGT, which attaches geranyl-geranyl groups to the Rab7 C-terminus. Once modified, Rab7 binds GDI, stabilizing its GDP-bound form and preventing the geranyl-geranyl tail from engaging with membranes. As a result, Rab7 remains inactive and confined to the cytosol. To trigger activation, GDF removes GDI, exposing the geranyl-geranyl anchor and recruiting Rab7 to the membrane. On the membrane, MCC facilitate the exchange of GDP for GTP, thereby activating Rab7. The activated Rab7–GTP dissociates from MCC and remains membrane-associated, where it interacts with downstream effector proteins (e.g., HOPS). Inactivation is mediated by GAPs, which stimulate GTP hydrolysis to GDP. The resulting GDP-bound Rab7 then rebinds GDI, returns to the cytosol, and completes the cycle.

## 1.5 Effectors of Rab7 and its role in cell migration

Functionally, Rab7 governs membrane trafficking and fusion processes, showing an indispensable role in cargo transport to lysosome and promoting fusion [51]. The specific processes controlled by Rab7 are diverse, as reflected by the large and diverse set of Rab7 effectors with various localizations [33, 52-54].

The transition from Rab5 to Rab7 is critical during endocytosis. Once activated, Rab7 recruits TBC2—a Rab5-specific GTPase-activating protein (GAP)—to the membrane, where it hydrolyzes GTP-bound Rab5 to GDP. This prevents further Rab5 activation, facilitates the switch to Rab7 and promotes maturation. Notably, a hyperactivation of Rab5, either by overexpression of a constitutively active Rab5 mutant, Rab5[QL], or due to defects in Rab5 GAPs, disrupts the maturation process and leads to enlarged endosomes [23, 55]. Restoring normal Rab5 activity—either by expressing a Rab5 GAP or overexpressing a dominant-negative Rab5 mutant, Rab5[NT]—reduces endosome size to more physiologically appropriate dimensions.

Besides promoting early-to-late endosome maturation, active Rab7 on late endosomes also interacts with various effectors to facilitate vesicle movement and fusion prior to being inactivated by its GAP. For example, RILP (Rab7-interacting lysosomal protein) associates with active Rab7 on endosomes and lysosomes and recruits the dynein-

dynactin motor complex, driving late endosomes and lysosomes toward the microtubule minus end and clustering them away from the cell periphery [56]. In the context of autophagy, FYCO1 interacts with Rab7 on autophagosomes and lysosomes to mediate vesicle transport toward the microtubule plus end [57], pointing out a fundamental role of Rab7 for movement of Rab7-positive vesicles and organelles on microtubules both towards plus and minus ends. Moreover, Rab7 can also interact with Rac1 and vimentin [58, 59], both of which are key regulators of cell motility [60, 61]. Altogether, these results point to a key role of Rab7 in cell migration.

Indeed, Rab7 is upregulated in multiple cancer cell types, where its overexpression correlates positively with metastasis and malignancy of the disease. Rab7 has been shown to regulate cancer cell migration through various mechanisms [62-65]. For instance, in gastric cancer cells, Rab7 enhances the phosphorylation of PI3K and AKT, thereby promoting proliferation [66]. In HT-1080 cells, inactivating Rab7 impairs the trafficking of MT1-MMP back to the plasma membrane, slowing invasive capacity [67]. Recently, TPC2 was proposed as a Rab7 effector [62, 68]. Co-IP, FRET and lysosomal patch clamp experiments confirmed that Rab7 interacts with TPC2 and enhances TPC2-mediated currents, thereby promoting TPC2-dependent migration in melanoma cells via GSK3β, β-catenin, and MITF.

## 1.6 Two-Pore Channels (TPCs)

TPCs are members of the pore-loop cation channel superfamily. Each TPC subunit consists of two fused transmembrane domains, each containing 6 helices and a pore loop. Two subunits assemble to a pseudotetrameric complex, which is structurally

related to voltage-gated sodium and calcium channels. TPC1, the first identified member, was cloned from rat kidney (Accession No. AB018253) and later also from Arabidopsis thaliana (Accession No. AAD11598), sharing 24.6% amino-acid identity. Subsequently, two other members TPC2 and TPC3 were identified. While TPC1 and TPC2 are universally expressed cross species, TPC3 is absent from the genomes of many animals, including mice, rats, and humans (**Figure 4)** [69].

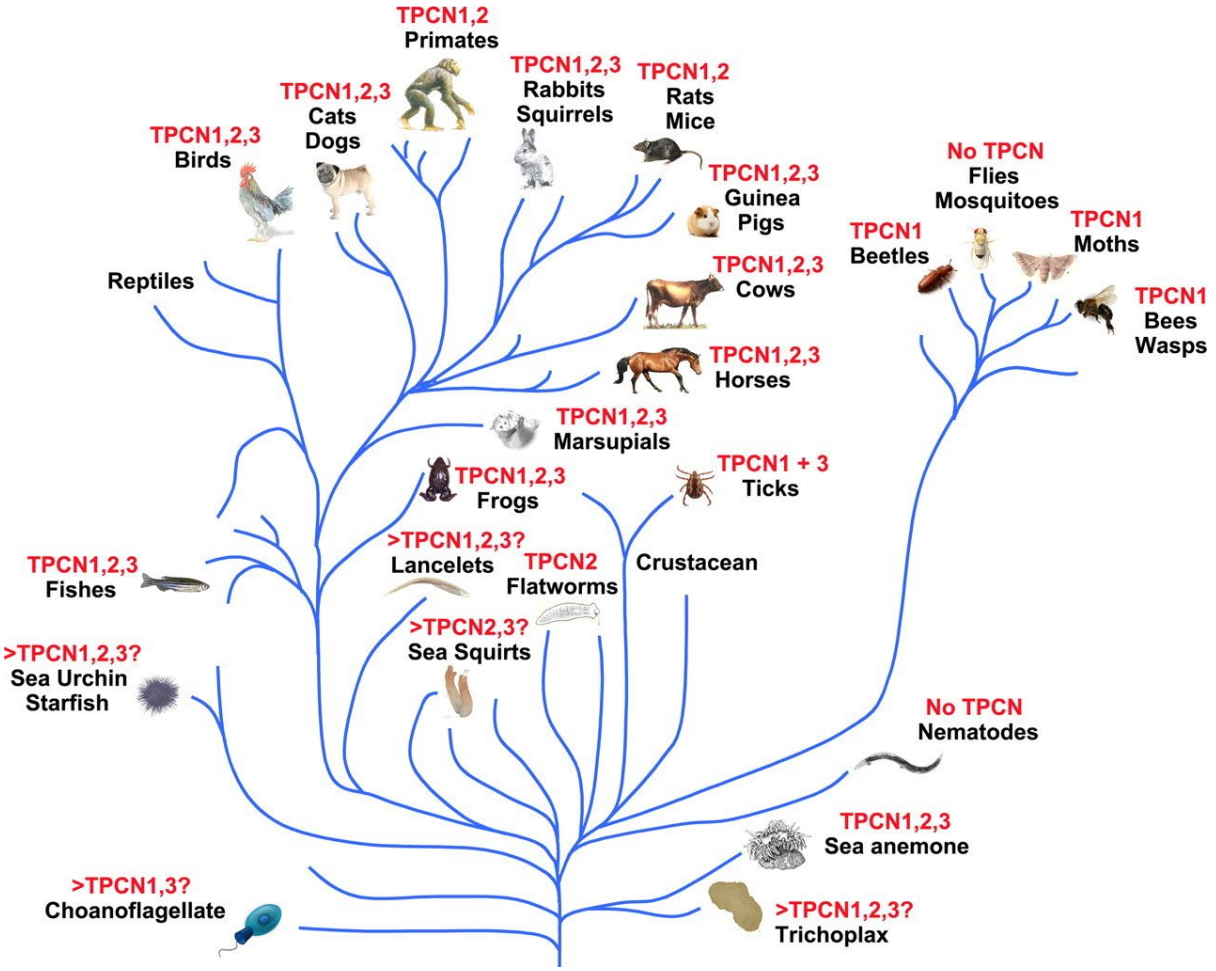


**Figure 4 Phylogenetic tree of TPCs in animals**

Schematic diagram displays partial family trees from the animal kingdom and identifies key examples of species in which the genes encoding TPC1, TPC2, and TPC3 are absent or present. “>” denotes possible presence of additional TPCs. Higher primates, including man, as well as some rodents (mouse, rat) do not contain a functional TPC3 gene. Reproduced from Zhu et al. [69], Figure 3.

In mammalian cells, TPC1 localizes primarily to less acidic organelles, such as early and recycling endosomes [70], whereas TPC2 resides in more acidic late endosomes and lysosomes [71-73].

Both NAADP and $PI(3,5)P_2$ are endogenous activators of TPC1. While $PI(3,5)P_2$ induces a $Na^+$ specific current, the channel becomes permeable to $Ca^{2+}$ when activated by NAADP. TPC1 can be activated in a voltage dependent manner in the present of $PI(3,5)P_2$ and this voltage-dependent channel opening is pH-dependent: an increase in lysosomal pH shifts channel´s activation threshold toward a more hyperpolarized potential. Lysosomal $Ca^{2+}$ increases TPC1 open probability under activation by NAADP in a dose dependent manner as lysosomal $Ca^{2+}$ concentration rises [74, 75].

TPC2 shares several functional features with TPC1. For instance, TPC2 can also be activated by both NAADP and $PI(3,5)P_2$, inducing $Ca^{2+}$ specific or $Na^+$ specific currents. NAADP-mediated TPC2 activation is also modulated by lysosomal $Ca^{2+}$: higher lysosomal $Ca^{2+}$ concentrations (200 μM) increase the channel's sensitivity to NAADP, enabling very low levels of NAADP (10n M), which has little effect on TPC2 when lysosomal $Ca^{2+}$ is only 10 μM, to open the channel. Additionally, lysosomal pH can regulate TPC2´s affinity to NAADP, shifting activation from irreversible at neutral pH to reversible at low pH, and producing a bell-shaped concentration–response curve [76]. However, unlike TPC1, $PI(3,5)P_2$ induced TPC2 activation shows minimal pH dependency [77] and TPC2 is not voltage independent, whose activation requires the presence of agonists. Interestingly, $Mg^{2+}$ inhibits both NAADP and $PI(3,5)P_2$ induced TPC2 activation in a pH-dependent manner from both lysosomal and cytosolic sides [78].

Plants possess only one TPC gene encoding a channel that is distantly related to TPC1. Plant TPC1 localizes to the vacuolar membrane and exhibits distinct gating and selectivity properties [79]. It functions as a slow vacuolar (SV) channel that mediates a $Ca^{2+}$ dependent $Ca^{2+}$ release into cytosol in a voltage dependent manner. Cytosolic $Ca^{2+}$ potentiates voltage activation by binding to the EF hand domain, whereas vacuolar $Ca^{2+}$ slows down voltage activation [80-82]. Plant TPC1 plays critical roles in processes such as seed germination, facilitation of leaf wound healing through jasmonate synthesis [83], and maintaining vacuolar membrane potential [84].

## 1.7 Structure of human TPC2

Like other TPC channels, human TPC2 (HsTPC2) is a “dimer of dimers”, with each subunit containing two homologous Shaker-like six-transmembrane (6-TM) domains, designated 6-TM I and 6-TM II. Each 6-TM domain comprises six transmembrane helices (IS1–S6 for 6-TM I and IIS1–S6 for 6-TM II). Similar to most voltage-gated ion channels, HsTPC2 exhibits a domain-swapped arrangement: the S1–S4 voltage-sensing domain (VSD) of one 6-TM interacts with the S5–S6 pore-forming domain of the adjacent 6-TM. Notably, the linker connecting the two 6-TMs folds into an EF-hand like domain structure whose pair of motifs lack the essential acidic residues for $Ca^{2+}$ coordination [79, 85], preventing the channel from sensing cytosolic $Ca^{2+}$ (**Figure 5A**).

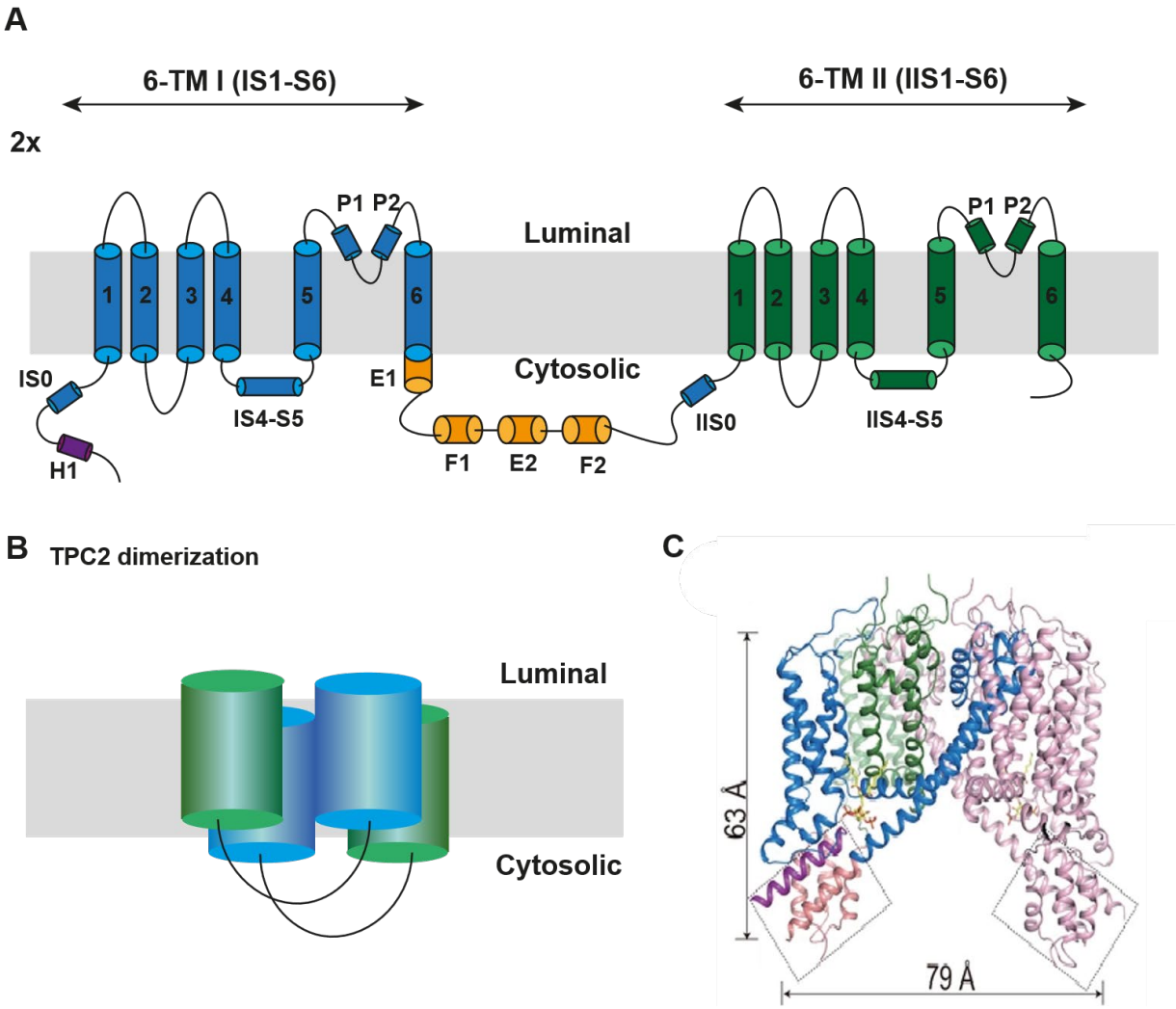


**Figure 5 Structure of HsTPC2**

(**A**) Topology and domain arrangement of HsTPC2 subunit. (**B**) Arrangement of two HsTPC2 subunits to for a pseudo-tetramer. (**C**) Cyo-structure of HsTPC2 with one subunit colored as that in (**A**) and another subunit in pink. PI(3,5)$P_2$ are shown as yellow sticks, two EF-hand domains are boxed. Reproduced from She et al. [79], Figure 1B.

Although human TPC2 (HsTPC2) contains a voltage-sensing domain (S1–S4) with multiple positively charged arginine residues in S4, its activation is voltage-independent. The key difference from other voltage-dependent channels that possess a canonical voltage sensor is that HsTPC2 has an isoleucine, rather than an arginine, at position 551 in II S4. Remarkably, introducing an arginine at position 551 can convert

HsTPC2 into a voltage-dependent channel. Conversely, mouse voltage dependent TPC1 (MmTPC1) can be rendered voltage-independent by substituting the arginine at its corresponding position with glutamine or isoleucine [74, 79, 86].

$PI(3,5)P_2$, the endogenous activator of TPC2, binds directly to TPC2 at the junction formed by IS3, IS4, and the IS4–IS5 linker in the first six-transmembrane domain (6-TM I). Specifically, the inositol 1,3,5-trisphosphate head group of $PI(3,5)P_2$ interacts with Lys204 and nearby basic residues. An interaction with Arg329 on IS6 induces a shift in the IS6 helix from a partially broken to a continuous conformation. This structural rearrangement should open the channel pore, enabling ion flux [79] (**Figure 6**). A mutation in Lys204 against alanine abolished $PI(3,5)P_2$ activity on TPC2 [87]. Furthermore, a recent molecular dynamics simulations (MD) study demonstrated that the selective filter II (Val652-Asn653-Asn654) in both subunits must also undergo a conformational change for $Na^+$ conduction under $PI(3,5)P_2$ activation, suggesting a dynamic nature of the TPC2 ion conduction pore [88].

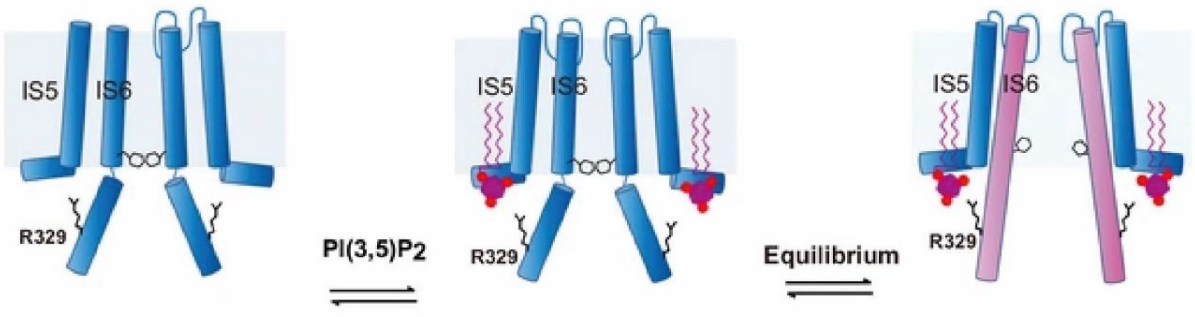


**Figure 6 Activation gating of HsTPC2 by $PI(3,5)P_2$**

The S5 and S6 domains of both TPC2 subunits are shown, with IS5 and IS6 labeled. On the left, the channel is depicted in closed state. In the center, the channel remains closed but with

$PI(3,5)P_2$ suited in, indicating that the ligand binding pockets can accommodate $PI(3,5)P_2$ without significant conformational changes. On the right, the channel is shown in its open state, induced by $PI(3,5)P_2$. $PI(3,5)P_2$ binds at the junction formed by IS3, IS4, and the IS4–IS5 linker within the first six-transmembrane domain (6-TM I), interacts with R329 on cytosolic EF hands, applying an outward force that pulls IS6 and EF hands into a straight conformation. The same process occurs also in the other subunit, resulting in pore opening. Reproduced from She et al. [79], Figure 5C.

## 1.8 Ion selectivity of TPC2

TPC2 differs from most other ion channels in that its ion selectivity changes depending on the activating ligand. When activated by $PI(3,5)P_2$, TPC2 predominately conducts $Na^+$ current ($P_{Ca}/P_{Na}$~0,08) [77, 89, 90]. In contrast, NAADP activation boosts the $Ca^{2+}$ conductance to a higher level ($P_{Ca}/P_{Na}$~0,65) [71, 72, 75, 91]. Unlike $PI(3,5)P_2$, NAADP does not seem to directly interact with the channel but rather requires NAADP binding proteins (e.g. JPT2 and Lsm12) to activate TPC2 [92-94].

## 1.9 Agonists and antagonists of TPC2

Besides the endogenous TPC2 activators NAADP and $PI(3,5)P_2$, several synthetic TPC2 agonists have been identified. Specifically, the two compounds A1P and A1N were found to mimic $PI(3,5)P_2$- and NAADP-mediated activation, respectively, thereby evoking $Na^+$ specific and $Ca^{2+}$ specific currents [91]. Importantly, both compounds are membrane-permeable and thus serve as valuable tools for dissecting cellular processes connected to $PI(3,5)P_2$ versus NAADP-driven TPC2 activation. Unlike NAADP, A1N seems to act directly on the channel and does not require additional proteins for its action [95].

Beyond modulating TPC channel ion selectivity, various agonists can also tailor their voltage dependence. For instance, several tricyclic antidepressants (TCAs), such as clomipramine and chlorpromazine, have been reported to activate TPC2 in a voltage-dependent manner, indicating an agonist-specific gating mechanism [87].

TPC2 activity can be also influenced by pharmacological inhibitors. Tetrandrine, a bis-benzylisoquinoline alkaloid isolated from the medicinal plant Stephania tetrandra, has shown promise in inhibiting cancer cell migration via TPC2 blockade [96], in curbing infection of Ebola virus [97], SARS-CoV-2 (COVID-19) [98], as well as in restricting pathological vascular neovascularization [99]. However, its clinical potential is constrained by limited accessibility (requiring either plant extraction or complex total synthesis) and systemic toxicity—documented as alveolar hemorrhage in CD-1 mice after a single intraperitoneal dose and drastically reduced viability of NL-20 and WI-38 cells after 24 hours—thus limiting its therapeutic utility [100]. In an effort to overcome these drawbacks, multiple tetrandrine derivatives have been synthesized and screened for enhanced specificity and reduced toxicity. Among them, SG-094 stands out for its potent inhibition of TPC2-dependent phosphorylation of VEGFR2-related targets, coupled with notably lower cytotoxicity [101]. The binding site of SG-094 in TPC2 has been recently determined with cryo-electron microscopy (EM) [102]. SG-094 binds to VSD II of TPC2, induces a confirmation change in both subunits, and stabilizes HsTPC2 in an inactive state by preventing IIS4/II5helix from rotating. Although SG-094 shares structural similarities with tetrandrine, these two compounds appear to inhibit TPC2 through different mechanisms. While Tyr436 on IIS1 is essential for SG-094 binding, this residue does not contribute to the inhibitory action of tetrandrine. SG-094 more effectively inhibits A1N-induced channel activity than A1P, whereas tetrandrine suppresses both agonists to a similar extent. However, the binding

site of tetrandrine on TPC2 remains unidentified, and further investigation is required to clarify the distinct actions of these structurally related antagonists. Ned-19, initially discovered as an NAADP antagonist, can diminish effectively TPC2 mediated lysosomal $Ca^{2+}$/ $Na^{+}$ release and suppresses cell migration but only exhibits significant effects at high micromolar concentrations (>100 µM) [96, 103, 104]. (**Figure 7**)

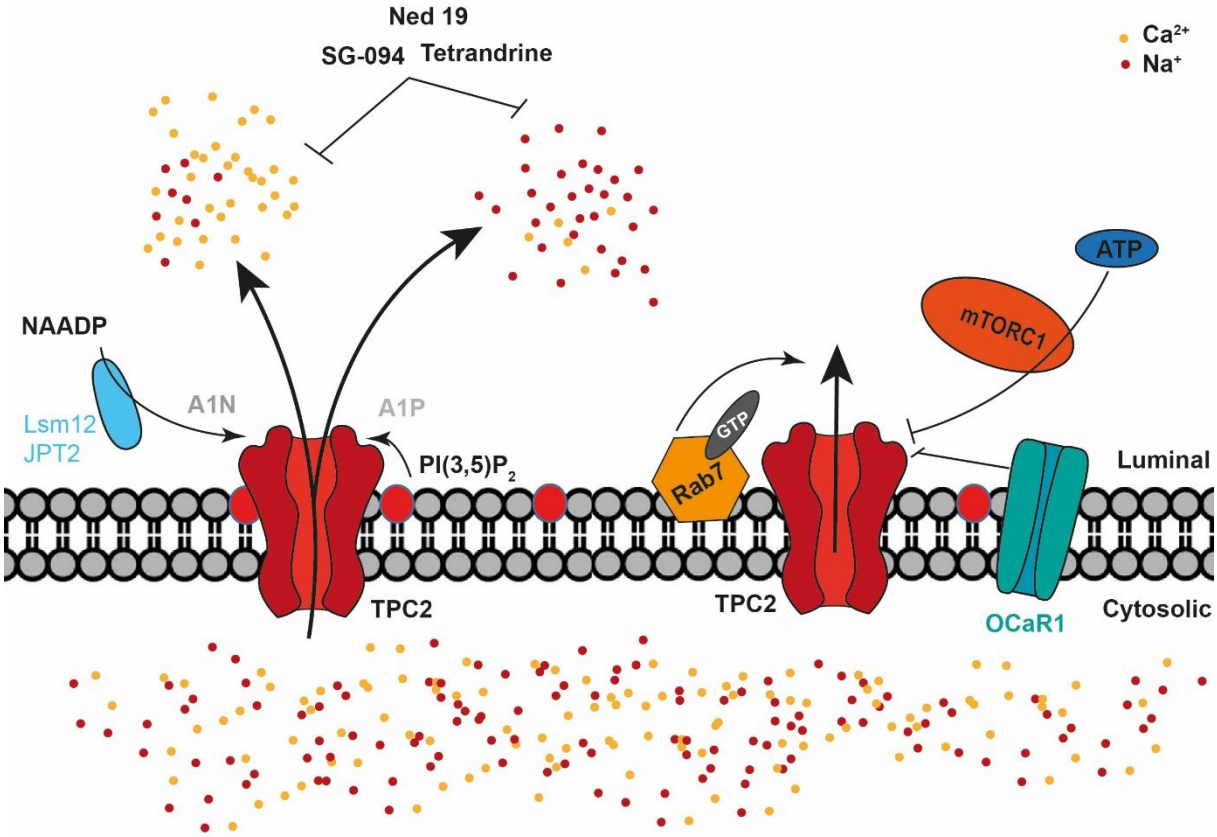


**Figure 7 Agonists and antagonists of TPC2**

$PI(3,5)P_2$ binds directly to TPC2 and induces a $Na^{+}$-specific current, whereas NAADP requires its binding proteins (Lsm12 and JPT2) to engage TPC2 and drive a $Ca^{2+}$-specific current. The synthetic agonists A1P and A1N functionally mimic the actions of $PI(3,5)P_2$ and NAADP, respectively, though through distinct mechanisms. Ned19, tetrandrine, and its derivative SG-094 inhibit TPC2 activity via different binding sites. $PI(3,5)P_2$ is depicted as red-circled phospholipids within the membrane. Rab7 enhances agonist-induced channel activation, while ATP suppresses it through interaction with mTORC1. Additionally, OCaR1/TMEM63A inhibits TPC2.

TPC2 is also functionally regulated by various proteins. For instance, nutrients such as amino acid and ATP have been shown to inhibit TPC2 channel activity through mTORC1 [68, 90]. OCaR1 can also inhibit TPCs activity and thereby controls $Ca^{2+}$ release from secretory granules during exocytosis [105]. Meanwhile, as discussed in section 1.5, Rab7 enhances TPC2 channel activity upon agonist activation, promoting TPC2 dependent signaling pathway [62, 68].

## 1.10 Function of TPC2 and its impact on pathological processes

Lysosomes act as both degradation centers and signaling hubs within cells, playing critical roles in maintaining homeostasis, regulating vesicle trafficking, and influencing development and aging. Proper lysosomal function is essential for responding to diverse signals, stresses, and stimuli. TPC2 directly impacts lysosomal physiology, thus influencing cellular processes controlled by these organelles.

Genetic ablation or pharmacological inhibition of TPC2 elevates lysosomal pH, disrupts vesicle trafficking, and enlarges lysosomes, thereby impairing pH-dependent hydrolytic enzymes and promoting the accumulation of undigested macromolecules [106-108]. These findings underscore TPC2's potential involvement in a range of pathological processes where lysosomal function plays a pivotal role.

TPC2 deletion or pharmacological blockade has been shown to inhibit cancer cell migration and proliferation in vitro and in vivo by disrupting β1-integrin recycling; under TPC2 deficiency, β1-integrin becomes trapped in early endosomes and cannot be properly processed [96]. In neovascular age-related macular degeneration (AMD), TPC2 inhibition reduces VEGFA and IL-1β secretion in the retina, diminishes

neovascularization, and attenuates immune activation [99]. This effect likely stems from impaired trafficking and fusion of secretory lysosomes with the plasma membrane in TPC2$^{-/-}$ macrophages, resulting in decreased release of inflammatory mediators.

TPC2 is also critical for low-density lipoprotein (LDL)-cholesterol trafficking. In TPC2$^{-/-}$ mice on a high-cholesterol diet, the inability to handle LDL-cholesterol properly contributes to non-alcoholic fatty liver disease [109]. Moreover, studies in fibroblasts from familial Alzheimer's disease patients revealed that excessive TPC2-mediated $Ca^{2+}$ currents promote lysosomal alkalinization—via enhanced $H^+$ efflux through a $Ca^{2+}/H^+$ exchanger—and reduce autophagic clearance of amyloid. Pharmacological TPC2 inhibition by tetrandrine restores normal lysosomal pH and enhances amyloid clearance [110]. Intriguingly, a similar TPC2 hyperactivation phenotype was identified in fibroblasts from Parkinson's disease patients; treatment with the TPC2 inhibitor Ned-19 or the PIKfyve inhibitor YM-201636 reversed lysosomal morphological defects [111]. On the other hand, defective lysosomal function arising from TPC2 ablation can be therapeutically exploited to overcome drug sequestration in chemotherapy. Specifically, knocking out TPC2 sensitizes vincristine-resistant acute lymphoblastic leukemia (ALL) cells to chemotherapeutic agents, offering a potential strategy for tackling drug resistance [106].

TPC2 exhibits distinct functional responses depending on the activating stimulus. A1P, but not A1N, induced TPC2 activation has been shown to enhance cellular exocytosis, whereas A1N, but not A1P, induces lysosomal alkalization [91]. Interestingly, co-activation of TPC2 with both agonists (A1P+A1N) significantly increases $Ca^{2+}$ flux without affecting $Na^+$ flux, suggesting a synergistical activation on TPC2 [112]. These observations highlight the stimulus-specific functional versatility of TPC2, offering valuable insights into its role in disease mechanisms and therapeutic potential. For

example, in lysosomal storage disorder disease model, the activation of TPC2 with A1P is enough for a rescue effect for cholesterol accumulation [113], leaving calcium signal cascade less affected. Targeting TPC2 while preserving its essential physiological functions could provide a more precise therapeutic approach with fewer side effects and remain a field needed to discover.

# 2 Aim of Study

Proteomic screens conducted by several laboratories, including our own, have revealed a number of proteins that directly or indirectly interact with TPC1 and TPC2 [114, 115]. Among these identified proteins were small GTPases of the Rab family, known for their critical roles in cellular signal transduction and endolysosomal function. Of particular interest was the potential involvement of Rab7 in the regulation of TPC2, given its key role in controlling endolysosomal vesicle trafficking and maturation. Furthermore, Rab7 has been shown to influence cancer cell migration and proliferation—processes that have also been linked to TPC2. Rab proteins do not function in isolation but are tightly regulated by proteins that control their activity states, facilitating GDP/GTP exchange (GEFs) or accelerating GTP hydrolysis (GAPs). The MCC complex has been previously identified as a specific Rab7 GEF, exerting significant influence over cellular processes regulated by Rab7.

The goal of this PhD project was to explore the functional and mechanistic relationship between MCC and TPC2. Specifically, the project aimed to investigate whether components of the MCC complex modulate TPC2 activity. To this end, cellular models lacking MCC components should be developed and utilized for electrophysiological analysis of TPC2-mediated currents employing lysosomal patch-clamp technology. Additionally, fluorescence-based techniques, such as FRET, in combination with immunoprecipitations, were to be used to examine the interaction between the channel and MCC components. Finally, the effects of MCC-dependent TPC2 regulation on cancer cell proliferation and migration should be studied. Overall, these investigations aim to enhance our understanding of the impact of TPC2 regulation in key physiological and disease processes.

# 3 Methods

## 3.1 Cell culture

Cells were cultured in DMEM supplemented with 10% FBS, 100 U/mL penicillin, and 100 µg/mL streptomycin at 37°C in a humidified environment with 10% $CO_2$. For lysosomal patch experiments, cells were seeded at an appropriate density onto poly-L-lysine (PLL)-coated coverslips (Microscope cover glasses 12mm: Glaswarentabrik Karl Hecht GmbH) in 24-well plates two days before experimentation. 24 hours post-seeding, cells were transfected with desired plasmids using Turbofect™, following the manufacturer's protocol.

To induce lysosome enlargement, a final concentration of 1 µM vacuolin-1 was added to each well on the evening before the experiment, as vacuolin-1 has been reported to nonspecifically enlarge endosomes and lysosomes up to 3 µm, which is commonly used in lysosomal patch clamp. This enlargement facilitates manual manipulation and recording from lysosomal membranes [116, 117].

**Cell Culture Medium**

Fetal bovine serum 10 %

Pen-Strep 100 U/mL

DMEM 500 mL (Invitrogen, #21885-025 for HEK 293 cell line; Invitrogen, #31966-021 for SK-MEL5 cell line)

Mix components and filter-sterilize (sterile syringe filters 0.2 µm: VWR, #5140061).

Store at 4℃; pre-warm to 37℃ before use.

**Poly-L-Lysine Coating Solution**

Poly-L-lysine 0.1 %

Boric acid 80 mM

Borate 10 mM

Sterilize by passing through a 0.2 µm filter and store in 70% ethanol under room temperature for a long-time storage.

## 3.2 Generation of *CCZ1* knockout and *RMC1* knockout cells in HEK 293 and SK-MEL5 cell lines

CRISPR-Cas9 nuclease system was applied to knock out *CCZ1* and *RMC1* genes in HEK 293 and SK-MEL5 cell lines. The protocol was adapted from the method described by F. Ann Ran et al. [118] and involved five primary steps: (1) design of sgRNAs and construction of sgRNA-containing CRISPR-Cas9 plasmids, (2) transfection of these plasmids into cells, (3) assessment of genome editing efficiency, (4) isolation and culture of single-cell clones, and (5) verification of genome editing in individual clones.

### 3.2.1 Design of sgRNAs and construction of sgRNA-containing CRISPR-Cas9 plasmids

Guide RNA sequences were designed using the online tools Crispor (http://crispor.gi.ucsc.edu/) and VBC Score (https://www.vbc-score.org/). Each exon of the target genes was individually submitted to these tools. The guide RNAs were then selected based on the lowest predicted off-target effects and highest efficiency scores. Guide RNAs were preferentially selected to target early exons or exons encoding functionally important amino acid sequence.

To knock out the two identical copies of the duplicated *CCZ1* gene, two guide RNA sequences with protospacer adjacent motifs (PAM) located immediately downstream at the 3´ end were selected. Guide RNA$_{CCZ1\text{-}1}$ targeted exon 11, while guide RNA$_{CCZ1\text{-}}$

$_2$ targeted exon 12, with the objective of deleting the sequence between these two cut sites. Conversely, to knock out the *RMC1* gene, one single guide RNA with a PAM at the 3´ end targeting exon 10 was utilized (guide RNA$_{RMC1}$), which introduced indel mutations leading to a premature stop codon.

A scaffold sequence (yellow) and U6 promoter (purple) together with its RNA polymerase III start site sequence (black) were appended to the 3´ end and 5´ end of designed guide RNA sequences respectively. The configuration of all required elements is illustrated in **Figure 8A**. The complete sequences were synthesized commercially and inserted into our CRISPR-Cas9 plasmid using Gibson assembly. Successful insertion was confirmed via Sanger sequencing, as shown in **Figure 8B**.

### 3.2.2 Effective transfection of sgRNA containing CRSPR-Cas9 plasmids into cells

Since our CRISPR-Cas9 plasmid lacks a fluorescence tag and HEK 293 or SK-MEL5 cells are not considered challenging to be transfected, a blank GFP plasmid was employed as a control to assess transfection efficiency. Following the manufacturer's protocol, high transfection efficiency was achieved using Lipofectamine 3000$^{TM}$.

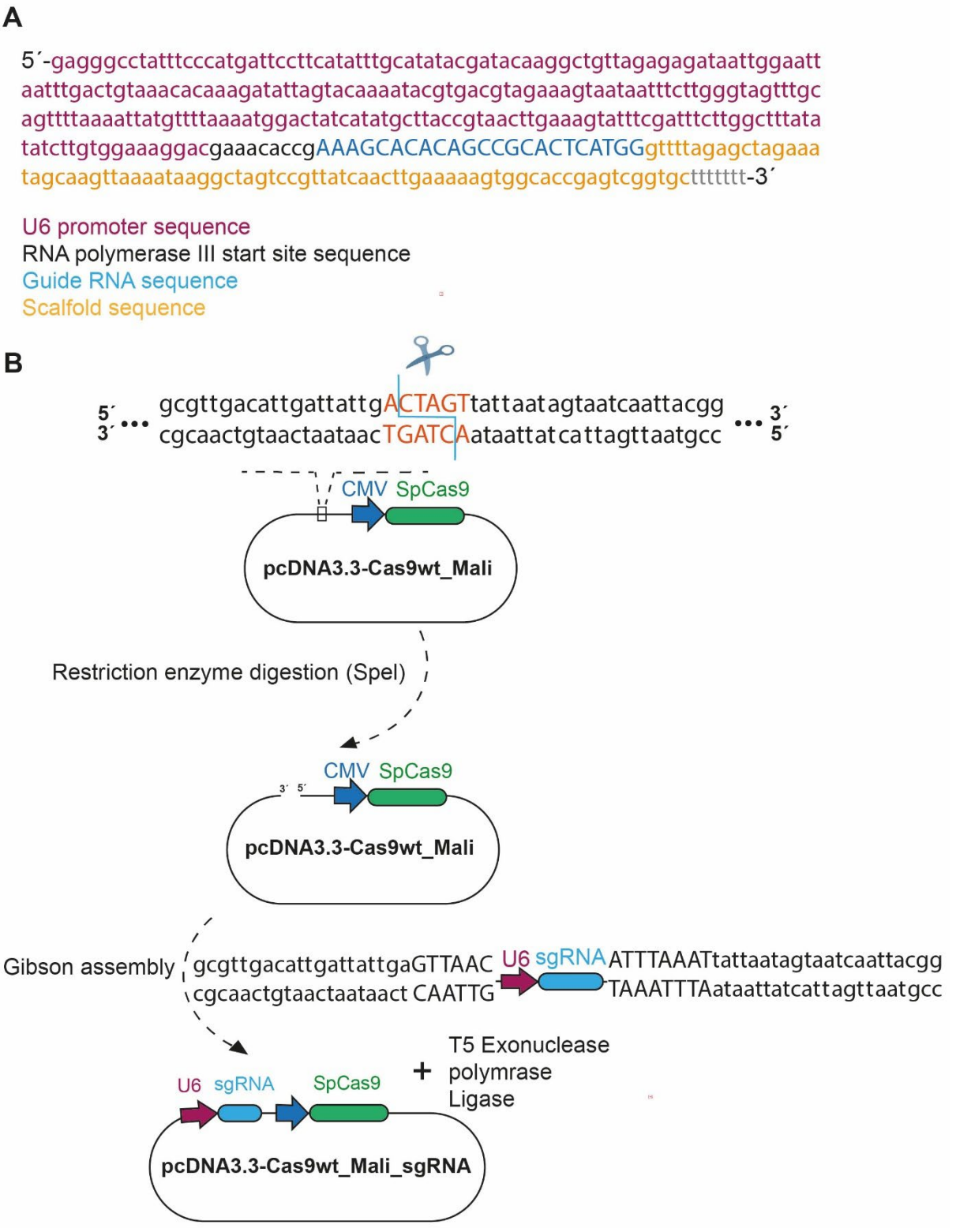


**Figure 8 Full structure of designed sgRNA and workflow of inserting sgRNAs into CRISPR-Cas9 plasmids**

(**A**) The complete sequence of designed sgRNA consisted of U6 promoter (red), RNA polymerase III start site (black), guide RNA (blue) and scaffold (yellow). (**B**) The plasmid was linearized through incubation with restriction enzyme (SpeI). Subsequently, the complete

sequence from A was modified to include overlaps at both termini, with these sequences designed to match the regions flanking both sides of the restriction enzyme (SpeI) cleavage site. Capitalized sequences on the overhangs indicate restriction enzyme recognition sites, enabling flexible exchange of sgRNA sequences. The Gibson assembly was carried out according to the manufacturer's instructions.

### 3.2.3 Assessment of genome editing efficiency of designed sgRNAs

Different strategies were used to validate the sgRNAs to knock out *CCZ1* and *RMC1*. For sgRNAs targeting *CCZ1*, a PCR primer pair was designed to amplify regions flanking the guide RNA targeting sites. Primer *CCZ1*_F was positioned upstream of guide RNA$_{CCZ1\text{-}1}$, while primer *CCZ1*_R was positioned downstream of guide RNA$_{CCZ1\text{-}2}$, resulting in a distance of 1544bp between the two primers. PCR was then conducted on the extracted genomic DNA of transfected and untransfected cells, and the PCR products were separated on a 0,7% agarose gel. A successful deletion of the 992 bp region between two sgRNAs produced a band at 552 bp (**Figures 9A-B)**, indicating efficient genome editing.

For the *RMC1* sgRNA efficiency assessment, another PCR was conducted using a primer pair flanking the CRISPR-Cas9 cut site (primer *RMC1_F*, primer *RMC1_R*) on extracted genomic DNA of transfected cells (**Figure 9C**), and the resulting PCR product was also separated on a 0,7% agarose gel. Because only one sgRNA was used to knock out *RMC1*, the indels were small and could not be distinguished from unedited sequence on the gel, appearing as one single band. Consequently, the entire amplified DNA fragment was excised from the gel and purified using the QIAquick Gel Extraction Kit (Cat.28705) according to the manufacturer's instructions. The purified DNA fragment was sent to Sanger sequencing using the primer *RMC1_F*. The presence of multiple peaks downstream of the cut site indicated a high editing efficiency (**Figure 9D**).

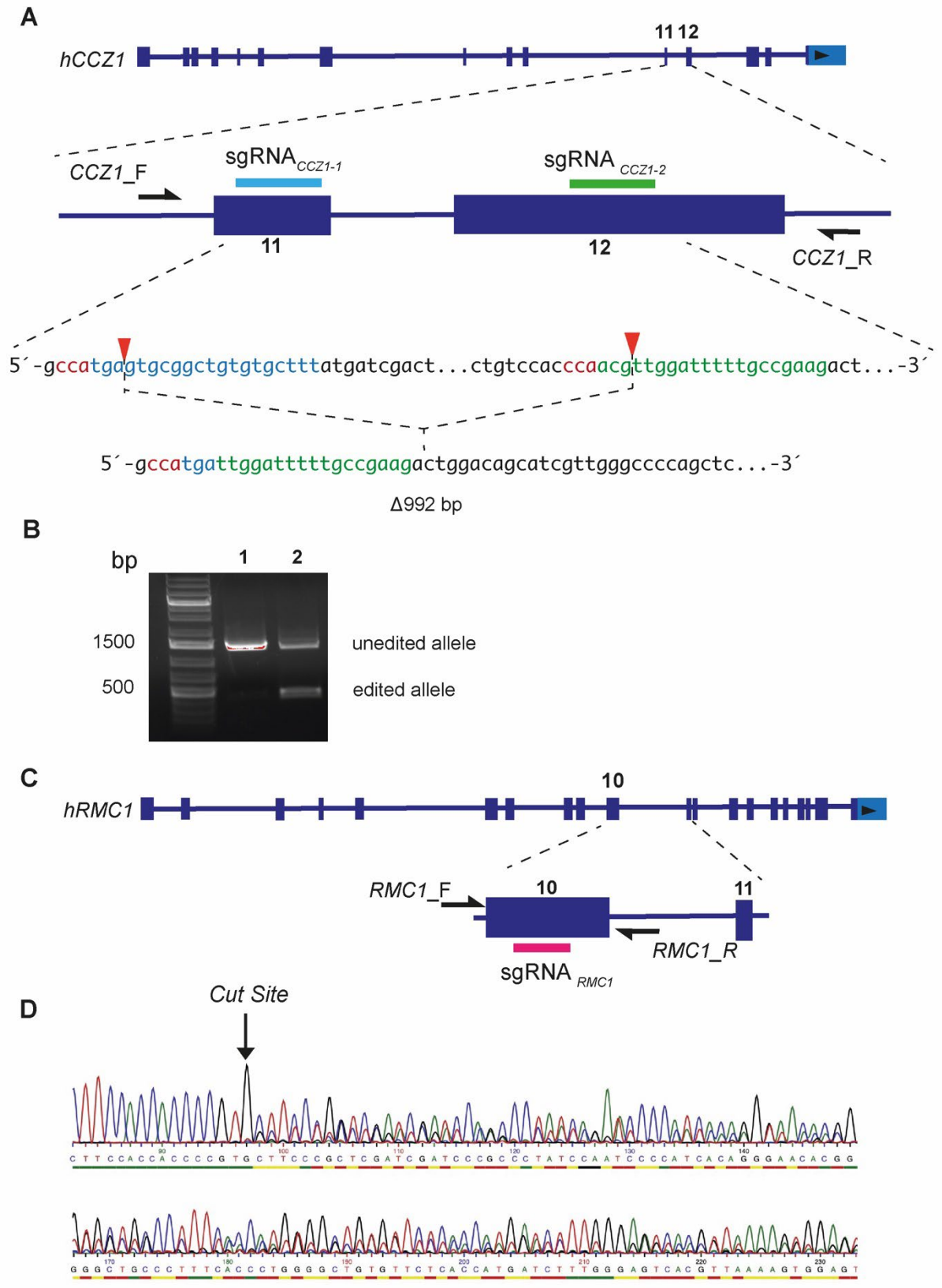


**Figure 9 Assessment of genome editing efficiency of sgRNAs targeting *CCZ1* and *RMC1***

(**A**) The schematic diagram illustrates the design of two sgRNAs targeting exon 11 and exon 12 of the *CCZ1* gene. A primer pair (*CCZ1*_F, *CCZ1*_R) spanning 1544 bp was designed to flank the sequence intended for deletion. A successful deletion caused a loss of 992bp and resulted in a band showed at 544bp. (**B)** PCR analysis was conducted using genomic DNA from untransfected HEK 293 cells as a control (lane 1) and genomic DNA from HEK 293 cells transfected with sgRNA-containing plasmids (lane 2). A 1544 bp band in lane 2 indicated an unprocessed region between exon 10 and exon 11, while a 552 bp band confirmed successful deletion of the target sequence. (**C**) The schematic diagram shows the sgRNA design targeting exon 10 of the *RMC1* gene. PCR primers (*RMC1_F*, *RMC1_R*) were designed to flank the sgRNA targeting sequence. (**D**) Sanger sequencing results following transfection with the $sgRNA_{RMC1}$-containing plasmid revealed the presence of multiple peaks, confirming successful genome editing at the target site.

### 3.2.4 Isolation and culture of single-cell clones and verification of genome editing in individual clones

48 hours post-transfection, cells were split and seeded as single cells into 96-well plates. To increase the likelihood of isolating a knockout single cell, at least three 96-well plates were seeded per knockout line using a limiting dilution method.

Briefly, the cells were first rinsed with PBS, followed by enzymatic digestion with trypsin. The digestion process was halted by adding culture medium supplemented with FBS. The resulting cell suspension was transferred to a Falcon tube and centrifuged at 300 rpm for 5 minutes at room temperature. The supernatant was discarded, and the cell pellet was resuspended in fresh culture medium. Cell was stained with trypan blue and counted (Countess II FL). $1 \times 10^6$ cells were resuspended into 10 mL of fresh medium. After thorough mixing, 1 mL of the cell suspension was again transferred into a new Falcon tube, followed by resuspension in 9 mL of fresh medium. The procedure was repeated twice, resulting in a Falcon tube containing 10 mL of medium with a final concentration of 1,000 cells. 3 mL aliquot of the cell suspension was diluted with 27mL of fresh medium, resulting in a final cell concentration of 1 cell per 100 µL of medium.

100 µL of the cell suspension was seeded into each well of a 96-well plate. A total of 30 mL of cell suspension was sufficient to seed three 96-well plates.

It was essential to identify and mark wells containing a single cell on the day following seeding. After several weeks of expansion, only colonies derived from a single cell were further expanded by splitting and seeding into two 24-well plates. One plate was maintained for continued cell culture, while the other was used for genomic DNA isolation.

For both knockout cell lines, PCR was performed using the primer pairs from section 2.2.3 (*RMC1*_F and *RMC1*_R, *CCZ1*_F and *CCZ1*_R). For each *RMC1* knockout single cell, the PCR product was subjected to TOPO cloning (using the TOPO™ TA Cloning™ Kit according to the manufacturer's instructions) to verify editing of both alleles. Only double-edited single cells were subsequently analyzed by Western blot to confirm protein deletion.

For each *CCZ1* knockout single cell, PCR product was analyzed via agarose gel electrophoresis to determine the length of DNA fragments. Only single clones exhibiting a single band at around 552 bp were selected for validation at the protein level via Western blot.

## 3.3 Lysosomal patch clamp electrophysiology

Patch-clamp technology has advanced rapidly in recent years, enabling detailed studies of ion channels. However, traditional whole-cell patch clamp techniques have limited access to ion channels located on intracellular organelles, creating an urgent need for modified approaches. Our laboratory has successfully established and routinely performs lysosomal patch-clamp techniques to study various lysosome-

localized channels across different cell types [117]. The key steps involved in lysosomal patch-clamping are outlined below.

### 3.3.1 Isolation of lysosome from cell

The PPL-coated coverslip with adherent cells was transferred to a patch-clamp chamber containing 1 mL of bath solution. Under a 40x microscope, only fluorescently labeled, enlarged endo-lysosomes were selected for isolation. Ideal lysosomes were positioned close to the cell edge, occupying less than half the cell's area, which improved the likelihood of successful isolation.

A pipette with a sealed opening (BF150-75-10, Sutter) was used to cut and isolate the lysosome. The pipette was first positioned above the plasma membrane, near the targeted lysosome, and lowered until slight membrane deformation was observed. The plasma membrane was then quickly ruptured by moving the pipette away from the cell, a step often repeated several times to fully sever the membrane without detaching the cell body from the coverslip.

The isolated lysosome was then pushed into the bath solution by pressing on the cell body with the pipette, moving it downwards. Occasionally, small fragments of plasma membrane remained attached to the lysosome, compromising the seal. However, when the lysosome remained connected to the cell body by actin filaments, it was less likely to be dislodged during the process, enhancing the chances of achieving a successful seal.

### 3.3.2 Formation of giga seal

A freshly prepared, polished borosilicate glass pipette was used for giga-seal formation. To increase the likelihood of achieving a giga-seal, the tip shape was carefully inspected under a microscope, with the diameter maintained between 0,4–0,8 mm.

Although smaller diameters facilitated giga-seal formation, they made lysosomal break-in more challenging. Additionally, the pipette tip was checked to ensure it was free of debris. In the extracellular solution, the pipette resistance ranged from 5 to 7 MΩ.

Before approaching the pipette to the extracellular solution surface, 0,02–0,04 mL of positive pressure was applied using a syringe. Although 0,05 mL of positive pressure could enhance seal formation, it complicated lysosomal break-in. Positive pressure also helped to keep dust away from the pipette tip.

The pipette was moved quickly toward the top of the target lysosome (within <10 seconds), and the positive pressure was released abruptly when the lysosome showed maximum deformation or was most displaced from its original position while still attached to the cell. A giga-seal (>1 GΩ) typically formed within a few seconds. For lysosomes displaying a slow increase in resistance, the Ramp Seal protocol or slight suction with a syringe was applied. After forming the giga-seal, any extra suction was released to facilitate lysosomal rupture in the next step.

### 3.3.3 Open lysosome

Due to the fragile nature and small size of lysosomes, applying suction by mouth as done in other patch setups could rupture the lysosomal membrane. Therefore, membrane rupture was achieved using the ZAP function, which delivered a rapid voltage pulse (0,1–50 ms duration at −500 to −1,000 mV). Typically, the process began with a 0,1 ms pulse at −500 mV, applied up to five times before increasing the voltage to −550 mV if needed. A successful membrane rupture was indicated by two distinct capacitive transient peaks, which were compensated using the C-slow button in the HEKA Patch Master software.

### 3.3.4 Lysosomal voltage-clamp recording and analysis

In cells transfected with the YFP-tagged TPC2 plasmid, only YFP-positive lysosomes were selected for recording. Since different agonists and antagonists were added to the chamber to activate the TPC2 channel, only one lysosome was recorded per coverslip. To ensure even distribution of agonists or antagonists, gentle mixing steps were performed.

To characterize voltage-independent ion channels, a Ramp Protocol was applied to the clamped lysosomal membrane. This protocol gradually varied the membrane potential linearly from a user-defined starting value (−100 mV in this thesis) to a user-defined end value (+100 mV in this thesis), over a user-specified time span (500ms in this thesis). The Ramp Protocol was continuously applied until the current reached a steady state. Additionally, the STEP Protocol was used to investigate the voltage dependency of TPC2. In this protocol, the clamped membrane was subjected to a series of voltage steps (from −100 mV to +100 mV in 20 mV increments), with each step lasting for a defined duration (1000 ms) and a sweep interval of 10 seconds.

Patch-clamp recordings were conducted using a Patch Clamp EPC 10 USB amplifier (HEKA) and the PatchMaster software (HEKA). Whole-lysosome currents were digitized at 10 kHz and filtered at 2.9 kHz. All experiments were carried out at room temperature (21–23°C). Data recording and analysis were performed using the online analysis function of PatchMaster, Origin 6.1 (OriginLab) and Prism 10 software. The online analysis function in the PatchMaster software defined the current flowing through the channel as the mean value of the last five recorded currents in each Ramp cycle or STEP steps. Fast and slow capacitive transients were compensated by the EPC-10 amplifier’s built-in compensation circuit.

**Cytoplasmic (bath) solution**

| | |
|---|---|
| K-MSA | 140 mM |
| KOH | 5 mM |
| NaCl | 2 mM |
| $CaCl_2$ | 0.39 mM |
| EGTA | 1 mM |
| HEPES | 10 mM |

pH adjusted to 7.2 with KOH, sterilized by passing through a 0.2 µm filter.

**Luminal (pipette) solution**

| | |
|---|---|
| Na-MSA | 140 mM |
| K-MSA | 5 mM |
| $CaCl_2$ | 1 mM |
| Ca-MSA | 2 mM |
| HEPES | 10 mM |
| MES | 10 mM |

pH adjusted to 4.6 with MSA, sterilized by passing through a 0.2 µm filter.

For lysosomal patch-clamp experiments, stock solutions were prepared as follows: 100 mM ATP-Mg and 1 mM $PI(3,5)P_2$ in distilled water, and 10 mM TPC2-A1P in DMSO. All stock solutions were aliquoted and stored in tightly sealed vials at −20 °C.

## 3.4 Förster Resonance Energy Transfer (FRET)

For Förster Resonance Energy Transfer (FRET) experiments, 17 mm glass-bottom imaging dishes (Ibidi 81218-200) were pretreated with 0,1% Poly-L-Lysine for 2 hours.

HEK293 cells were seeded in the dishes two days before measurements. One day prior to imaging, cells were transfected using Lipofectamine 2000™.

Each FRET pair was transfected with 0.7 µg of donor plasmid DNA with mTurquoise2 constructs (For different FRET experiments mTq-Rab7, mTq-Rab7[QL], mTq-Rab5, mTq-CCZ1, CCZ1-mTq were used, respectively.) with 1.5 µg of acceptor plasmid DNA with mVenus constructs (hTPC2-mVenus), to balance the lower expression rates of channel proteins.

Live-cell imaging was conducted using a Zeiss LSM980 inverted confocal microscope equipped with a 60X oil immersion objective. Excitation wavelengths were set to 445 nm and 515 nm for mTurquoise2 and mVenus, respectively. Images were acquired with bidirectional line scans across three emission channels: mTq2DIRECT (445 nm excitation; 455–526 nm emission), mTq2FRET (445 nm excitation; 455–526 nm emission), and mVenusDIRECT (515 nm excitation; 526–561 nm emission).

Image analysis was performed in FIJI, applying a mild Gaussian blur for processing. Regions of interest (ROIs) were delineated around mVenus-positive lysosomes. A custom FIJI macro calculated the mean fluorescence intensity within each ROI across all channels and exported the data as a .csv file. Calibration constants were derived from cells expressing single mTurquoise2, single mVenus, and a tandem construct, respectively. FRET Two-Hybrid interaction curves were generated using a custom MATLAB function (MathWorks), with calculations based on the methodology described by Liu et al. [119] .

## 3.5 Western blot

Cells were initially washed three times with ice-cold PBS. Following the washes, 400 µL of lysis buffer was added to the cells. The cells were then scraped from the wells,

transferred into Eppendorf tubes, and incubated on ice for 30 minutes. After incubation, the cell suspensions were centrifuged at 13,200 rcf for 10 minutes at 4°C. The resulting supernatant was carefully transferred to a new Eppendorf tube, and protein concentration was measured using the Qubit Protein Assay kit, following the manufacturer's instructions.

An equal amount of protein from each condition was prepared by boiling in 6× Laemmli sample buffer supplemented with DTT at 72°C for 10 minutes. Proteins were subsequently separated by molecular weight using SDS-PAGE. A gradient gel with 6% and 12% polyacrylamide was prepared according to standard recipes, utilizing assembled glass plates with spacers (Bio-Rad). First, 4,25 mL of 12% gel solution was poured, followed by 4,25 mL of 6% gel solution, ensuring no air bubbles. To maintain a flat and horizontal resolving surface, 1 mL of isopropanol was layered on top. After setting, a 5% stacking gel solution was added to complete the SDS-PAGE gel assembly.

Samples containing 15 µg of protein in equal volumes were loaded into the SDS-PAGE wells. A PageRuler Prestained Protein Ladder (Thermo Fisher Scientific) was used as a molecular weight marker. Electrophoresis was conducted at 100 V for the first 20 minutes, followed by 150 V for an additional 40 minutes in electrophoresis buffer.

For protein transfer, a PVDF membrane was activated in methanol and prepared for use. Proteins were transferred onto the membrane using a Mini Trans-Blot Cell (Bio-Rad) in transfer buffer at a constant current of 350 mA for 1.5 hours. After transfer, the membrane was blocked at room temperature for 1 hour using blocking buffer, followed by overnight incubation with the primary antibody diluted in blocking buffer at 4°C.

The following day, the membrane was washed three times with TBST for 10 minutes per wash. It was then incubated with the secondary antibody, diluted in blocking buffer,

for 2 hours at room temperature, followed by three additional 10-minute washes in TBST. For signal detection, a chemiluminescent substrate, Western Blotting Luminol Reagent (Santa Cruz), was prepared and applied according to the manufacturer's instructions. Images were captured using the Chemidoc MP Imaging system (Bio-Rad) and analyzed with ImageLab software.

**Table1: Antibodies used for Western blot**

| Antibody | Source | Dilution |
|---|---|---|
| Mouse Anti-CCZ1 | Santa Cruz B-7: sc-514290 | 1:500 |
| Rabbit Anti-RMC1 | Proteintech 20111-1-AP | 1:1000 |
| Donkey Anti-Mouse IgG (H+L) | Jackson, 715-035-150 | 1:2000 |
| Donkey Anti-Rabbit IgG (H+L) | Jackson, 711-035-152 | 1:2000 |
| Rabbit Anti-GAPDH | Cell Signaling 14C10 | 1:1000 |
| Mouse Anti-HA | Cell Signaling 6E2 | 1:1000 |

**Lysis buffer**

| | |
|---|---|
| Triton X-100 | 2,5 mL |
| 5 M NaCl | 15 mL |
| 2,5 M $CaCl_2$ | 0,4 mL |
| $H_2O$ | add to 500 mL |

**6x Laemmli buffer**

| | |
|---|---|
| Tris-HCl pH 6,8 | 7 mL |
| Glycerol | 3 mL |
| SDS | 1,0 g |
| Bromophenol blue | 1,2 mg |

| | |
|---|---|
| DTT | 0,93 g |
| $H_2O$ | add to 10 mL |

**1x Electrophoresis buffer**

| | |
|---|---|
| Tris base | 3,03 g |
| Glycin | 14,4 g |
| SDS | 1,0 g |
| $H_2O$ | add to 1 L |

**4x 0,5 M Tris-HCl/SDS buffer**

| | |
|---|---|
| Tris base | 0,5 M |
| SDS | 0,4% |
| $H_2O$ | add to 500 mL |
| Adjust pH to 6,8 | |

**4x 1,5 M Tris-HCl/SDS buffer**

| | |
|---|---|
| Tris base | 1,5 M |
| SDS | 0,4% |
| $H_2O$ | add to 500 mL |
| Adjust pH to 8,8 | |

**Stacking gel (for 2 gels)**

| | |
|---|---|
| 30% acrylamide/bis-acrylamide | 1 mL |
| 4x 0,5 M Tris-HCl/SDS buffer | 1,9 mL |
| $H_2O$ | 4,6 mL |
| APS | 37,5 µL |
| TEMED | 7,5 µL |

**6 % Gradient separation gel (for 2 gels)**

| | |
|---|---|
| 30% acrylamide/bis-acrylamide | 2,3 mL |

| | |
|---|---|
| 4x Tris-HCl/SDS buffer 1,5 M | 2,8 mL |
| $H_2O$ | 6,2 mL |
| APS | 22,5 µL |
| TEMED | 7,5 µL |

**12% Gradient separation gel (for 2 gels)**

| | |
|---|---|
| 30% acrylamide/bis-acrylamide | 4,6 mL |
| 4x Tris-HCl/SDS buffer 1,5 M | 2,8 mL |
| $H_2O$ | 3,9 mL |
| APS | 22,5 µL |
| TEMED | 7,5 µL |

**Transfer buffer**

| | |
|---|---|
| Tris | 3,0 g |
| Glycin | 14,4 g |
| $H_2O$ | add to 1 L |

**TBST**

| | |
|---|---|
| Tris | 1,2 g |
| NaCl | 8 g |
| Tween 20 | 1 mL |
| $H_2O$ | add to 1 L |

**Blocking solution**

| | |
|---|---|
| TBST | 15 mL |
| Non-fat dried milk powder | 0,75 g |

## 3.6 Quantitative RT-PCR

Total RNA was isolated from cultured cells using the RNeasy Plus Mini Kit (Qiagen, Cat. 74134) according to the manufacturer's instructions. Cells were disrupted and homogenized in Buffer RLT Plus, purified through the gDNA Eliminator spin column, and finally eluted in RNase-free water. The concentration and purity of the extracted RNA were assessed using a NanoDrop 2000c spectrophotometer. For reverse transcription, cDNA was synthesized with the RevertAid First Strand cDNA Synthesis Kit (Thermo Fisher Scientific, Cat. K1622), following the manufacturer's protocol. Briefly, 150 ng of total RNA was combined with both Oligo(dT) and Random Hexamer primers for first-strand cDNA synthesis. PCR amplification of the resulting cDNA was performed in a ProFlex PCR system (Thermo Fisher Scientific) by adding 5x Reaction Buffer, RiboLock RNase Inhibitor, 10 mM dNTP Mix, and RevertAid M-MuLV Reverse Transcriptase.

Quantitative real-time PCR (qRT-PCR) was then conducted using the SYBR Select Master Mix (Applied Biosystems, Cat. 4472903) according to the manufacturer's guidelines. Each reaction contained 2× SYBR Select Master Mix, forward and reverse primers, cDNA template, and RNase-free water in a total volume of 20 µl on a 96-well plate. Three technical replicates were set up for each gene of interest, and the plate was processed on a QuantStudio™ Real-Time PCR System (Applied Biosystems). Relative gene expression levels were calculated using the $2^{-\Delta\Delta CT}$ method [120], with ACTIN serving as the housekeeping gene. All primers used in qPCR can be found in the appendix (Table 2)

## 3.7 Cell migration and proliferation assay

The cell migration assay was adapted from Abrahamian et al. [62] with partial modifications. 0,5 x $10^6$ SK-MEL5 WT and *CCZ1* KO cells, respectively, were seeded

into the upper chamber of 8µm pore size transwell inserts (Sigma Aldrich) in serum-free culture medium. The lower well of a 24–well plate was filled with culture medium with 10% FCS as a chemoattractant. Transwell inserts were placed in the 24-well plate and cultured for 24 h. After incubation, the non-migrated cells on top side of the transwell membrane were gently moved. Cells that had migrated to the underside of the membrane were fixed and stained with 0,5% crystal violet (Merck) in methanol (Carl Roth), imaged with EVOS M7000 and counted with ImageJ (NIH, Bethesda, MD). For experiments involving Rab7 plasmids transfection, cells were transfected four hours prior seeding into the transwell inserts. For treated cells, TPC2-A1P (10 µM) and SG-094 (7 µM) was added at the start of the experiment to both transwell insert and the 24-well plate.

Cell proliferation was evaluated using the xCELLigence Real-Time Cell Analysis (RTCA) system (ACEA Biosciences), which provides continuous measurements of the doubling time and cell index—the latter being a dimensionless parameter correlated with cell number. Equal numbers of SK-MEL5 WT and *CCZ1* KO cells were seeded into a 16-well E-plate (OLS, #300601140) that had been equilibrated according to the manufacturer's instructions. After an initial 30-minute reading, the system was paused to allow addition of TPC2-A1P (10 µM) or SG-094 (7 µM), and then measurements were resumed. SG-094 was dissolved in DMSO as a 7mM stock solution and TPC2-A1P in DMSO as a 10 mM stock solution.

## 3.8 Statistics

All data are presented as mean ± SEM, with each point corresponding to one measurement of experiments. Statistical analysis was performed using GraphPad Prism 7 or Origin 8. P-values were calculated using Student's t-test, Kruskal-Wallis test

or one-way ANOVA followed by Tukey's multiple comparisons test. $P < 0.05$ was considered statistically significant; *$P < 0.05$, **$P < 0.01$, ***$P < 0.001$, and ns indicates no significant difference.

# 4. Results

## 4.1 Genetic deletion of *CCZ1* and *RMC1* in HEK 293 and SK-MEL5 cell lines.

MON1 and CCZ1 form a dimer that constitutes the functional core of the MCC complex. Consequently, the loss of either MON1 or CCZ1 completely abolishes MCC activity [23]. Given their functional complementarity, this thesis focuses on the effects of *CCZ1* knockout on TPC2 function in HEK 293 and SK-MEL5 cell lines.

HEK 293 cells were used to assess TPC2 channel activity via lysosomal patch-clamp recordings [121], while SK-MEL5, a melanoma cell line with substantial endogenous Rab7 and TPC2 expression, was employed for functional assays such as migration and proliferation tests [62].

Additionally, *RMC1* KO HEK 293 and SK-MEL5 cell lines were generated to investigate the role of RMC1, the third component of the vertebrate MCC. Recent studies suggest that RMC1 primarily stabilizes the CCZ1/MON1 complex rather than directly contributing to MCC function. Supporting this hypothesis, the effects observed upon *RMC1* loss can be attributed to a reduction in CCZ1/MON1 levels [12, 24].

Human CCZ1 protein is encoded by a duplicated locus on chromosome 7 displaying identical nucleotide sequence and exon-intron structure (*CCZ1* and *CCZ1b*)**.** A CRISPR-Cas9 approach was employed to inactivate both copies of the gene by designing two sgRNAs targeting exons 11 and 12, respectively, with the goal of deleting the 992 bp sequence between them.

A primer pair, who is separated by 1544bp, was designed to flank these two cut sites. A successful deletion of 992bp resulted in a single band at 552bp **(Figure 10A)**. PCR results confirmed the successful deletion in both alleles of HEK 293 and SK-MEL5 cell

lines, as indicated by the presence of a 552 bp band and the absence of the 1544 bp band (**Figures 10B-C**). Protein extracted from these single cell clones was analyzed via Western blot, where the complete loss of CCZ1 protein expression was demonstrated by the absence of a 56 kDa band, as shown in **Figure 10B** and **Figure 10C**.

The human *RMC1* gene has five annotated splicing variants. To ensure that functional RMC1 protein is no longer produced, exon 10, which is part of the open reading frame shared by all splicing variants, was selected for CRISPR-Cas 9 targeting (**Figure 11A**). This design leverages the non-homologous end joining (NHEJ) repair pathway to induce small insertions or deletions (indels) that would cause a frameshift, resulting in a premature stop codon. Both alleles were sequenced to confirm the edits. Insertions are highlighted in red, while deletions are indicated with transverse lines, as shown in **Figures 11B** and **11C**. Western blot analysis demonstrated the complete absence of RMC1 protein, confirming successful knockout at the protein level in both cell types (**Figures 11B, 11C**).

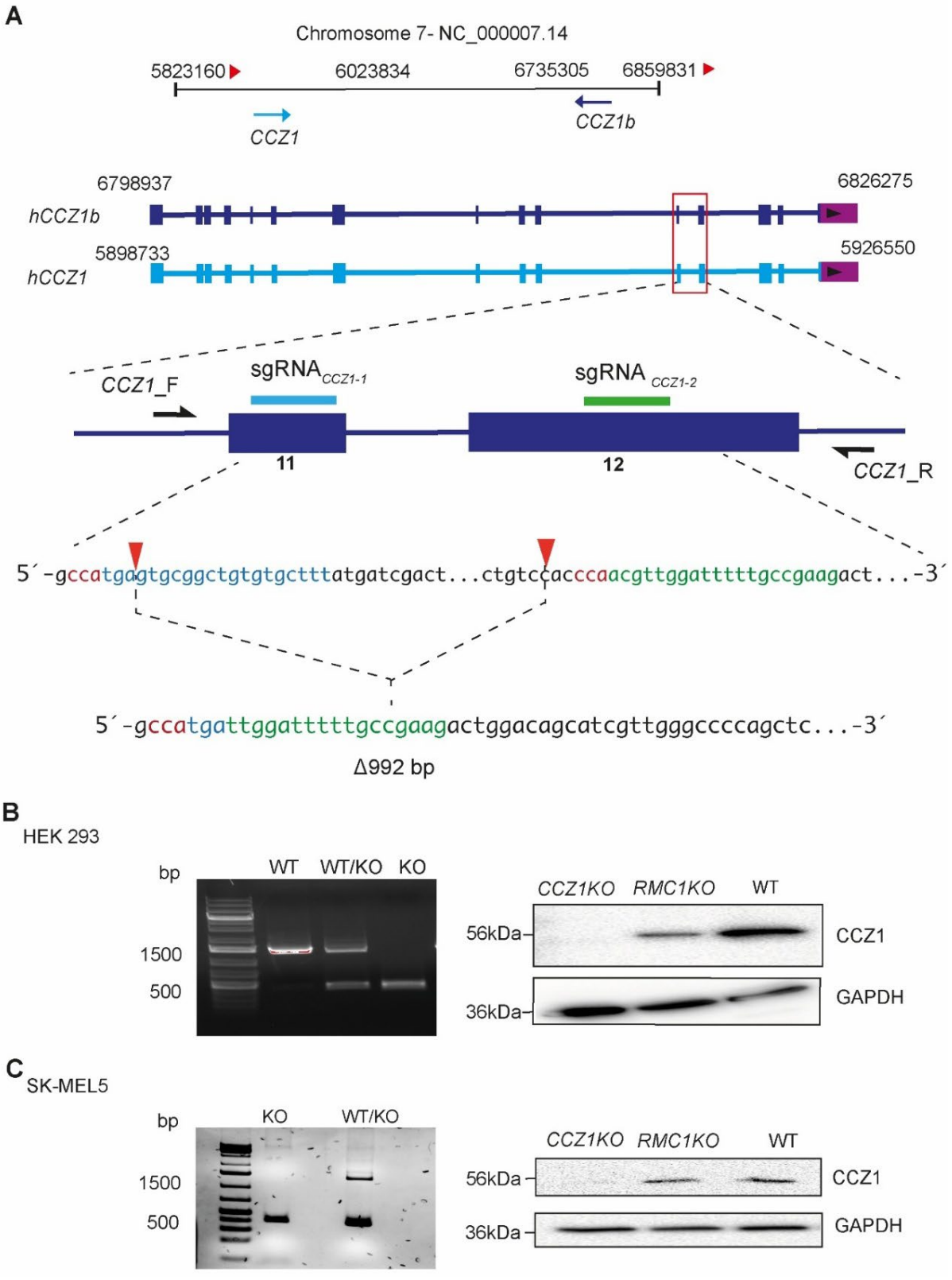


**Figure 10 Genetic deletion of *CCZ1* in HEK 293 and SK-MEL5 cell lines**

(**A**) Cartoon showing the relative localization of *CCZ1* and *CCZ1b* genes: The *CCZ1* gene is located at chr7:5898733-5926550, whereas *CCZ1b* is positioned at chr7:6798937-6826275, separated by a genomic distance of 872.384 bp. *CCZ1* and *CCZ1b* share the same intron-

exon structure, the same CDS length of 1449 nucleotides and encode proteins consisting of 482 amino acids. Two sgRNAs were designed to target exon 11 and exon 12 of both *CCZ1* copies and caused a deletion of 992 bp. Two primers were positioned upstream and downstream of two sgRNAs with a distance of 1544bp. A successful sequence deletion between two sgRNAs leaded to truncated length between two primers of 552bp. Cut sites are indicated as red arrows. (**B, C**) On the left are PCR results of HEK 293 and SK-MEL5 cells using CCZ1 primer pair from section 3.2.3. The lanes showing a single band at around 1544 bp, indicates unedited alleles, the lanes showing additional band at 552bp, indicates a heterogenous editing, only the lanes showing a single band at around 552bp, indicates editing at both alleles. On the right are the WB results in HEK 293 and SK-MEL5 cells, the absence of a band at 56kDa indicates the successful knock out of *CCZ1*.

Interestingly, Western blot analysis revealed that CCZ1 protein expression was significantly reduced in the *RMC1* KO HEK 293 cell line (**Figure 10B**). Similarly, RMC1 protein expression was substantially diminished in both *CCZ1* KO cell lines (**Figures 11B, 11C**), suggesting a reduced stability of the RMC complex, if one of its components is absent. RMC1 expression was also reduced in *CCZ1* KO SK-MEL5 cells (**Figure 10C**) while the deletion of RMC1 only slightly, if at all, reduced CCZ1 levels. This indicated that CCZ1 is less prone to degradation in *RMC1* KO SK-MEL-5 cells or, alternatively that these cells contain other proteins that stabilize CCZ1 in the absence of RMC1.

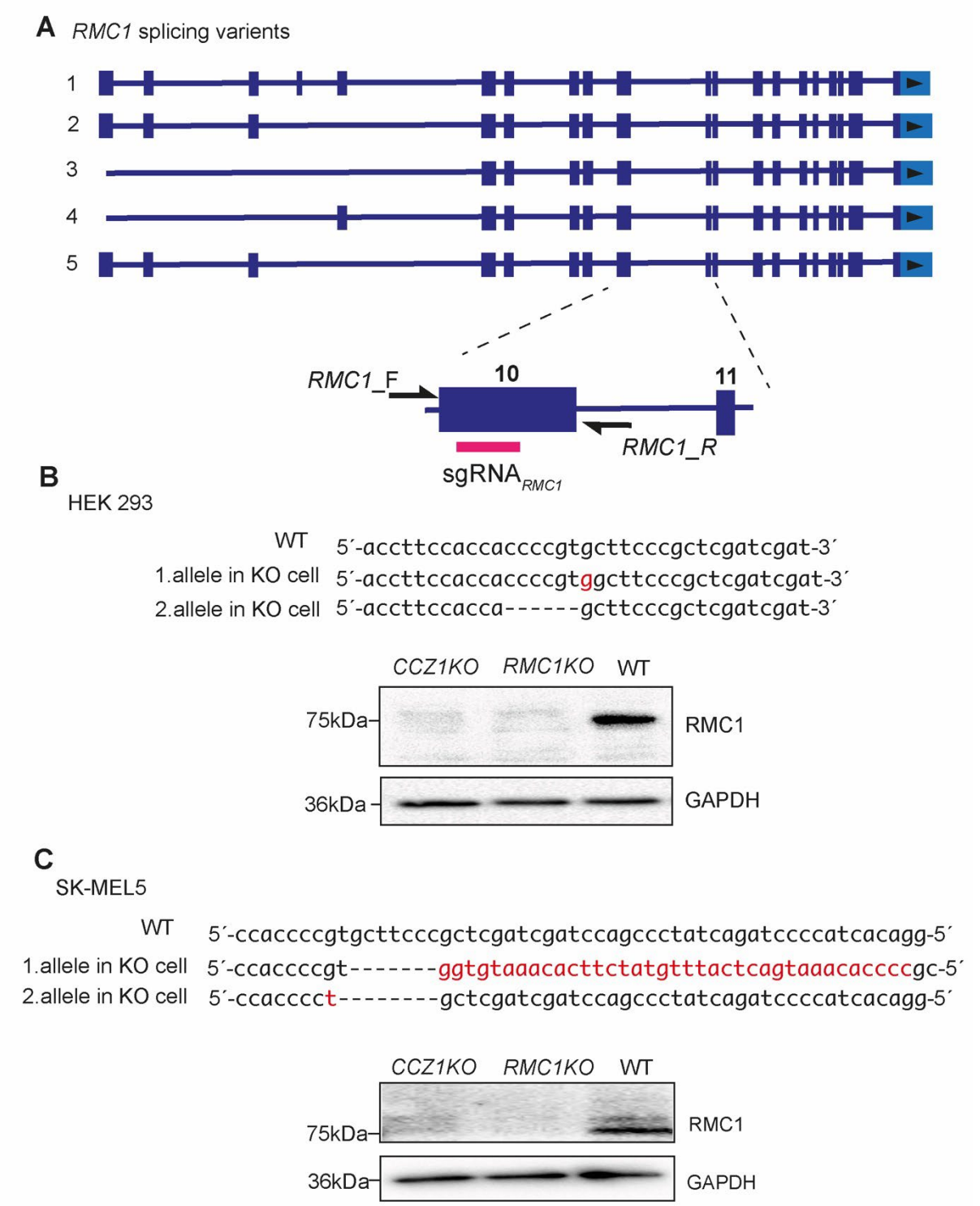


**Figure 11 Genetic deletion of *RMC1* in HEK 293 and SK-MEL5 cell line**

(**A**) Cartoon showing exons arrangement of 5 *RMC1* splicing variants. sgRNA was designed to target exon 10 with a primer pair flanking the designed cut site. (**B**) Sanger sequencing results of both alleles of *RMC1* KO cells in HEK 293. Deleted sequences shows in transverse lines and inserted sequences is highlighted in red. Western blot of RMC1 protein in WT, *CCZ1* KO, *RMC1* KO HEK 293 cells, the absence of band at 75 kDa indicated a successful deletion of protein. (**C**) Sanger sequencing results of both alleles of *RMC1* KO cells in SK-MEL5 cell

line, deleted sequences shows in transverse lines and inserted sequences is highlighted in red. Western blot of RMC1 protein in WT, *CCZ1* KO, *RMC1* KO SK-MEL5 cell line, the absence of band at 75 kDa indicated a successful deletion of protein.

## 4.2 Characterization of distribution of TPC2 in *CCZ1* Knockout HEK 293 cells

Before starting functional investigations, the endosome size and TPC2 distribution were analyzed in generated knockout cell lines. After overexpressing hTPC2-YFP in HEK293 WT and *CCZ1* KO cells, the cells were treated overnight with 1 µM apilimod, a specific PIKfyve inhibitor [114], to specifically enlarge late endosomes and lysosomes. Quantitative analysis revealed a significant increase in the diameter of hTPC2-YFP positive vesicles in *CCZ1* KO cells compared to WT controls (**Figures 12A-B**).

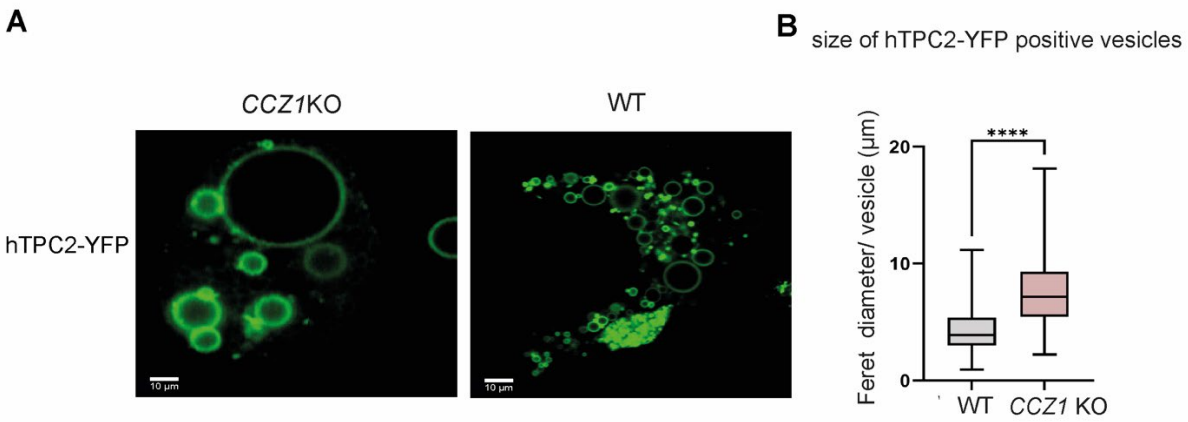


**Figure 12 Size of enlarged hTPC2-YFP positive vesicles in HEK 293WT and *CCZ1* KO cells**

(**A**) Representative confocal imaging of hTPC2-YFP (green) in HEK 293 WT and *CCZ1* KO cells after overnight incubation with 1µM apilimod, with a scale bar of 10µm. (**B**) Feret diameter of hTPC2-YFP positive enlarged vesicles was measured in WT and *CCZ1* KO cells and statistically analyzed with Kruskal-Wallis test; ****p<0.001.

Next, the subcellular distribution of TPC2 in HEK293 WT and *CCZ1* KO cells was assessed by co-expressing hTPC2-YFP with mCherry-LAMP1, a lysosomal marker. Following overnight incubation with 1 µM apilimod, confocal imaging showed that TPC2 and LAMP1 colocalized similarly in both *CCZ1* KO and WT cells (**Figure 13A**), consistent with TPC2's lysosomal localization.

Subsequently, hTPC2-YFP was co-expressed with mCherry-Rab5, an early endosome marker, in WT, *CCZ1* KO, and *RMC1* KO HEK293 cells. While TPC2 colocalization with Rab5 remained minimal in WT and *RMC1* KO cells, *CCZ1* KO cells displayed increased TPC2–Rab5 colocalization (**Figure 13B**). This raised the question whether the loss of *CCZ1* may trigger a physical interaction between Rab5 and TPC2, which was not reported in WT cells. To clarify this issue, FRET assays were performed in HEK293 WT and *CCZ1* KO cells overexpressing hTPC2-mVen and mTq-Rab5.

Although TPC2 and Rab5 seemed to colocalize more, FRET efficiency stayed very low and showed no significant difference between WT and CCZ1 KO cells (Figures 13C-D). In summary, CCZ1 knockout does not interfere with TPC2's lysosomal localization but redirects a portion of TPC2 to early endosomes. Despite this altered distribution, TPC2 and Rab5 do not appear to form a direct interaction, as indicated by a mean FRET efficiency below 5 % in both cell lines (Figure 13D). The low FRET efficiency implies that only 5% energy from hTPC2-mVen (doner) is transferred to mTq-Rab5 (acceptor), meaning only 5% of both proteins are within ~10nm distance necessary for strong interaction

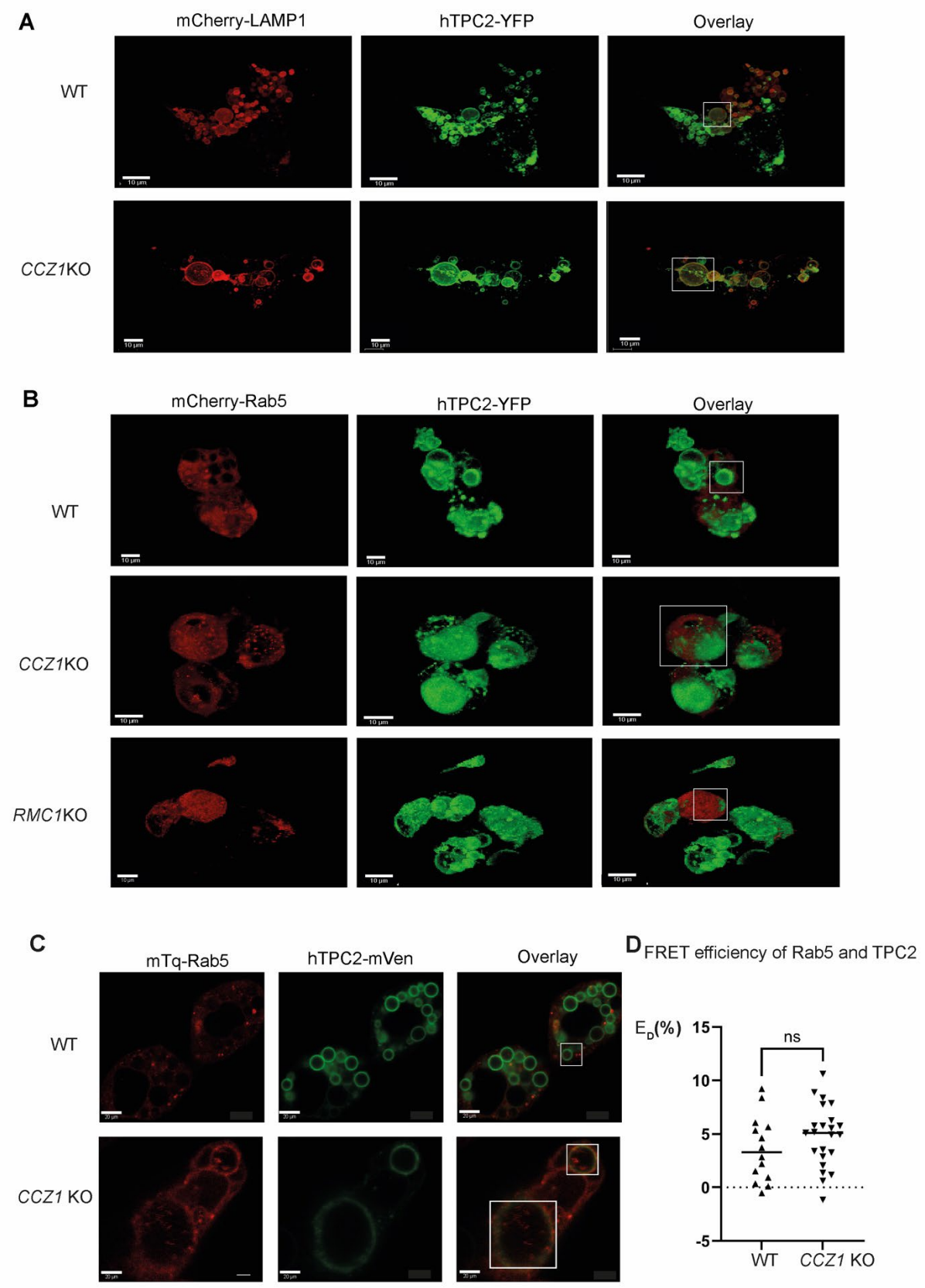


**Figure 13 Distribution of enlarged hTPC2-YFP positive vesicle of HEK 293 WT and *CCZ1* KO cells**

Cells were incubated overnight with 1 µM apilimod to specifically enlarge late endosomes and lysosomes. (**A**) hTPC2-YFP and mCherry-LAMP1 were overexpressed in HEK 293 WT and *CCZ1* KO cells. Confocal imaging revealed the localization of hTPC2-YFP (green), mCherry-LAMP1 (red), and their overlay. White boxes highlight hTPC2 positive vesicles that colocalized with LAMP1 in *CCZ1* KO and WT cells. (**B**) hTPC2-YFP and mCherry-Rab5 were overexpressed in HEK 293T WT, *CCZ1* KO, and *RMC1* KO cells. Confocal images showed TPC2 (green), Rab5 (red), and their overlay. White boxes highlight hTPC2 positive vesicles that didn´t colocalized with Rab5 in WT cells but do colocalized in *CCZ1* KO cells. (**C**) hTPC2-mVen and mTq-Rab5 were overexpressed in HEK 293 WT and *CCZ1* KO cells. Confocal imaging revealed TPC2 (green), Rab5 (red), and their overlay. Enlarged vesicles containing hTPC2-mVen without mTq-Rab5 in WT cells and with mTq-Rab5 in *CCZ1* KO cells are highlighted in white boxes. (**D**) FRET efficiency between hTPC2-mVen (donor) and mTq-Rab5 (acceptor) in HEK WT and *CCZ1* KO cells was statistically analyzed using a two-tailed t-test; *ns* indicates no significant difference. Scale bar is 10µm in (**A, B**) and 20 µm in (**C**)**.**

## 4.3 Knockout of *CCZ1* and *RMC1* disrupts Rab7-TPC2 interaction.

To investigate the role of MCC in Rab7-mediated TPC2 function, the interaction between Rab7 and TPC2 in HEK293 WT, *CCZ1* KO and *RMC1* KO cells was studied using immunofluorescence and FRET analysis by overexpressing hTPC2-mVen and mTq-Rab7. In WT cells, overexpressed Rab7 (red) and TPC2 (green) colocalized extensively, as indicated by the overlay images and a high FRET efficiency, suggesting robust interaction (**Figures 14A-B**). In contrast, FRET efficiency was profoundly reduced in *CCZ1* KO cells indicating that the absence of CCZ1 impaired Rab7-TPC2 interaction (**Figures 14C-D**).

In *RMC1* KO cells, colocalization was also significantly diminished, however, a very weak FRET signal remained detectable (**Figures 14E-F**). This observation is aligned with the fact that deletion of *RMC1* leads to a strong reduction of CCZ1 protein amounts (**Figure 10B).**

Together, these data suggested that the interaction efficiency between Rab7 and TPC2 reflects the amount of CCZ1 protein and varies between zero (*CCZ1* KO) and one (WT), with the low amounts of CCZ1 as present in *RMC1* KO allowing only a weak

interaction. Given this quantitative relationship subsequent experiments were focused on the *CCZ1* knockout model.

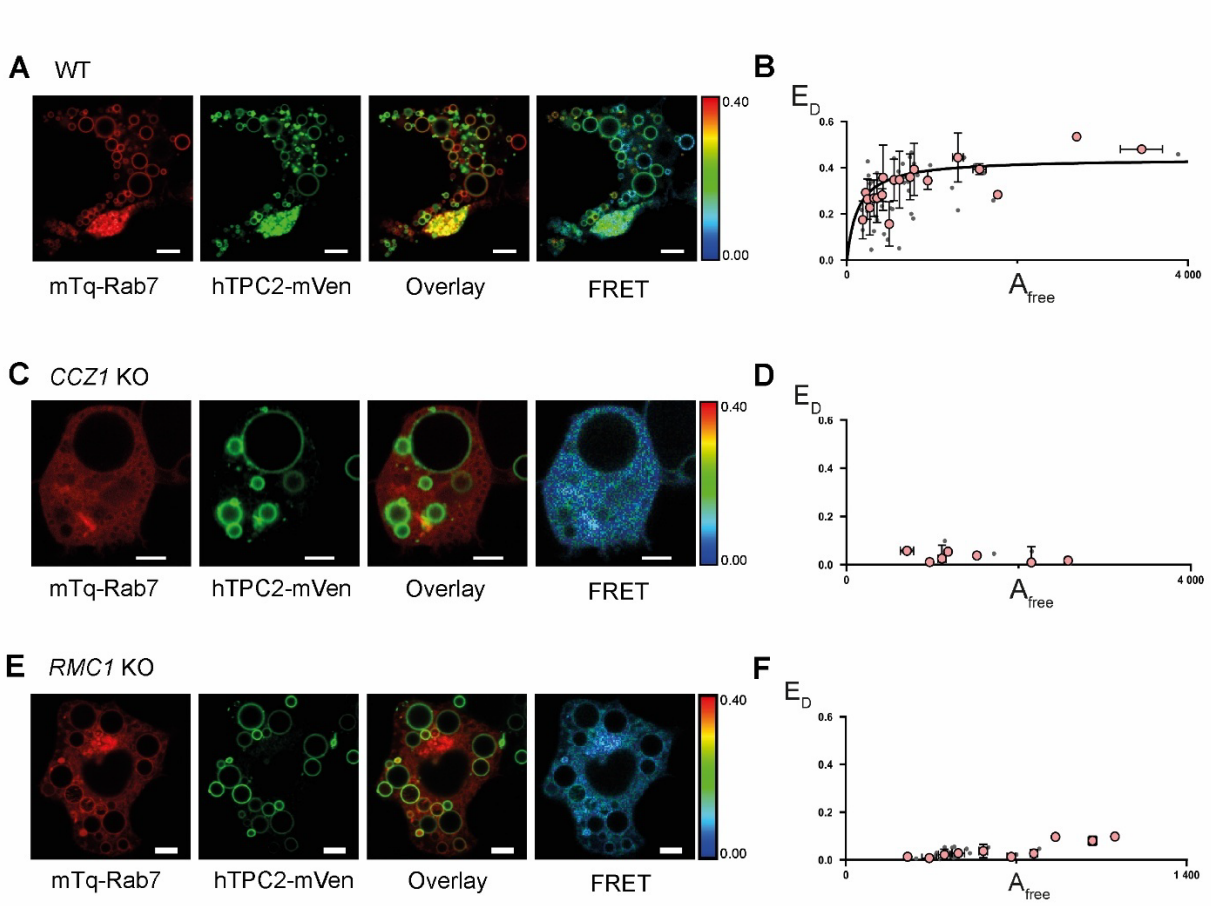


**Figure 14 Defect MCC function disrupts Rab7-TPC2 interaction**

**(A, C, E)** Immunofluorescence imaging of overexpressed mTq-Rab7 (red) and hTPC2-mVen (green) in HEK 293T WT (**A**), *CCZ1* KO (**C**) and *RMC1* KO (**E**) cells. The third panel shows the overlay of mTq-Rab7 and hTPC2-mVen. Cells were treated with apilimod (1 µM, overnight). FRET efficiency based on donor lifetime measurements, is shown in the rightmost panel, with a color scale representing the FRET efficiency. **(B, D, F)** Binding curve of hTPC2-mVen interacting with mTq-Rab7 in WT (**B**), *CCZ1* KO (**D**), and *RMC1* KO cells (**F**).

## 4.4 Knockout of *CCZ1* abolishes the stimulatory effect of Rab7 on TPC2 channel activity

Whole-endolysosome patch-clamp recordings were conducted to directly assess the functional impact of *CCZ1* knockout on TPC2 currents. hTPC2-YFP was overexpressed in HEK293 WT and *CCZ1* KO cells, followed by an overnight treatment with 1 µM vacuolin-1, which enlarged endosomes and lysosomes to facilitate patch-clamp measurements [122].

In WT cells, $PI(3,5)P_2$ stimulation produced a robust TPC2 current (~0.5 nA at –100 mV), which could be inhibited by ATP [90]. mCherry-Rab7 co-expression significantly enhanced $PI(3,5)P_2$-evoked TPC2 current, tripling the current density to ~1.5 nA at –100 mV, consistent with prior findings that Rab7 augments $PI(3,5)P_2$-dependent TPC2 currents [62] (**Figures 15A-C**). In contrast, in *CCZ1* KO cells, TPC2 current density reached ~1 nA at –100 mV even without mCherry-Rab7 overexpression, and mCherry-Rab7 co-expression conferred no additional stimulatory effect (**Figures 15D–E**). Quantitative analysis showed no significant difference in current density at –100 mV between *CCZ1* KO cells with or without Rab7 (**Figure 15F**), indicating that CCZ1 is essential for Rab7-mediated enhancement of TPC2 activation.

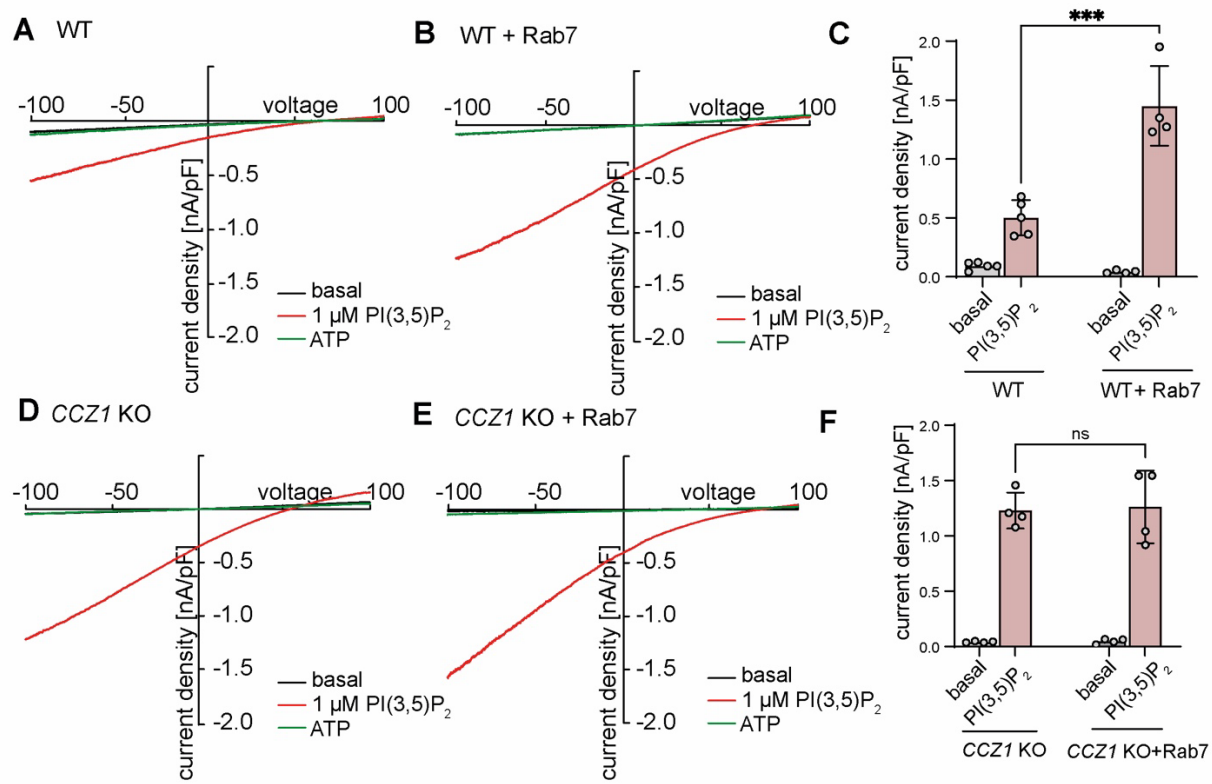


**Figure 15 Knockout of *CCZ1* abolishes Rab7 mediated enhancement on TPC2 current**

(**A-B, D-E**) Whole-endolysosome patch-clamp recordings of hTPC2-YFP currents in HEK293 WT and *CCZ1* KO cells, showing basal (black), ATP (green), and $PI(3,5)P_2$ (red)-stimulated current densities. (**A-B**) Representative current-voltage (I-V) relationships in WT cells in the absence (**A**) and presence (**B**) of mCherry-Rab7 co-expression. (**C**) Quantification of current densities at -100 mV from endolysosomal recordings in (**A-B**). (**D-E**) Representative current-voltage (I-V) relationships in *CCZ1* KO cells in the absence (**D**) and presence (**E**) of mCherry-Rab7 co-expression. (**F**) Quantification of current densities at -100 mV from endolysosomal recordings in (**C**, **F**). Data are presented as mean ± s.e.m. Statistical significance was determined using two-way ANOVA with Bonferroni post-hoc tests. ***p<0.001; ns, not significant.

## 4.5 Rescue of Rab7-TPC2 interaction

To confirm that the loss of Rab7-TPC2 interaction in *CCZ1* KO and *RMC1* KO cells is due to the absence of CCZ1 and RMC1 proteins and not caused by some non-specific effects caused by the generation of knock out cell lines, these proteins were separately reintroduced into *CCZ1* KO and *RMC1* KO cells and the Rab7-TPC2 interaction was tested. Immunofluorescence analysis showed restored colocalization of mTq-Rab7 and hTPC2-mVen in both KO cell lines, and FRET efficiency in *CCZ1* KO cells was

comparable to that in WT cells (**Figures 16A-C**). Functionally, re-expression of CCZ1 rescued the $PI(3,5)P_2$-induced hTPC2-YFP currents in *CCZ1* KO cells to levels similar to WT cells (**Figures 16D-F**). These results confirm that CCZ1 is required for Rab7-TPC2 interaction and subsequent TPC2 activation.

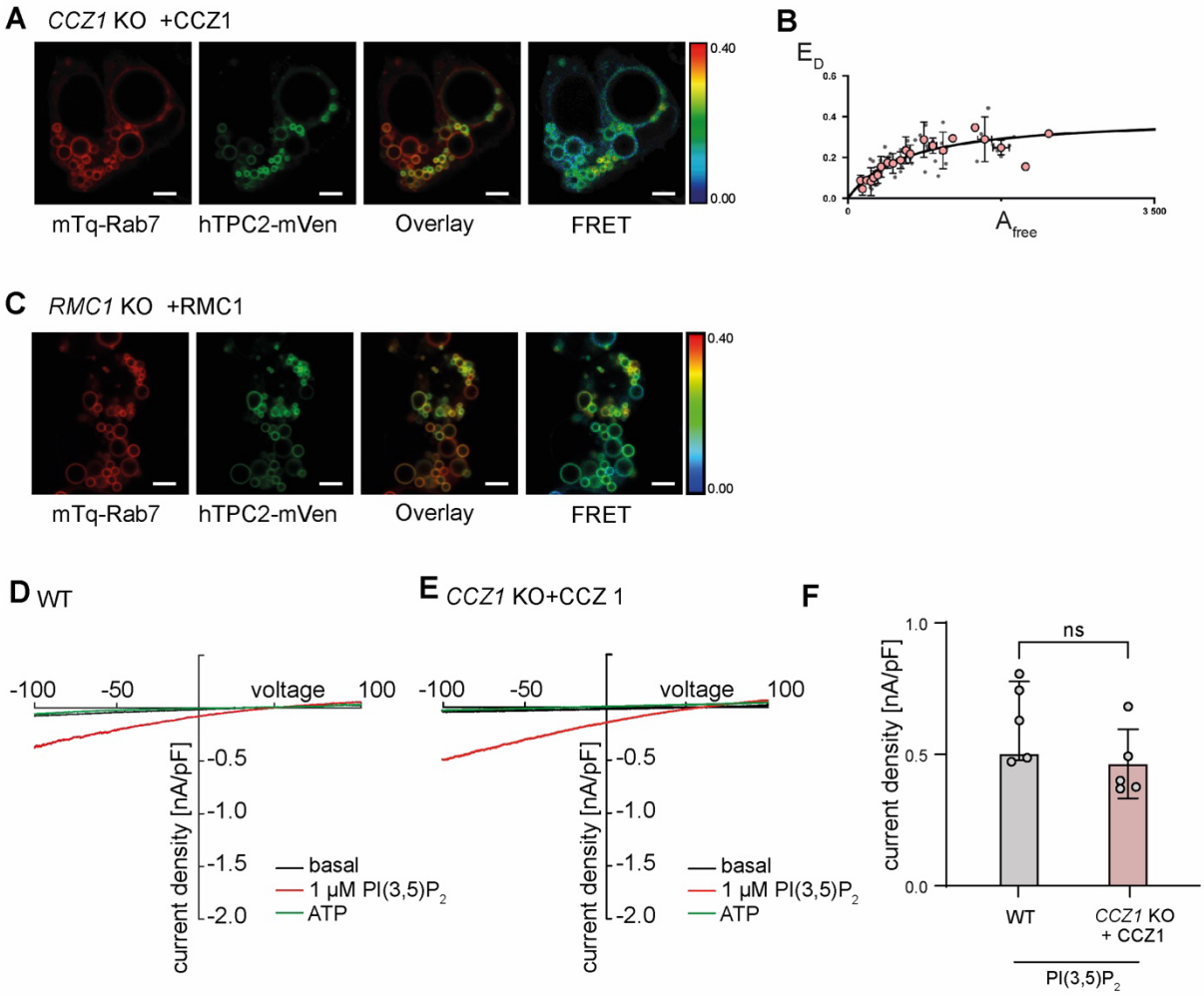


**Figure 16 Rab7-TPC2 interaction can be rescued in both knockout cells by re-expression of the lacking proteins**

(**A, C**) Immunofluorescence imaging of overexpressed mTq-Rab7 (red) and hTPC2-mVen (green) in *CCZ1* KO HEK293 cells co-expressing mCherry-CCZ1 (**A**), or HA-RMC1 (**C**). The third panel shows the overlay of mTq-Rab7 and hTPC2-mVen. Cells were treated with apilimod (1 µM, 16 h) before imaging. FRET efficiency, based on donor lifetime measurements, is shown in the rightmost panel, with a color scale representing the FRET efficiency. (**B**) Binding curve of hTPC2-mVen interacting with mTq-Rab7 in *CCZ1* KO with co-expression of mCherry-CCZ1. (**D-E**) Whole-endolysosome patch-clamp recordings of hTPC2-YFP currents in WT (**D**) and in *CCZ1* KO cells co-expressing mCherry-CCZ1(**E**), showing basal (black), ATP (green), and $PI(3,5)P_2$ (red)-stimulated current densities. (**F**) Quantification of current densities at -100 mV from endolysosomal recordings in *CCZ1* KO cells co-expressing mCherry-CCZ1 (red bar),

compared to WT cells. Data are presented as mean ± s.e.m. Statistical significance was determined using two-way ANOVA with Bonferroni post-hoc tests. ns, not significant.

## 4.6 Constitutively active Rab7[QL] mutant does not alter TPC2 currents in *CCZ1* knockout cells

The loss of the Rab7-TPC2 interaction in the absence of CCZ1 may be explained by the fact that Rab7 requires CCZ1 to transition into its active GTP-bound form. If this hypothesis is correct, the constitutively active Rab7[QL] mutant, which mimics the GTP-bound state, should bypass the need for CCZ1 in TPC2 activation. The Rab7[QL] mutant is a well-characterized Rab7 variant where a glutamine-to-leucine substitution at position 67 (Q67L) prevents GTP hydrolysis, thereby locking Rab7 in its active, GTP-bound state. Immunofluorescence imaging and FRET analysis showed colocalization of overexpressed mTq-Rab7[QL] and hTPC2-mVen in WT cells, along with robust FRET efficiency, indicating strong interaction (**Figures 17A-B**). However, in *CCZ1* KO cells, mTq-Rab7[QL] and hTPC2-mVen exhibited very little colocalization, and FRET efficiency was significantly reduced, suggesting that the interaction between Rab7[QL] and TPC2 was still compromised in the absence of CCZ1 (**Figures 17C-D**). In agreement with this limited colocalization between Rab7[QL] and hTPC2 in *CCZ1* KO cells, whole-endolysosome patch-clamp recordings revealed that co-expression of mCherry-Rab7[QL] failed to enhance hTPC2 currents (**Figures 17F-H**). In *RMC*1 KO cells, the FRET between Rab7[QL] and hTPC2 was reduced compared to WT cells but remained stronger than in *CCZ1* KO cells (**Figure 17E**). This observation is consistent with the residual CCZ1 levels in *RMC1* KO cells (**Figure 10B**), which partially maintains the interaction.

Together, these results indicate that CCZ1 plays a critical role beyond simply facilitating Rab7 activation, and its presence is required for the functional coupling between Rab7 and TPC2.

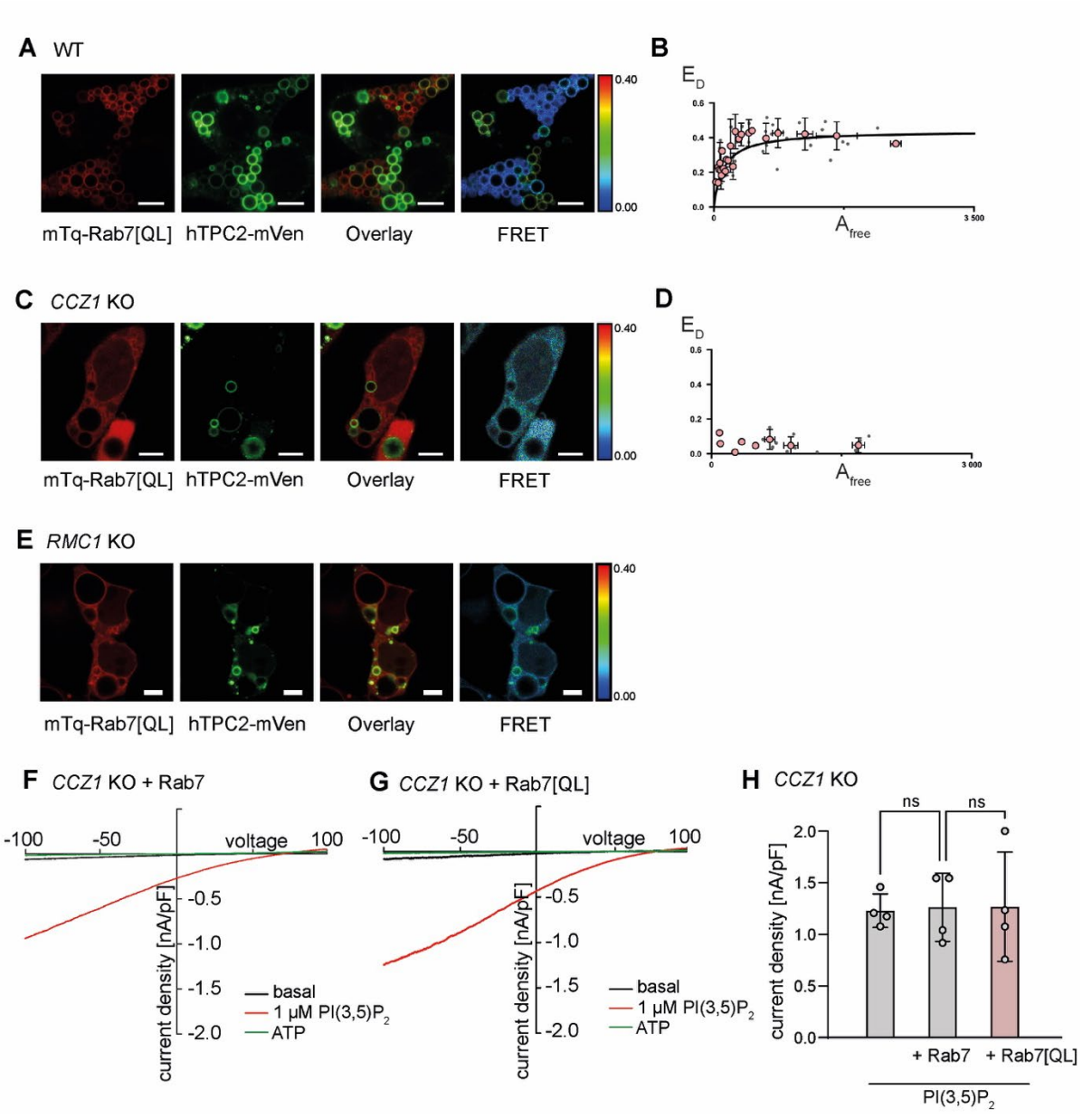


**Figure 17 The constitutively active Rab7[QL] mutant does not alter TPC2 currents in *CCZ1* knockout cells**

(**A-E**) Immunofluorescence imaging of mTq-Rab7[QL] (red) and hTPC2-mVen (green) in WT (**A**) and *CCZ1* KO (**C**) and *RMC1* KO (**E**) HEK 293 cells. The third panel shows the overlay of Rab7[QL] and hTPC2. Cells were previously treated with apilimod (1 µM, 16 h). FRET efficiency, based on donor lifetime measurements, is shown in the rightmost panel, with a color scale representing the FRET efficiency. Binding curve of hTPC2-mVen interacting with mTq-

Rab7[QL] in WT (**B**) and *CCZ1* KO (**D)**. **(F-H)** Whole-endolysosome patch-clamp recordings of hTPC2-YFP currents in *CCZ1* KO cells with coexpression of Rab7 (**F**) or Rab7[QL] (**G**), showing basal (black), ATP (green), and $PI(3,5)P_2$ (red)-stimulated current densities. (**H**) Quantification of current densities at -100 mV from endolysosomal recordings in *CCZ1* KO cells co-expressing hTPC2-YFP with Rab7[QL] (pink bar) compared to cells co-expressing Rab7 (grey bar) from Figure 15B. Data are presented as mean ± s.e.m. Statistical significance was determined using two-way ANOVA with Bonferroni post-hoc tests. ns, not significant.

## 4.7 *CCZ1* knockout enhances TPC2 sensitivity to $PI(3,5)P_2$

Given that CCZ1 functions beyond its role as a Rab7 GEF in the Rab7-TP2 interaction, it is possible that CCZ1 may also regulate lysosomal TPC2 currents independently of Rab7. To investigate this possibility, the dose-response curve of TPC2 to $PI(3,5)P_2$ was determined in WT and *CCZ1* KO cells.

hTPC2-YFP was overexpressed in WT and *CCZ1* KO cells followed by overnight incubation of apilimod for inhibiting endogenous synthesis of $PI(3,5)P_2$ [123]. Different concentrations of $PI(3,5)P_2$ were applied exogenously to the cell. In WT cells, $PI(3,5)P_2$ induced a dose-dependent increase in TPC2 currents, with a maximal response at 100 µM (**Figure 18A**), and the current continued to rise during depolarization. By contract, the TPC2 current in *CCZ1* KO cells displayed a distinctive `spoon-shaped` current response when activated by $PI(3,5)P_2$ concentrations greater than 1 µM (**Figure 18B**), where the rate of current increase plateaued at high depolarizing potentials. These findings indicated a voltage dependency of TPC2 in *CCZ1* KO cells that is not observed in WT cells.

Moreover, TPC2 showed significantly increased currents across concentrations ranging from 1 to 100 µM in dose response curve in *CCZ1* KO cells compared with WT cells (**Figure 18C**). The EC50 value for $PI(3,5)P_2$ shifted to a lower concentration in *CCZ1* KO cells compared to WT cells ($EC50_{WT}$: 0, 6779 µM; $EC50_{CCZ1KO}$: 0,2743 µM), suggesting increased sensitivity of TPC2 in *CCZ1* KO cells. Remarkably, the maximal

current response in *CCZ1* KO cells was approximately 50% higher compared to WT cells, indicating a substantial enhancement in TPC2 activity due to *CCZ1* deletion.

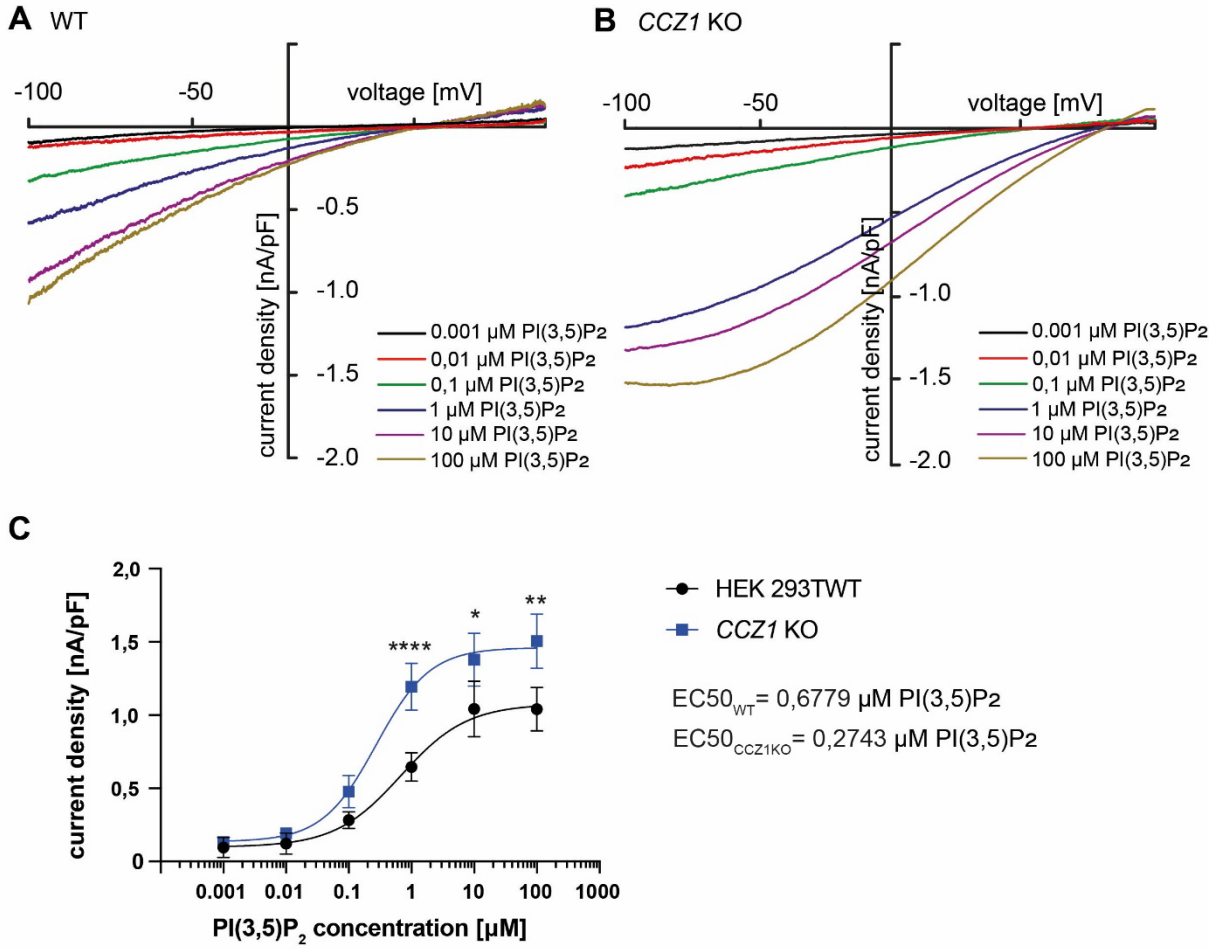


**Figure 18 *CCZ1* knockout enhances TPC2 sensitivity to PI(3,5)$P_2$**

(**A-B**) Whole-endolysosome patch-clamp recordings of hTPC2-YFP currents in WT (**A**) and *CCZ1* KO (**B**) HEK293 cells in response to varying concentrations of PI(3,5)$P_2$ (0,001 µM, 0,01 µM, 0,1 µM, 1 µM, 10 µM, 100 µM) after overnight incubation of apilimod. Current density-voltage (I-V) relationships are shown for each condition. (**C**) Dose-response curve comparing the current densities at -100mV induced by increasing concentrations of PI(3,5)$P_2$ in WT (black) and *CCZ1* KO (blue) cells. Data are presented as mean ± s.e.m, statistical significance was determined using unpaired t test (two-tailed), *p<0.05, **p<0.01, ****p<0.0001.

## 4.8 Voltage-dependent response of TPC2 currents in *CCZ1* knockout cells

The voltage-dependence of TPC2 currents in WT and *CCZ1* KO cells was further analyzed using a step pulse protocol. In WT cells, 1 µM and 10 µM $PI(3,5)P_2$ induced robust peak ($I_p$) and steady-state ($I_s$) currents. The corresponding I-V relationships exhibited typical voltage-independent behavior (**Figures 19A-B, 19H-I**).

In *CCZ1* KO cells, however, TPC2 currents during membrane hyperpolarization reached a peak ($I_p$) before decaying to a steady state ($I_s$) by the end of the pulse (**Figures 19C-D, 19J-K**). This decay suggested a desensitization of TPC2 currents to ligands under hyperpolarized potentials in the absence of CCZ1. Quantitative analysis of the $I_p/I_s$ ratio revealed a significant increase in *CCZ1* KO cells compared to WT cells if TPC2 was activated by 10 µM $PI(3,5)P_2$ (**Figure 19L**), indicating that CCZ1 may influence the voltage-dependent regulation of TPC2. However, a similar desensitization pattern was observed in WT cells when Rab7 was co-expressed (**Figures 19F-G**), suggesting that *CCZ1* deletion itself is not responsible for the desensitization. Instead, the desensitization may be an intrinsic property of the maximally activated of TPC2 channel.

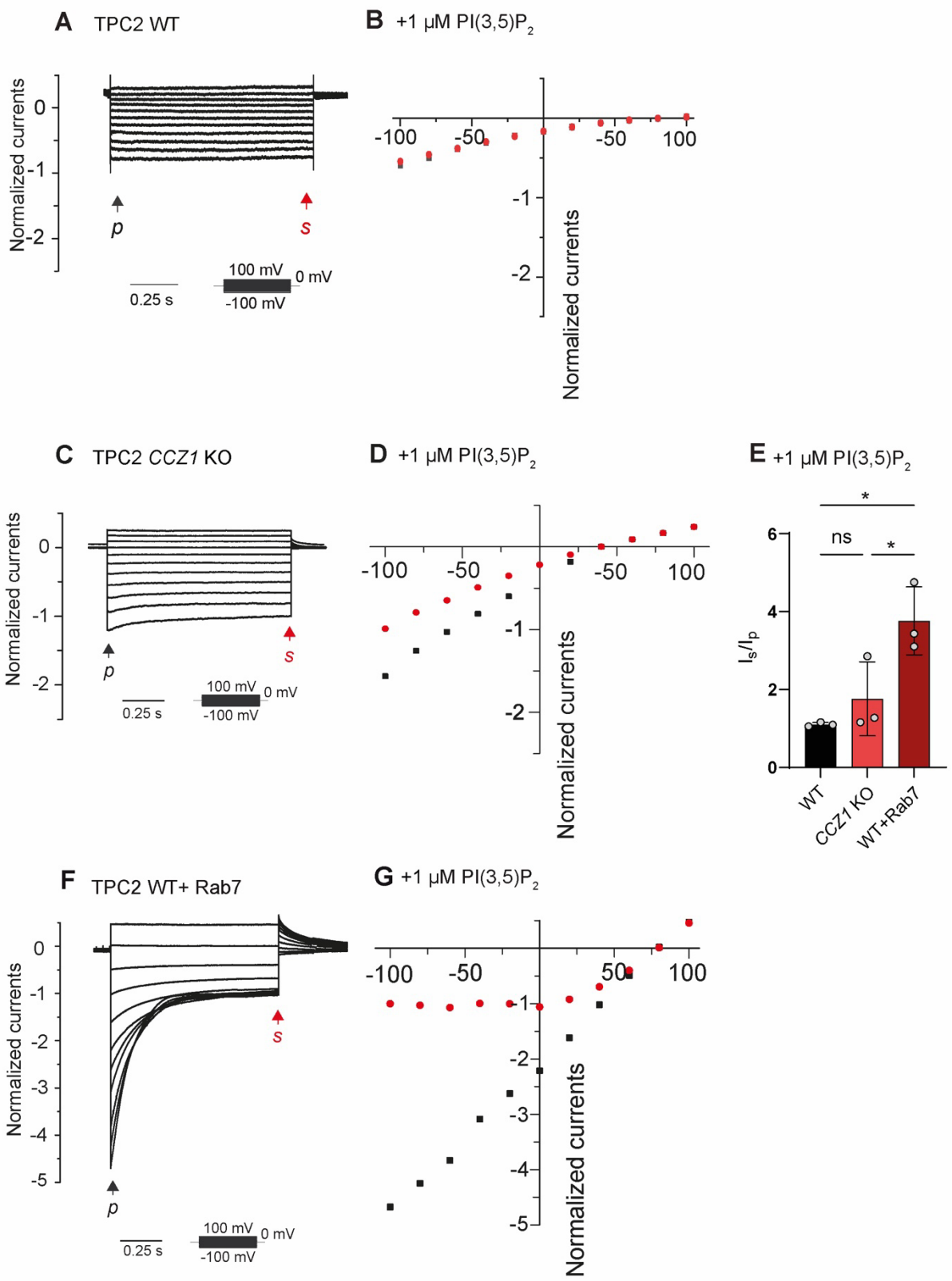
A TPC2 WT
B +1 µM PI(3,5)P2
Normalized currents
0
-1
-2
p
s
100 mV
0 mV
-100 mV
0.25 s
-100
-50
-50
100
Normalized currents
C TPC2 CCZ1 KO
D +1 µM PI(3,5)P2
E +1 µM PI(3,5)P2
Is/Ip
6
4
2
0
ns
*
*
WT
CCZ1 KO
WT+Rab7
F TPC2 WT+ Rab7
G +1 µM PI(3,5)P2
0
-1
-2
-3
-4
-5
50

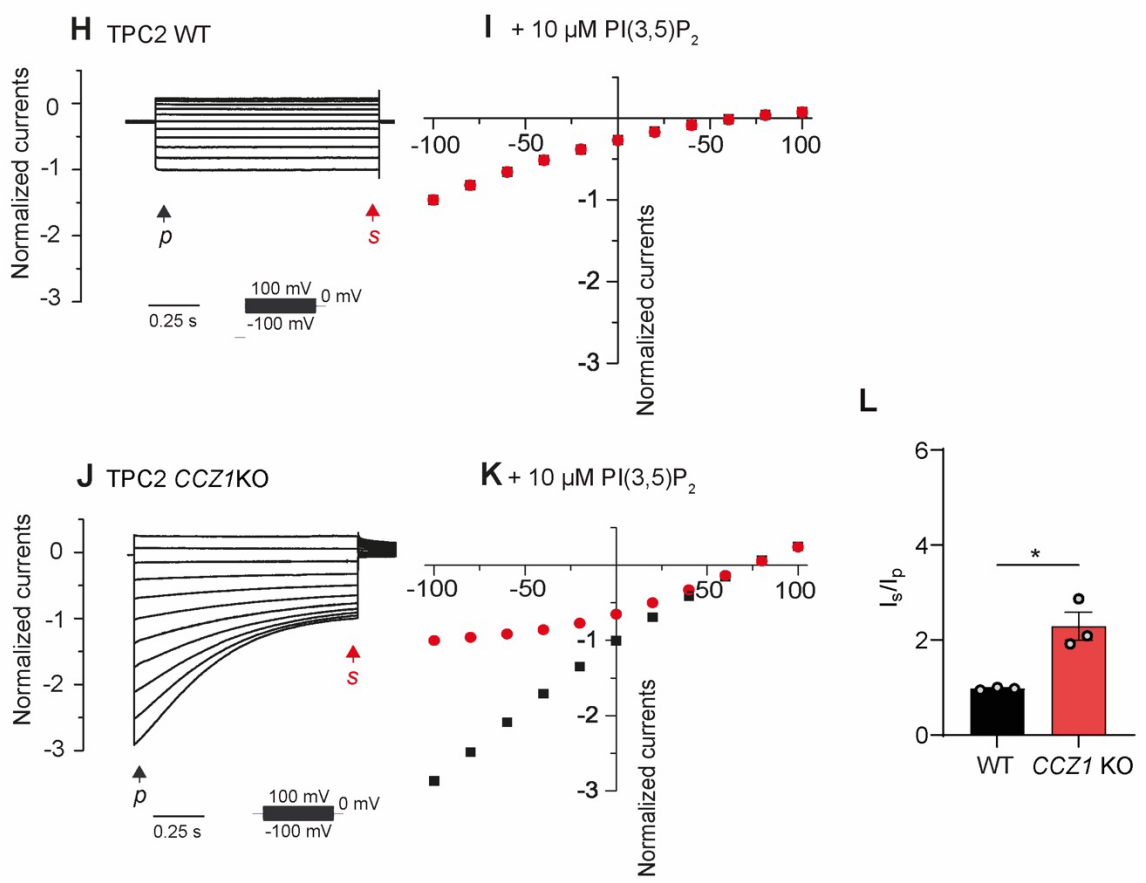


**Figure 19 Voltage-dependent response of TPC2 currents in *CCZ1* knockout cells**

(**A, C, F**) Whole-endolysosome patch-clamp recordings showing normalized TPC2 currents in HEK293 WT cells (**A**), in *CCZ1* KO cells (**C**) and in HEK 293 WT with co-expression of Rab7 (**F**) in response to1 µM PI(3,5)$P_2$, recorded using a step pulse protocol shown below the current traces. (**B, D, G**) Voltage-current (I-V) relationships for peak (*p*, red) and steady-state (*s*, black) currents in WT cells (**B**), in *CCZ1* KO cells (**D**) and in WT with co-expression of Rab7 (**G**) with treatment of 1 µM PI(3,5)$P_2$. (**H, J**) Normalized TPC2 currents in HEK 293 (**H**) and *CCZ1* KO cells (**J**) treated with 10 µM PI(3,5)$P_2$, recorded using a step pulse protocol. (**I, K**) Voltage-current (I-V) relationships for peak (*p*, red) and steady-state (*s*, black) currents in HEK 293 WT (**I**) and in *CCZ1* KO cells in response to 10 µM PI(3,5)$P_2$. (**E**) Quantification of the $I_p/I_s$ ratio in WT (black) and *CCZ1* KO (hell red) and WT with Rab7 co-expression (dark red) from **A, C** and **F**. **(L)** Quantification of the $I_p/I_s$ ratio in WT (green) and *CCZ1* KO (hell red) cells from **F** and **J** in response to 10 µM PI(3,5)$P_2$. Data are presented as mean ± s.e.m., *P < 0,05 (two-tailed t-test).

Since CCZ1 is indispensable for Rab7 to interact with TPC2, and loss of CCZ1 increases channel efficacy, FRET was performed to test whether there is a direct interaction between CCZ1 and TPC2. Despite labeling fluorophores at both termini of

CCZ1, no FRET signal was detected between the two proteins (**Figures 20A-B**). Given that CCZ1 functions in conjunction with MON1 and RMC1 to activate Rab7, these three proteins were together overexpressed to determine whether any interaction could be observed. However, all proteins exhibited a cytosolic distribution, with no evidence of specific interactions (**Figure 20C)**. The absence of TPC2–CCZ1 FRET signals may stem from tag-induced conformational changes in either CCZ1 or the MCC complex that hinder TPC2 binding. Alternatively, MCC might modulate TPC2 through an indirect pathway that bypasses direct MCC–TPC2 interaction.

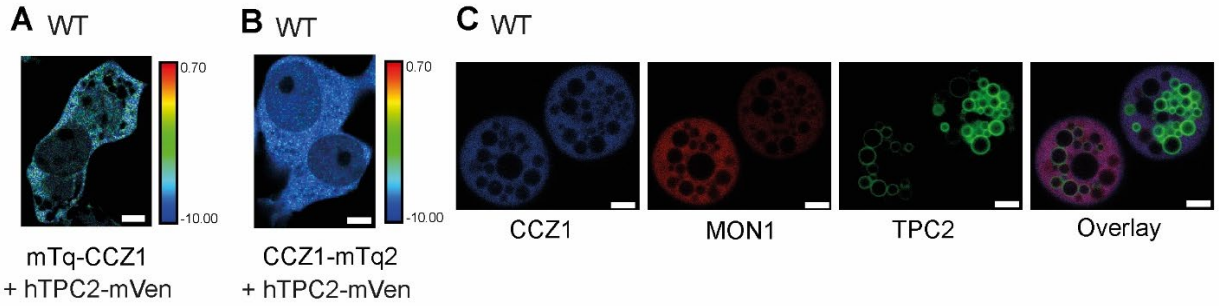


**Figure 20 No direct interaction was detected between TPC2 and MCC by FRET**

(**A, B**) FRET imaging of hTPC2-mVen with mTq-CCZ1 (**L**) or CCZ1-mTq (**M**) in HEK 293 WT cells, with the rightmost panel presenting FRET efficiency based on doner lifetime measurements. (**C**) Immunofluorescent images of overexpressed eCFP-CCZ1, mCherry-MON1, unlabeled RMC1 and hTPC2-YFP in HEK 293 WT cell after overnight incubation with apilimod, while TPC2 distributed membrane bound, MCC showed a cytosolic distribution.

## 4.9 Defective Rab5-to-Rab7 transition is not the reason for enhanced TPC2 activity in *CCZ1* KO cells

Knocking out of *MON1* not only leads to Rab7 inactivation but also results in Rab5 hyperactivation [23]. This is because the Rab5 GTPase-activating protein (GAP) TBC1D18 functions in a MON1-dependent manner, and its disruption impairs endosomal maturation. Morphologically, accumulation of active Rab5 causes an

enlarged endosomal size and a reduced number of LAMP2 positive vesicles in *MON1* KO cells. Overexpression of TBC1D18 partially rescues the aberrant endosomal morphology [23].

To determine whether the enhanced response of TPC2 to agonists observed in *CCZ1* KO cells is a consequence of impaired endosomal maturation due to defective MON1-dependent TBC1D18 activity, TBC1D18 was overexpressed in *CCZ1* KO cells. Consistent with the fact that CCZ1 and MON 1 function as a dimer and loss of either disrupts the complex, the endosomal size in *CCZ1* KO cells was normalized to almost wild-type level by overexpression of TBC1D18 (**Figure 21A**). Subsequently, lysosomal patch-clamp recordings were performed under identical conditions to assess TPC2 channel function followed by overnight incubation with apilimod, and no significant difference in TPC2 channel activity was observed with or without TBC1D18 overexpression (**Figures 21B-C, F**). These findings exclude a direct link between enhanced TPC2 function and the abnormal vesicle size resulting from Rab5 overactivation in the context of defective endosomal maturation**.** To further examine whether Rab7 deactivation or defects in its downstream effectors contribute to the increased TPC2 activity, lysosomal patch-clamp analysis was also performed in *Rab7* KO cells (**Figure 21D**). TPC2 currents in *Rab7* KO cells did not reach the levels observed in *CCZ1* KO cells, indicating that the enhanced TPC2 activity arises downstream of Rab5 inactivation and is independent of Rab7 loss-of-function (**Figure 21E**).

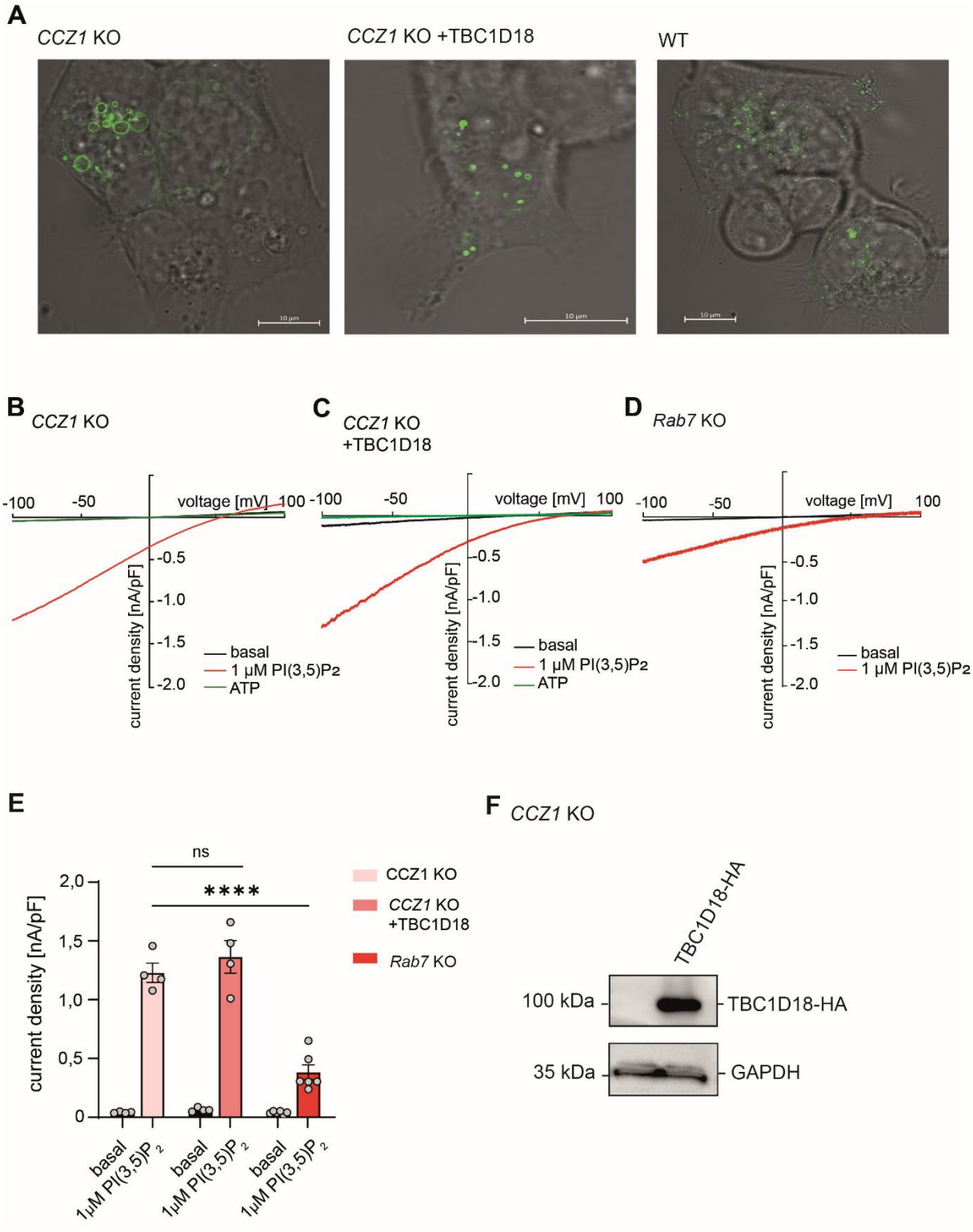


**Figure 21 Loss of function of TBC1D18 and deactivation of Rab7 are not the responsible for enhanced TPC2 activity after knocking out *CCZ1***

(**A**) Representative images showing vesicle size in *CCZ1* KO cells (left), *CCZ1* KO cells overexpressing TBC1D18-HA (middle), and WT cells (right) after overexpressing hTPC2-YFP. Scale bar is 10µm. (**B, C, D**) Whole-endolysosome patch-clamp recordings of hTPC2-YFP

currents in *CCZ1* KO cells (**B**), *CCZ1* KO cells co-expressing of TBC1D18 (**C**) and in *Rab7* KO cells (**D**), showing basal (black), ATP (green), and $PI(3,5)P_2$ (red)-stimulated current densities. (**E**) Quantification of current densities at -100 mV from endolysosomal recordings of overexpressed hTPC2-YFP in *CCZ1* KO cells with or without co-expressing of TBC1D18 and in *Rab7* KO cells. Data are presented as mean ± s.e.m. Statistical significance was determined using two-way ANOVA with Bonferroni post-hoc tests. ****p<0,0001, ns, not significant.

## 4.10 *CCZ1* KO SK-MEL5 cells show enhanced TPC2 dependent migration and proliferation

Reduced or abolished TPC2 activity impairs migration and proliferation in various cancer cell types, whereas TPC2 overactivity has been linked to enhanced migration in melanoma. Given the substantial endogenous TPC2 expression in SK-MEL5 cells compared to other cancer lines, the impact of *CCZ1* knockout on TPC2-dependent migration was investigated in both SK-MEL5 WT and SK-MEL5 *CCZ1* KO cells [62, 96]. qPCR showed a similar TPC2 transcription in SK-MEL5 WT and *CCZ1* KO cells, indicating knockout of *CCZ1* did not affect TPC2 expression (**Figure 22H**).

Due to its negative charges $PI(3,5)P_2$ cannot penetrate the plasma membrane and, hence, does not reach lysosomal organelles when applied from the extracellular space. To circumvent this problem, A1P was utilized, a well-characterized hydrophobic TPC2 agonist, that mimics activation by $PI(3,5)P_2$ to study migration and proliferation. Like $PI(3,5)P_2$ and as expected, A1P induced a significantly larger TPC2 current in *CCZ1* KO HEK 293 cells compared to that WT cells (**Figures 22A-C**).

To study cell migration, SK-MEL5 WT and *CCZ1* KO cells were seeded in a Boyden chamber and cultured for 24 hours. Migrated cells were stained and counted thereafter (**Figure 22D**). In untreated cells (no agonist in the bath), WT cells showed a stronger migration compared to *CCZ1* KO cells. This can be explained by a low endogenous TPC2 activity as TPC2 specific antagonist SG-094 failed to further reduce the migration in *CCZ1* KO cells (**Figure 22G**). As expected, and consistent with the patch

results that A1P induced a stronger TPC2 current in *CCZ1* KO cells, A1P enhanced migration rate in both cell lines, however, migration was significantly more profound in *CCZ1* KO cells compared to WT cells. Importantly, transcript levels of TPC2 were identical in WT and KO cells indicating that increased activity of TPC2 in KO cells was not caused by an increase in channel expression but rather by a stimulation of the channel itself (**Figure 22H**). Interestingly, co-expression of either WT Rab7 or Rab7[QL] did not increase cell migration in both WT and *CCZ1* KO cells. There was even a reduction of migration when Rab7 or Rab7[QL] were overexpressed. While this finding is consistent with the impaired Rab7 / TPC2 interaction in *CCZ1* KO cells, the absence of an effect in WT (and also the trend of a reduction of migration in the presence of Rab7 in *CCZ1* KO cells) might be explained by cellular processes that are controlled by Rab7 and counteract its action on TPC2.

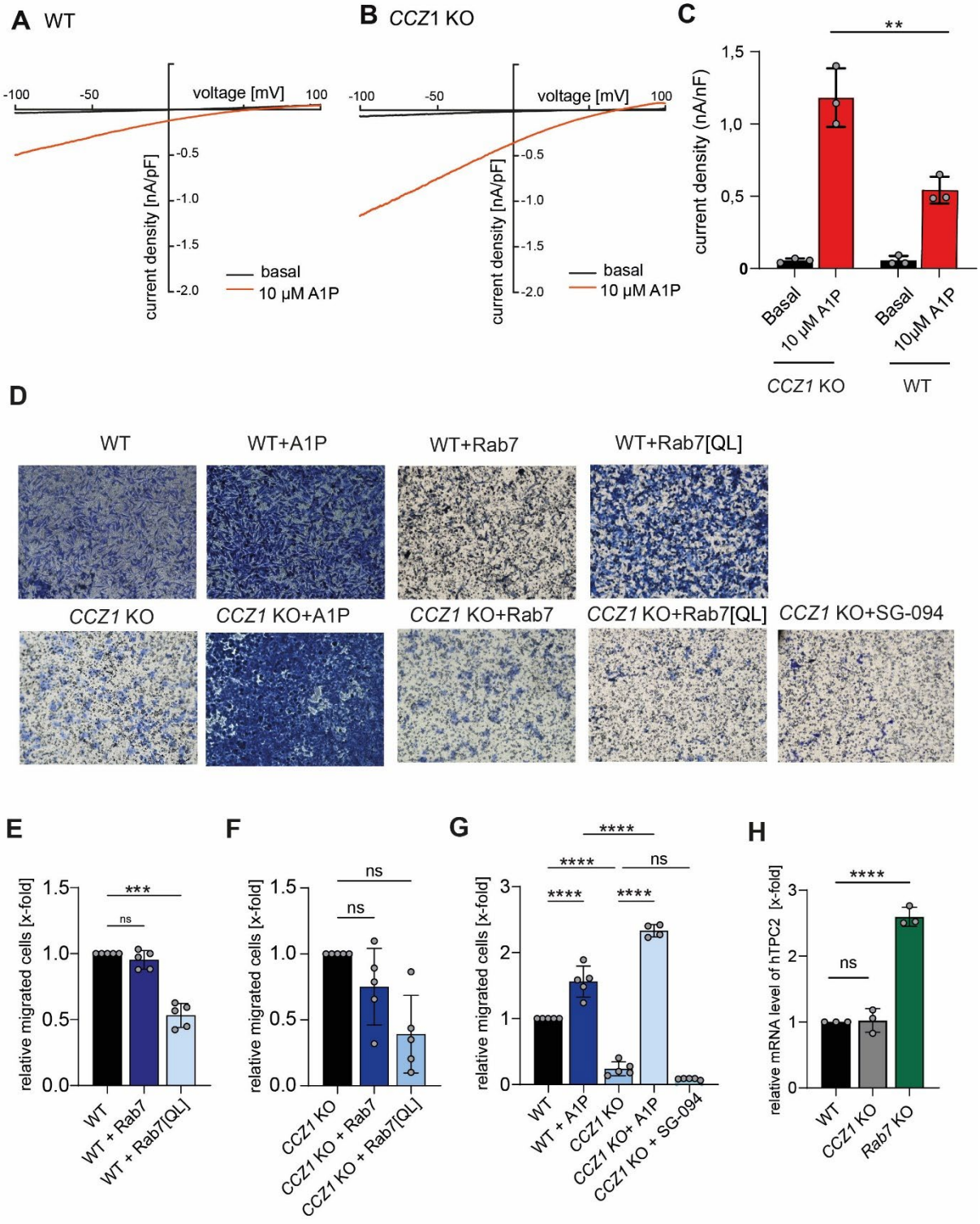


**Figure 22 *CCZ1* KO SK-MEL5 cells show enhanced TPC2 dependent migration**

(**A-C**) Whole-endolysosome patch-clamp recordings of hTPC2-YFP currents in WT (**A**) and *CCZ1* KO (**B**) HEK293 cells, showing basal (black) and A1P (red)-stimulated current. (**C**) Quantification of current densities at -100 mV from endolysosomal hTPC2-YFP recordings from **A** and **B**. Data are presented as mean ± s.e.m. Statistical significance was determined using two-way ANOVA with Bonferroni post-hoc tests. **p<0,01. (**D**) Representative images of

24h migration assay in untreated SK-EML5 WT and *CCZ1* KO cells, in both cell lines with overexpressed Rab7 WT or Rab7[QL] and with treatment of A1P or SG-094, to specifically active or inhibit TPC2. Migrated cells were afterwards stained and showed in blue. (**H**) Relative mRNA expression of TPC2 in SK-MEL5 WT, *CCZ1* KO and *Rab7* KO cells, qPCR results were normalized by WT results, statistical significance was determined using two-way ANOVA with Bonferroni post-hoc tests. (**E, F, G**) Doubling time statically analyzed in different groups. Doubling time was normalized by WT cells in each group. Data are presented as mean ± s.e.m. Statistical significance was determined using two-way ANOVA with Bonferroni post-hoc tests. ****p<0,0001, ***p<0,001.

To assess cell proliferation, SK-MEL5 WT and *CCZ1* KO cells were monitored in a xCELLigence RTCA device for 60 hours with or without treatment of A1P and SG-094. Doubling time was calculated every hour by xCELLigence RTCA, and the mean doubling time over the entire 60 h was used for analysis. In untreated groups, *CCZ1* KO cells (ginger) showed a significantly faster proliferation compared to WT cells (black) (**Figures 23A-B**). The inhibition of TPC2 with SG-094 had no significant effect on the proliferation of *CCZ1* KO cells (blue), suggesting that elevated proliferation is not driven by TPC2 activity under basal conditions (no agonist present) —a finding consistent with the migration assay results (**Figure 22G**), where TPC2 activity appeared similarly low in *CCZ1* KO cells. While A1P had no effect on the doubling time of WT cells (red), it substantially reduced the doubling time in *CCZ1* KO cells, indicating enhanced proliferation upon TPC2 activation.

Taken together, knocking out of *CCZ1* in SK-MEL5 cells i): abolishes the enhancement of Rab7 on TPC2-dependent migration and ii): promotes enhanced migration and proliferation when TPC2 is specifically activated. These findings are consistent with lysosomal patch clamp results and support a role for CCZ1 as a negative regulator of TPC2 activation.

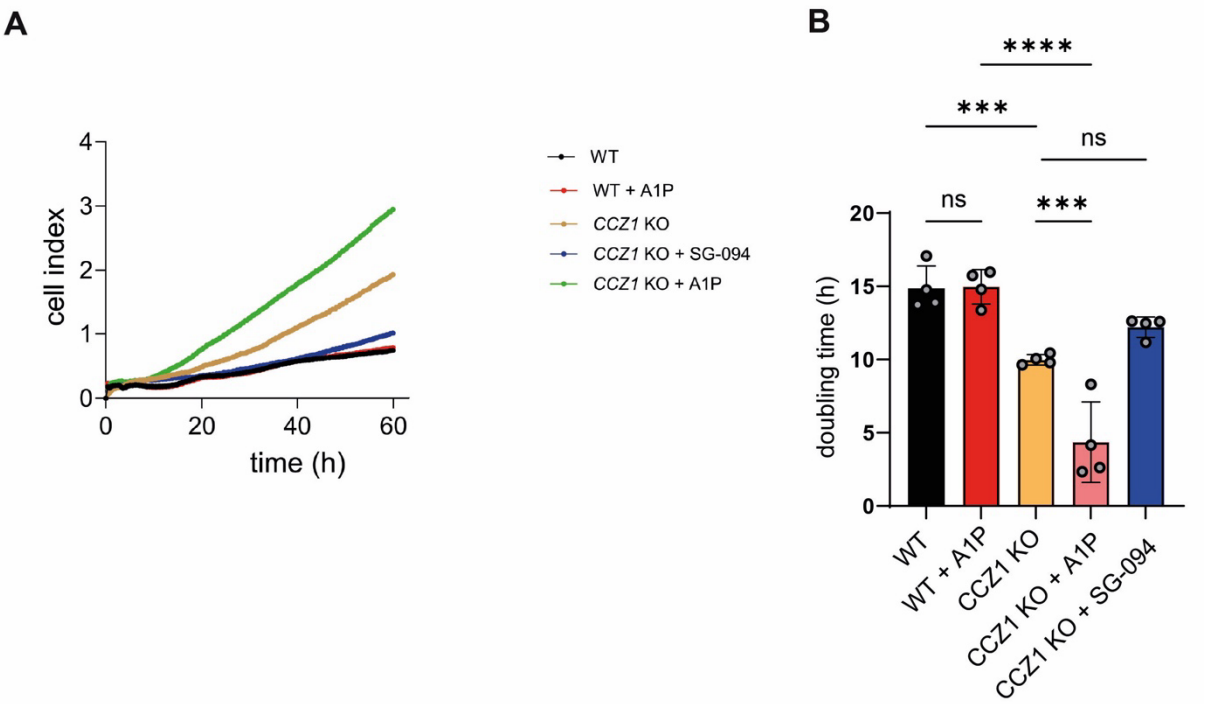


**Figure 23 *CCZ1* KO SK-MEL5 cells showed enhanced TPC2 dependent migration**

(**A**) Proliferation curves of SK-MEL5 WT basal (black), WT treated with A1P (red), *CCZ1* KO basal (ginger), *CCZ1* KO cells treated with A1P (purple) and *CCZ1* KO cells treated with SG-094 (blue). Cells were monitored over 60h. (**B**) Mean doubling time of 60h for all five groups. Data are presented as mean ± s.e.m. Statistical significance was determined using two-way ANOVA with Bonferroni post-hoc tests. ****p<0,0001, ***p<0,001, ns, not significant.

# 5 Discussion

In this thesis, CCZ1, a critical component of the MON1-CCZ1-RMC1 (MCC) complex, was identified as a novel regulator of the endolysosomal TPC2 channel. Consistent with earlier reports, it was confirmed that Rab7 enhances TPC2 activity in HEK 293 WT cells [62]. Surprisingly, this stimulatory effect was entirely abolished in *CCZ1* KO cells, indicating that the effect of Rab7 on TPC2 is not direct but rather requires the presence of CCZ1.

Interestingly, TPC2 current densities in *CCZ1* KO cells were comparable to those observed in Rab7-activated WT cells. This may suggest that under physiological (WT) conditions, TPC2 resides in a basal low-activity state, which shifts to a high-activity state when CCZ1 is absent. These findings raise the possibility that CCZ1 acts as a negative modulator of TPC2, with its inhibitory influence overcome either by Rab7 overexpression or genetic disruption of the MCC complex.

Supporting this model, FRET experiments revealed that Rab7 interacts with the TPC2 under WT conditions, whereas this interaction is completely lost in the absence of CCZ1. Notably, even a constitutively active Rab7[QL] mutant failed to bind TPC2 in *CCZ1*-deficient cells, underscoring the indispensable role of CCZ1 in mediating Rab7's regulatory effect on TPC2.

Preliminary FRET experiments did not support direct interaction between TPC2 and overexpressed CCZ1 alone or CCZ1 in the context of other components of the MCC complex. In HEK cells, the overexpressed CCZ1, MON1, and RMC1 predominantly localized to the cytosol, likely reflecting the complex, dynamic process of early-to-late endosome maturation. Alternatively, the absence of positive FRET data could, in theory, also be attributed to steric hindrance that prevents the fluorescent probes from

approaching the target protein closely. To assess such a scenario, explorative studies on the colocalization of TPC2 and MCC were performed. Specifically, as described by others [23], digitonin was used to release cytosolic proteins so that the membrane-bound fraction of MCC is enriched (**Figure 24**). Under these experimental conditions, a weak partial overlap of TPC2 and CCZ1 signals was indeed observable but, overall, the colocalization was not strong enough to explain the profound functional effects of CCZ1. Although these initial experiments are promising, further experiments with a series of fluorescent constructs of MCC components will be required to clarify whether TPC2 and MCC can interact with each other directly.

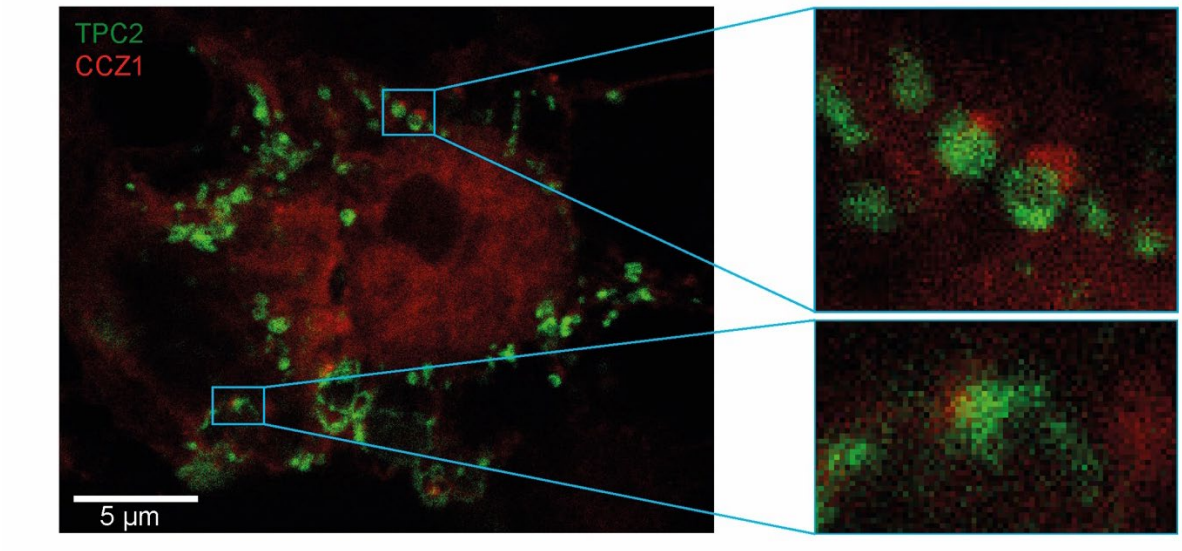


**Figure 24 Partial colocalization between TPC2 and CCZ1**

Confocal imaging showing overlap between overexpressed hTPC2-YFP (green) and the membrane-bound fraction of CCZ1 (red) after digitonin pretreatment. Vesicles with colocalized TPC2 and CCZ1 are highlighted in the zoomed-in view on the right.

Knocking out *CCZ1* disrupts the typical membrane association of the constitutively active Rab7[QL] mutant. Normally, Rab7-GDP has a high affinity for GDP dissociation inhibitor (GDI), which shields its prenyl group and keeps the GTPase in the cytosol. In contrast, the GTP-bound form—mimicked by Rab7[QL]—is not bound by GDI and, in

theory, can insert into membranes directly, bypassing the need for the GDI displacement factor (GDF) required for dissociation of GDI. Yet, Rab7[QL] fails to localize efficiently to membranes in *CCZ1* KO cells, suggesting that additional factors—potentially the MCC complex—are necessary for its insertion. MCC might promote membrane insertion either directly, possibly via RMC1, whose function remains incompletely understood, or indirectly by modulating Rab5 activity through TBC1D15. In WT cells, Rab7 activation is tightly coupled to Rab5 inactivation, minimizing their colocalization on endosomal membranes. However, in *CCZ1* KO cells, Rab5 remains hyperactive and membrane-bound, raising the alternative possibility that persistent Rab5 activity sterically or functionally hinders Rab7[QL] membrane insertion.

Furthermore, in *CCZ1* KO cells, TPC2 exhibited a “spoon-shaped” desensitization profile when activated by more than 1 µM $PI(3,5)P_2$, a significantly left-shifted EC50 for $PI(3,5)P_2$ ($EC50_{WT}$: 0,6779 µM; $EC50_{CCZ1\ KO}$: 0,2743 µM) and a stronger maximal current response. However, because EC50 is typically a property of the agonist, it should theoretically remain unchanged as long as the primary sequence of TPC2 remains unchanged. Indeed, other researchers have reported comparable EC50 values for $PI(3,5)P_2$ on wild-type TPC2, for example, Chao et al. measured an EC50 of 827 ± 183nM for $PI(3,5)P_2$ [125]. Since all currents were recorded at −100 mV, this desensitization in the I–V curve could “mask” the full current that TPC2 would otherwise conduct under hyperpolarizing conditions. Notably, this desensitization is observed not only when *CCZ1* is deleted, but also when Rab7 was co-expressed [62]. This contrasts with the typically voltage independent TPC2 current shape. Likewise, a slight spoon-like desensitization has been observed in TPC2 currents induced by 1 µM $PI(3,5)P_2$ in mTORC1 and Raptor knockdown cells [90]. The observation that ATP could inhibit

$PI(3,5)P_2$ induced currents in *CCZ1* KO cells argues against a mechanism in which the enhanced current is due to impaired mTORC1 function. In conclusion, it remains unclear whether the spoon-shaped desensitization arises from an intrinsic “auto-stop” mechanism within TPC2 (preventing excessively large currents) or if it is mediated by associated organelles involved in channel regulation.

The data imply that CCZ1 normally restrains TPC2 activity. Deleting *CCZ1* removes this brake and allows the channel to respond more strongly. One potential model to explain this observation builds on the idea that the Rab7-dependent switch relies on a not yet identified adaptor (“protein X”) capable of binding both TPC2 and Rab7-GTP:

In WT cells – Protein X is held by the MCC complex, keeping TPC2 in a low-activity state. When MCC activates Rab7, protein X is released from MCC, then captured by Rab7-GTP, and the Rab7–protein X complex docks onto TPC2, pushing the channel into a high-activity state.

In *CCZ1* KO cells – Rab7 cannot be activated into the GTP-bound state because the MCC is absent. Protein X is no longer sequestered by MCC and, through its intrinsic affinity, binds directly to TPC2, stimulating the channel into the high-activity state in a Rab7-independent manner (**Figure 25**).

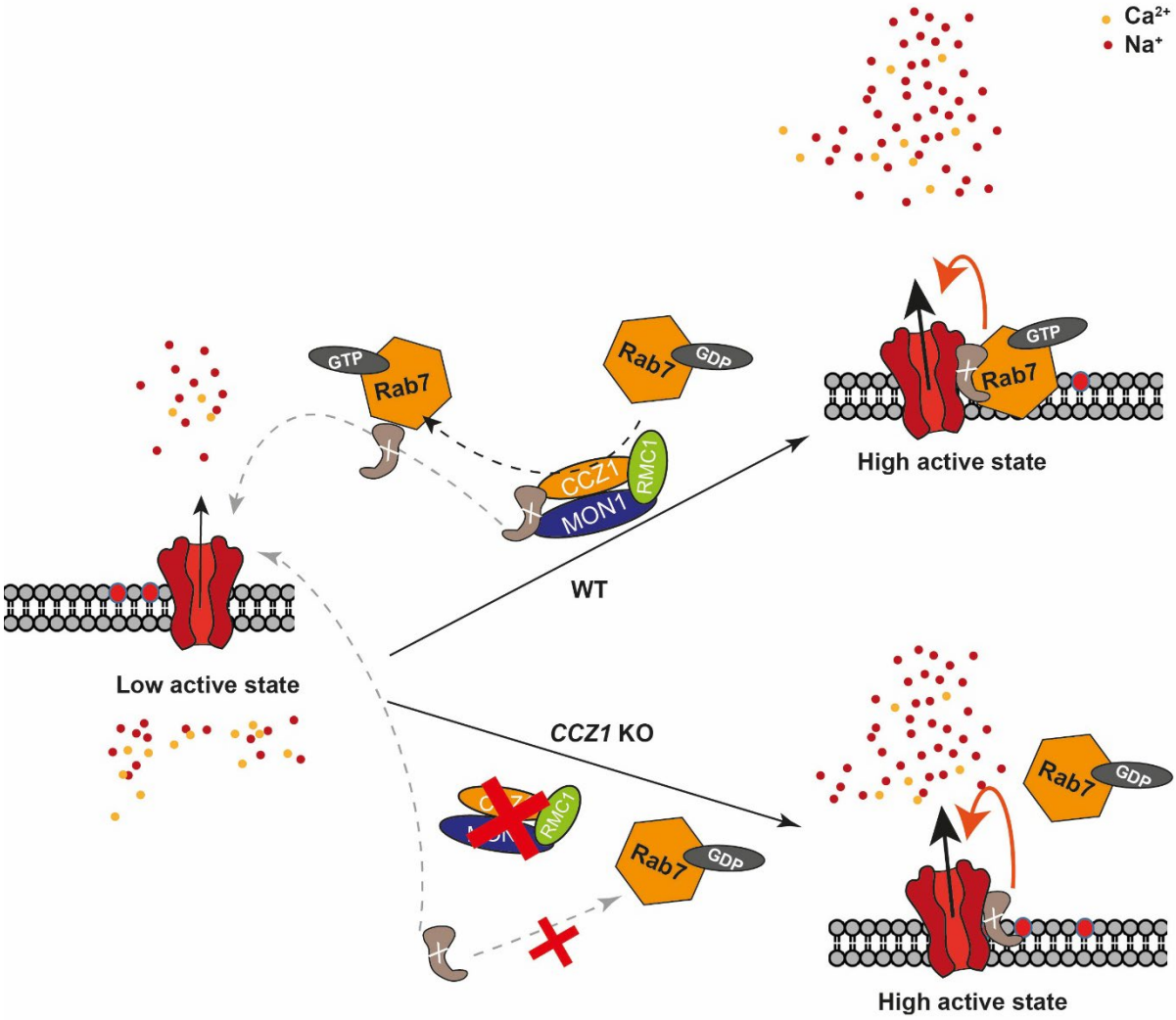


**Figure 25 Proposed model illustrating how the MCC complex indirectly regulates TPC2 channel function**

It is proposed that Rab7 modulates TPC2 through an unidentified adapter (protein X). In WT cells, protein X is sequestered by the MCC complex, leaving TPC2 in a low-activity state. When MCC converts Rab7-GDP to Rab7-GTP, protein X is released, captured by Rab7-GTP, and the resulting Rab7-GTP–protein X complex docks on TPC2, driving the channel into a high-activity state. In *CCZ1* KO cells, Rab7 remains GDP-bound because the MCC GEF is missing. Protein X is no longer sequestered and, owing to its intrinsic affinity, binds directly to TPC2, switching the channel into a high-activity state in a Rab7-independent manner.

Migration and proliferation assays in SK-MEL5 cells confirmed that *CCZ1* KO enhances TPC2 activity, consistent with patch-clamp findings. Previously, TPC2 has been shown to regulate SK-MEL5 cell migration and proliferation by promoting GSK-3β degradation, which in turn stabilizes β-catenin and MITF [62]. Enhancing TPC2

activity—either through agonist treatment or by overexpressing activators like Rab7—leads to increased GSK-3β degradation, resulting in β-catenin and MITF stabilization and ultimately promoting cell migration and proliferation [62]. In *CCZ1* KO cells, TPC2 shifts from a low- to a high-activity state. As a result, upon agonist stimulation, *CCZ1* KO SK-MEL5 cells show stronger TPC2 activation and, hence, greater lysosomal degradation capacity compared to WT cells. The increased activity is accompanied by enhanced GSK-3β degradation, elevated MITF levels, and increased migration and proliferation. Interestingly, the role of CCZ1 appears to be context dependent. In contrast to SK-MEL5 cells, CCZ1 downregulation in cutaneous-squamous cell carcinoma has been correlated with reduced tumor proliferation, suggesting that the impact of CCZ1 on migration and growth may vary across cancer types [26].

Notably, basal migration was significantly slower in *CCZ1* KO cells. Given the already low TPC2 activity in these cells and the lack of further reduction in migration rate following SG-094 treatment, it is likely that the impaired migration results from other factors influenced by the loss of *CCZ1*. The expression levels of MMP2 and MMP17 have been reported to be positively regulated by CCZ1 expression level, and their downregulation following *CCZ1* knockout likely contributes to the slower migration observed compared to WT cells [26]. In a 60-hour proliferation assay, however, *CCZ1* KO cells proliferated surprisingly significantly faster than WT cells under basal conditions. Treatment with SG-094 did not substantially reduce their proliferation, suggesting that the enhanced basal proliferation in *CCZ1* KO cells may therefore also be driven by a distinct signaling pathway affected by CCZ1 loss. The exact mechanism underlying this decreased TPC2 activity in untreated *CCZ1* KO cells remains unclear. Considering that *MON1* KO cells possess a highly acidic pH, active lysosomal proteases [23] and TPC2 activity is not significantly affected by pH value changes from

4,6 to 7,4 [77], another possible explanation could be the disrupted synthesis of its endogenous agonist, $PI(3,5)P_2$, resulting from *CCZ1* knockout.

PIKfyve, the key kinase responsible for converting PI3P to $PI(3,5)P_2$, has been implicated in regulating cancer cell migration [126]. Its dysregulation leads to abnormal EEA1-positive endosomes—a phenotype that can be rescued by overexpression of a dominant-negative Rab5 [127], resembling the endosomal defects observed in *CCZ1* KO cells. VPS34, the lipid kinase that generates PI3P, interacts with Rab5 on early endosomes, and its activity is positively correlated with the GTP-bound form of Rab5 [128]. In *CCZ1* KO cells, Rab5 is hyperactivated, likely resulting in increased PI3P production on early endosomes. This, in turn, enhances the recruitment and activity of PIKfyve, promoting the synthesis of $PI(3,5)P_2$ [129].

However, due to defective maturation of early endosomes into late endosomes in *CCZ1* KO cells, these PI(3,5)P2-enriched compartments fail to efficiently fuse with lysosomes, where TPC2 is localized. As a result, $PI(3,5)P_2$ is delivered less effectively to newly formed lysosomes, leading to reduced basal TPC2 activity.

In contrast to the migration assay—where TPC2 activation enhanced cell migration in both WT and *CCZ1* KO cells—A1P treatment did not accelerate proliferation in WT SK-MEL5 cells, suggesting that TPC2 plays a limited role in regulating proliferation in this cell line. Nevertheless, A1P did promote proliferation in non-inhibited *CCZ1* KO cells, indicating a context-dependent role for TPC2 in supporting cell growth under conditions of impaired endosomal maturation.

Together, these findings highlight a mechanistic link between endosomal maturation, phosphoinositide signaling, and TPC2-dependent regulation of cellular behaviors, underscoring the critical role of CCZ1 in maintaining endolysosomal function and cellular homeostasis.

# 6 Summary

In this study, lysosomal patch-clamp, FRET, and CRISPR-Cas9 experiments identified CCZ1—a core component of the MON1–CCZ1–RMC1 (MCC) complex—as a key regulator of TPC2 activity. Loss of CCZ1 enhances TPC2 activation by agonists and abolishes its regulation by Rab7. Although the precise mechanism remains unclear, a model of indirect regulation is proposed: in wild-type cells, an unidentified adaptor protein ("protein X") is sequestered by the MCC complex, keeping TPC2 in a low-activity state. Once MCC activates Rab7, protein X is released, combines with Rab7, docks onto TPC2, and drives the channel into a high-activity state. In *CCZ1* KO cells, Rab7 activation falters in the absence of MCC, leaving protein X free to bind TPC2 directly and activate the channel independently of Rab7.

Functional assays in the SK-MEL5 melanoma cell line—rich in endogenous TPC2 and Rab7—support this mechanism. *CCZ1* KO markedly increases TPC2-driven migration and proliferation after agonist stimulation compared with WT cells.

Overall, these findings reveal an unrecognized layer of TPC2 regulation within the Rab7 signaling axis and establish CCZ1 as a pivotal upstream modulator of lysosomal excitability, with implications for diseases marked by dysregulated TPC2 activity.

# 7 References


1. Kucharczyk, R., et al., *The novel protein Ccz1p required for vacuolar assembly in Saccharomyces cerevisiae functions in the same transport pathway as Ypt7p.* Journal of Cell Science, 2000. **113**(23): p. 4301-4311.
2. Kucharczyk, R.z.a., et al., *The Ccz1 protein interacts with Ypt7 GTPase during fusion of multiple transport intermediates with the vacuole in S. cerevisiae.* Journal of Cell Science, 2001. **114**(17): p. 3137-3145.
3. Wang, C.-W., et al., *The Ccz1-Mon1 Protein Complex Is Required for the Late Step of Multiple Vacuole Delivery Pathways *.* Journal of Biological Chemistry, 2002. **277**(49): p. 47917-47927.
4. Cui, Y., et al., *Activation of the Rab7 GTPase by the MON1-CCZ1 Complex Is Essential for PVC-to-Vacuole Trafficking and Plant Growth in Arabidopsis* The Plant Cell, 2014. **26**(5): p. 2080-2097.
5. Nordmann, M., et al., *The Mon1-Ccz1 Complex Is the GEF of the Late Endosomal Rab7 Homolog Ypt7.* Current Biology, 2010. **20**(18): p. 1654-1659.
6. Hoffman-Sommer, M., et al., *Multiple functions of the vacuolar sorting protein Ccz1p in Saccharomyces cerevisiae.* Biochemical and Biophysical Research Communications, 2005. **329**(1): p. 197-204.
7. Yong, X., et al., *Cryo-EM structure of the Mon1–Ccz1–RMC1 complex reveals molecular basis of metazoan RAB7A activation.* Proceedings of the National Academy of Sciences, 2023. **120**(22): p. e2301725120.
8. Filippini, F., et al., *Longins: a new evolutionary conserved VAMP family sharing a novel SNARE domain.* Trends in Biochemical Sciences, 2001. **26**(7): p. 407-409.

9. Rossi, V., et al., *Longins and their longin domains: regulated SNAREs and multifunctional SNARE regulators.* Trends in Biochemical Sciences, 2004. **29**(12): p. 682-688.

10. Klink, B.U., et al., *Structure of the Mon1-Ccz1 complex reveals molecular basis of membrane binding for Rab7 activation.* Proceedings of the National Academy of Sciences, 2022. **119**(6): p. e2121494119.

11. Dehnen, L., et al., *A trimeric metazoan Rab7 GEF complex is crucial for endocytosis and scavenger function.* Journal of Cell Science, 2020. **133**(13).

12. Tang, Y., et al., *Mechanistic insights into the GEF activity of the human MON1A/CCZ1/C18orf8 complex.* Protein & cell, 2025: p. pwaf018.

13. Borchers, A.-C., et al., *Regulatory sites in the Mon1–Ccz1 complex control Rab5 to Rab7 transition and endosome maturation.* Proceedings of the National Academy of Sciences, 2023. **120**(30): p. e2303750120.

14. Gao, J., et al., *Molecular mechanism to target the endosomal Mon1-Ccz1 GEF complex to the pre-autophagosomal structure.* Elife, 2018. **7**: p. e31145.

15. Cai, C.-Z., et al., *NRBF2 is a RAB7 effector required for autophagosome maturation and mediates the association of APP-CTFs with active form of RAB7 for degradation.* Autophagy, 2021. **17**(5): p. 1112-1130.

16. Matsumoto, N., et al., *The lysosomal V-ATPase a3 subunit is involved in localization of Mon1-Ccz1, the GEF for Rab7, to secretory lysosomes in osteoclasts.* Scientific Reports, 2022. **12**(1): p. 8455.

17. Matsumoto, N., et al., *Essential Role of the a3 Isoform of V-ATPase in Secretory Lysosome Trafficking via Rab7 Recruitment.* Scientific Reports, 2018. **8**(1): p. 6701.

18. Yan, B.-R., et al., *C5orf51 is a component of the MON1-CCZ1 complex and controls RAB7A localization and stability during mitophagy.* Autophagy, 2022. **18**(4): p. 829-840.

19. Schmökel, V., et al., *Genetics of Lipid-Storage Management in Caenorhabditis elegans Embryos.* Genetics, 2016. **202**(3): p. 1071-1083.

20. Nieto, C., et al., *ccz-1 mediates the digestion of apoptotic corpses in C. elegans.* Journal of Cell Science, 2010. **123**(12): p. 2001-2007.

21. Hoffman-Sommer, M., et al., *The CHiPS Domain – Ancient Traces for the Hermansky–Pudlak Syndrome.* Traffic, 2005. **6**(7): p. 534-538.

22. Dong, Y., et al., *The Ccz1 mediates the autophagic clearance of damaged mitochondria in response to oxidative stress in Candida albicans.* The International Journal of Biochemistry & Cell Biology, 2015. **69**: p. 41-51.

23. Hiragi, S., et al., *TBC1D18 is a Rab5-GAP that coordinates endosome maturation together with Mon1.* Journal of Cell Biology, 2022. **221**(12).

24. van den Boomen, D.J.H., et al., *A trimeric Rab7 GEF controls NPC1-dependent lysosomal cholesterol export.* Nature Communications, 2020. **11**(1): p. 5559.

25. Monteil, V., et al., *Identification of CCZ1 as an essential lysosomal trafficking regulator in Marburg and Ebola virus infections.* Nature Communications, 2023. **14**(1): p. 6785.

26. Yu, J., et al., *CCZ1 Accelerates the Progression of Cervical Squamous Cell Carcinoma by Promoting MMP2/MMP17 Expression.* Biomedicines, 2024. **12**(7): p. 1468.

27. Cai, C.-Z., et al., *Enhancing autophagy maturation with CCZ1-MON1A complex alleviates neuropathology and memory defects in Alzheimer disease models.* Theranostics, 2022. **12**(4): p. 1738-1755.

28. Bright, L.J. and M. Lynch, *The Rab7 subfamily across Paramecium aurelia species; evidence of high conservation in sequence and function.* Small GTPases, 2020. **11**(6): p. 421-429.

29. Klöpper, T.H., et al., *Untangling the evolution of Rab G proteins: implications of a comprehensive genomic analysis.* BMC Biology, 2012. **10**(1): p. 71.

30. Wang, Q., et al., *Rab7 controls innate immunity by regulating phagocytosis and antimicrobial peptide expression in Chinese mitten crab.* Fish & Shellfish Immunology, 2019. **95**: p. 259-267.

31. Yang, M., et al., *Rab7b, a novel lysosome-associated small GTPase, is involved in monocytic differentiation of human acute promyelocytic leukemia cells.* Biochemical and Biophysical Research Communications, 2004. **318**(3): p. 792-799.

32. Rink, J., et al., *Rab conversion as a mechanism of progression from early to late endosomes.* Cell, 2005. **122**(5): p. 735-749.

33. Cantalupo, G., et al., *Rab-interacting lysosomal protein (RILP): the Rab7 effector required for transport to lysosomes.* The EMBO journal, 2001. **20**(4): p. 683-693.

34. Bucci, C., et al., *Rab7: a key to lysosome biogenesis.* Molecular biology of the cell, 2000. **11**(2): p. 467-480.

35. Yamano, K., et al., *Mitochondrial Rab GAPs govern autophagosome biogenesis during mitophagy.* Elife, 2014. **3**: p. e01612.

36. Hyttinen, J.M., et al., *Maturation of autophagosomes and endosomes: a key role for Rab7.* Biochimica et Biophysica Acta (BBA)-Molecular Cell Research, 2013. **1833**(3): p. 503-510.

37. Gutierrez, M.G., et al., *Rab7 is required for the normal progression of the autophagic pathway in mammalian cells.* Journal of cell science, 2004. **117**(13): p. 2687-2697.

38. Li, Z., et al., *RAB7A GTPase Is Involved in Mitophagosome Formation and Autophagosome–Lysosome Fusion in N2a Cells Treated with the Prion Protein Fragment 106–126.* Molecular Neurobiology, 2023. **60**(3): p. 1391-1407.

39. Jin, X., et al., *RAB7 activity is required for the regulation of mitophagy in oocyte meiosis and oocyte quality control during ovarian aging.* Autophagy, 2022. **18**(3): p. 643-660.

40. Progida, C., et al., *Rab7b controls trafficking from endosomes to the TGN.* Journal of cell science, 2010. **123**(9): p. 1480-1491.

41. Progida, C., et al., *Dynamics of Rab7b-dependent transport of sorting receptors.* Traffic, 2012. **13**(9): p. 1273-1285.

42. Pylypenko, O., et al., *Structure of Rab escort protein-1 in complex with Rab geranylgeranyltransferase.* Molecular cell, 2003. **11**(2): p. 483-494.

43. Wu, Y.-W., et al., *Structure of the Disordered C Terminus of Rab7 GTPase Induced by Binding to the Rab Geranylgeranyl Transferase Catalytic Complex Reveals the Mechanism of Rab Prenylation *.* Journal of Biological Chemistry, 2009. **284**(19): p. 13185-13192.

44. Ghomashchi, F., et al., *Binding of prenylated and polybasic peptides to membranes: affinities and intervesicle exchange.* Biochemistry, 1995. **34**(37): p. 11910-11918.

45. Dirac-Svejstrup, A.B., T. Sumizawa, and S.R. Pfeffer, *Identification of a GDI displacement factor that releases endosomal Rab GTPases from Rab–GDI.* The EMBO journal, 1997.

46. Sivars, U., D. Aivazian, and S.R. Pfeffer, *Yip3 catalyses the dissociation of endosomal Rab–GDI complexes.* Nature, 2003. **425**(6960): p. 856-859.

47. Kiontke, S., et al., *Architecture and mechanism of the late endosomal Rab7-like Ypt7 guanine nucleotide exchange factor complex Mon1–Ccz1.* Nature communications, 2017. **8**(1): p. 14034.

48. Itzen, A. and R.S. Goody. *GTPases involved in vesicular trafficking: structures and mechanisms*. in *Seminars in cell & developmental biology*. 2011. Elsevier.

49. Stroupe, C. and A.T. Brunger, *Crystal structures of a Rab protein in its inactive and active conformations.* Journal of molecular biology, 2000. **304**(4): p. 585-598.

50. Fukuda, M., *TBC proteins: GAPs for mammalian small GTPase Rab?* Bioscience reports, 2011. **31**(3): p. 159-168.

51. Guerra, F. and C. Bucci, *Multiple roles of the small GTPase Rab7.* Cells, 2016. **5**(3): p. 34.

52. Lazar, T., D. Scheglmann, and D. Gallwitz, *A novel phospholipid-binding protein from the yeast Saccharomyces cerevisiae with dual binding specificities for the transport GTPase Ypt7p and the Sec1-related Vps33p.* European journal of cell biology, 2002. **81**(12): p. 635-646.

53. Sun, Q., et al., *Rubicon controls endosome maturation as a Rab7 effector.* Proceedings of the National Academy of Sciences, 2010. **107**(45): p. 19338-19343.

54. Seals, D.F., et al., *A Ypt/Rab effector complex containing the Sec1 homolog Vps33p is required for homotypic vacuole fusion.* Proceedings of the national academy of sciences, 2000. **97**(17): p. 9402-9407.

55. Wegener, C.S., et al., *Ultrastructural characterization of giant endosomes induced by GTPase-deficient Rab5.* Histochemistry and cell biology, 2010. **133**: p. 41-55.

56. Jordens, I., et al., *The Rab7 effector protein RILP controls lysosomal transport by inducing the recruitment of dynein-dynactin motors.* Current Biology, 2001. **11**(21): p. 1680-1685.

57. Pankiv, S., et al., *FYCO1 is a Rab7 effector that binds to LC3 and PI3P to mediate microtubule plus end–directed vesicle transport.* Journal of Cell Biology, 2010. **188**(2): p. 253-269.

58. Sun, Y., et al., *Possible role of direct Rac1-Rab7 interaction in ruffled border formation of osteoclasts.* Journal of Biological Chemistry, 2005. **280**(37): p. 32356-32361.

59. Margiotta, A., et al., *Rab7a regulates cell migration through Rac1 and vimentin.* Biochimica et Biophysica Acta (BBA) - Molecular Cell Research, 2017. **1864**(2): p. 367-381.

60. Lawson, C.D. and K. Burridge, *The on-off relationship of Rho and Rac during integrin-mediated adhesion and cell migration.* Small GTPases, 2014. **5**(1): p. e27958.

61. Chung, B.-M., J.D. Rotty, and P.A. Coulombe, *Networking galore: intermediate filaments and cell migration.* Current opinion in cell biology, 2013. **25**(5): p. 600-612.

62. Abrahamian, C., et al., *Rab7a is an enhancer of TPC2 activity regulating melanoma progression through modulation of the GSK3β/β-Catenin/MITF-axis.* Nature Communications, 2024. **15**(1): p. 10008.

63. Xie, J., et al., *Knockdown of Rab7a suppresses the proliferation, migration, and xenograft tumor growth of breast cancer cells.* Bioscience reports, 2019. **39**(2): p. BSR20180480.

64. Croizet-Berger, K., et al., *The endocytic catalysts, Rab5a and Rab7, are tandem regulators of thyroid hormone production.* Proceedings of the National Academy of Sciences, 2002. **99**(12): p. 8277-8282.

65. Davidson, B., et al., *Gene expression signatures differentiate ovarian/peritoneal serous carcinoma from diffuse malignant peritoneal mesothelioma.* Clinical cancer research, 2006. **12**(20): p. 5944-5950.

66. Liu, H., et al., *Rab7 Is Associated with Poor Prognosis of Gastric Cancer and Promotes Proliferation, Invasion, and Migration of Gastric Cancer Cells.* Med Sci Monit, 2020. **26**: p. e922217.

67. Williams, K.C. and M.G. Coppolino, *Phosphorylation of Membrane Type 1-Matrix Metalloproteinase (MT1-MMP) and Its Vesicle-associated Membrane Protein 7 (VAMP7)-dependent Trafficking Facilitate Cell Invasion and Migration *.* Journal of Biological Chemistry, 2011. **286**(50): p. 43405-43416.

68. Lin-Moshier, Y., et al., *The Two-pore channel (TPC) interactome unmasks isoform-specific roles for TPCs in endolysosomal morphology and cell*

*pigmentation.* Proceedings of the National Academy of Sciences, 2014. **111**(36): p. 13087-13092.

69. Zhu, M.X., et al., *Calcium signaling via two-pore channels: local or global, that is the question.* American Journal of Physiology-Cell Physiology, 2010. **298**(3): p. C430-C441.
70. Castonguay, J., et al., *The two-pore channel TPC1 is required for efficient protein processing through early and recycling endosomes.* Scientific reports, 2017. **7**(1): p. 10038.
71. Calcraft, P.J., et al., *NAADP mobilizes calcium from acidic organelles through two-pore channels.* Nature, 2009. **459**(7246): p. 596-600.
72. Zong, X., et al., *The two-pore channel TPCN2 mediates NAADP-dependent Ca2+-release from lysosomal stores.* Pflügers Archiv - European Journal of Physiology, 2009. **458**(5): p. 891-899.
73. Brailoiu, E., et al., *Essential requirement for two-pore channel 1 in NAADP-mediated calcium signaling.* Journal of Cell Biology, 2009. **186**(2): p. 201-209.
74. Cang, C., B. Bekele, and D. Ren, *The voltage-gated sodium channel TPC1 confers endolysosomal excitability.* Nature chemical biology, 2014. **10**(6): p. 463-469.
75. Rybalchenko, V., et al., *Membrane Potential Regulates Nicotinic Acid Adenine Dinucleotide Phosphate (NAADP) Dependence of the pH- and Ca<sup>2+</sup>-sensitive Organellar Two-pore Channel TPC1 *.* Journal of Biological Chemistry, 2012. **287**(24): p. 20407-20416.
76. Pitt, S.J., et al., *TPC2 Is a Novel NAADP-sensitive Ca<sup>2+</sup> Release Channel, Operating as a Dual Sensor of Luminal pH and*

*Ca<sup>2+</sup>*<sup></sup>.* Journal of Biological Chemistry, 2010. **285**(45): p. 35039-35046.

77. Wang, X., et al., *TPC proteins are phosphoinositide-activated sodium-selective ion channels in endosomes and lysosomes.* Cell, 2012. **151**(2): p. 372-383.

78. Jha, A., et al., *Convergent regulation of the lysosomal two‐pore channel‐2 by Mg<sup>2+</sup>, NAADP, PI(3,5)P<sub>2</sub> and multiple protein kinases.* The EMBO Journal, 2014. **33**(5): p. 501-511.

79. She, J., et al., *Structural mechanisms of phospholipid activation of the human TPC2 channel.* Elife, 2019. **8**: p. e45222.

80. Peiter, E., et al., *The vacuolar Ca2+-activated channel TPC1 regulates germination and stomatal movement.* Nature, 2005. **434**(7031): p. 404-408.

81. Dadacz-Narloch, B., et al., *A novel calcium binding site in the slow vacuolar cation channel TPC1 senses luminal calcium levels.* The Plant Cell, 2011. **23**(7): p. 2696-2707.

82. Guo, J., et al., *Structure of the voltage-gated two-pore channel TPC1 from Arabidopsis thaliana.* Nature, 2016. **531**(7593): p. 196-201.

83. Bonaventure, G., et al., *A gain‐of‐function allele of TPC1 activates oxylipin biogenesis after leaf wounding in Arabidopsis.* The Plant Journal, 2007. **49**(5): p. 889-898.

84. Jaślan, D., et al., *Voltage-dependent gating of SV channel TPC1 confers vacuole excitability.* Nature Communications, 2019. **10**(1): p. 2659.

85. Rahman, T., et al., *Two-pore channels provide insight into the evolution of voltage-gated Ca2+ and Na+ channels.* Sci Signal, 2014. **7**(352): p. ra109.

86. She, J., et al., *Structural insights into the voltage and phospholipid activation of the mammalian TPC1 channel.* Nature, 2018. **556**(7699): p. 130-134.

87. Zhang, X., et al., *Agonist-specific voltage-dependent gating of lysosomal two-pore Na+ channels.* eLife, 2019. **8**: p. e51423.

88. Zaki, A.-M., et al., *Plasticity of the selectivity filter is essential for permeation in lysosomal TPC2 channels.* Proceedings of the National Academy of Sciences, 2024. **121**(32): p. e2320153121.

89. Pitt, S.J., et al., *Reconstituted Human TPC1 Is a Proton-Permeable Ion Channel and Is Activated by NAADP or Ca<sup>2+</sup>.* Science Signaling, 2014. **7**(326): p. ra46-ra46.

90. Cang, C., et al., *mTOR regulates lysosomal ATP-sensitive two-pore Na+ channels to adapt to metabolic state.* Cell, 2013. **152**(4): p. 778-790.

91. Gerndt, S., et al., *Agonist-mediated switching of ion selectivity in TPC2 differentially promotes lysosomal function.* Elife, 2020. **9**: p. e54712.

92. Gunaratne, G.S., et al., *Essential requirement for JPT2 in NAADP-evoked Ca2+ signaling.* Science signaling, 2021. **14**(675): p. eabd5605.

93. Gunaratne, G.S., et al., *Convergent activation of two-pore channels mediated by the NAADP-binding proteins JPT2 and LSM12.* Science signaling, 2023. **16**(799): p. eadg0485.

94. Zhang, J., et al., *Lsm12 is an NAADP receptor and a two-pore channel regulatory protein required for calcium mobilization from acidic organelles.* Nature communications, 2021. **12**(1): p. 4739.

95. Saito, R., et al., *Convergent activation of Ca<sup>2+</sup> permeability in two-pore channel 2 through distinct molecular routes.* Science Signaling, 2023. **16**(799): p. eadg0661.

96. Nguyen, O.N.P., et al., *Two-pore channel function is crucial for the migration of invasive cancer cells.* Cancer research, 2017. **77**(6): p. 1427-1438.

97. Sakurai, Y., et al., *Two-pore channels control Ebola virus host cell entry and are drug targets for disease treatment.* Science, 2015. **347**(6225): p. 995-998.

98. Heister, P.M. and R.N. Poston, *Pharmacological hypothesis: TPC2 antagonist tetrandrine as a potential therapeutic agent for COVID-19.* Pharmacology research & perspectives, 2020. **8**(5): p. e00653.

99. Li, Y., et al., *TPC2 promotes choroidal angiogenesis and inflammation in a mouse model of neovascular age-related macular degeneration.* Life Science Alliance, 2021. **4**(8).

100. Jin, H., et al., *Pulmonary Toxicity and Metabolic Activation of Tetrandrine in CD-1 Mice.* Chemical Research in Toxicology, 2011. **24**(12): p. 2142-2152.

101. Müller, M., et al., *Gene editing and synthetically accessible inhibitors reveal role for TPC2 in HCC cell proliferation and tumor growth.* Cell chemical biology, 2021. **28**(8): p. 1119-1131. e27.

102. Chi, G., et al., *Structural basis for inhibition of the lysosomal two-pore channel TPC2 by a small molecule antagonist.* Structure, 2024. **32**(8): p. 1137-1149.e4.

103. Favia, A., et al., *VEGF-induced neoangiogenesis is mediated by NAADP and two-pore channel-2–dependent Ca<sup>2+</sup> signaling.* Proceedings of the National Academy of Sciences, 2014. **111**(44): p. E4706-E4715.

104. Naylor, E., et al., *Identification of a chemical probe for NAADP by virtual screening.* Nat Chem Biol, 2009. **5**(4): p. 220-6.

105. Tsvilovskyy, V., et al., *OCaR1 endows exocytic vesicles with autoregulatory competence by preventing uncontrolled Ca 2+ release, exocytosis, and pancreatic tissue damage.* The Journal of Clinical Investigation, 2024. **134**(7).

106. Geisslinger, F., et al., *Targeting TPC2 sensitizes acute lymphoblastic leukemia cells to chemotherapeutics by impairing lysosomal function.* Cell Death & Disease, 2022. **13**(8): p. 668.

107. Lin, P.-H., et al., *Lysosomal Two-pore Channel Subtype 2 (TPC2) Regulates Skeletal Muscle Autophagic Signaling *.* Journal of Biological Chemistry, 2015. **290**(6): p. 3377-3389.

108. Ambrosio, A.L., et al., *TPC2 controls pigmentation by regulating melanosome pH and size.* Proceedings of the National Academy of Sciences, 2016. **113**(20): p. 5622-5627.

109. Grimm, C., et al., *High susceptibility to fatty liver disease in two-pore channel 2-deficient mice.* Nature communications, 2014. **5**(1): p. 4699.

110. Tong, B.C.-K., et al., *Lysosomal TPCN (two pore segment channel) inhibition ameliorates beta-amyloid pathology and mitigates memory impairment in Alzheimer disease.* Autophagy, 2022. **18**(3): p. 624-642.

111. Hockey, L.N., et al., *Dysregulation of lysosomal morphology by pathogenic LRRK2 is corrected by TPC2 inhibition.* Journal of Cell Science, 2015. **128**(2): p. 232-238.

112. Yuan, Y., et al., *Segregated cation flux by TPC2 biases Ca2+ signaling through lysosomes.* Nature Communications, 2022. **13**(1): p. 4481.

113. Prat Castro, S., et al., *Neurodegenerative lysosomal storage disorders: TPC2 comes to the rescue!* Cells, 2022. **11**(18): p. 2807.

114. Lin-Moshier, Y., et al., *The Two-pore channel (TPC) interactome unmasks isoform-specific roles for TPCs in endolysosomal morphology and cell pigmentation.* Proceedings of the National Academy of Sciences, 2014. **111**(36): p. 13087-13092.

115. Krogsaeter, E.K., et al., *The protein interaction networks of mucolipins and two-pore channels.* Biochimica et Biophysica Acta (BBA) - Molecular Cell Research, 2019. **1866**(7): p. 1111-1123.

116. Cerny, J., et al., *The small chemical vacuolin‐1 inhibits Ca<sup>2+</sup>‐dependent lysosomal exocytosis but not cell resealing.* EMBO reports, 2004. **5**(9): p. 883-888.

117. Chen, C.-C., et al., *Patch-clamp technique to characterize ion channels in enlarged individual endolysosomes.* Nature Protocols, 2017. **12**(8): p. 1639-1658.

118. Ran, F.A., et al., *Genome engineering using the CRISPR-Cas9 system.* Nature protocols, 2013. **8**(11): p. 2281-2308.

119. Liu, L., et al., *Application of FRET biosensors in mechanobiology and mechanopharmacological screening.* Frontiers in Bioengineering and Biotechnology, 2020. **8**: p. 595497.

120. Fleige, S., et al., *Comparison of relative mRNA quantification models and the impact of RNA integrity in quantitative real-time RT-PCR.* Biotechnology letters, 2006. **28**: p. 1601-1613.

121. Thomas, P. and T.G. Smart, *HEK293 cell line: A vehicle for the expression of recombinant proteins.* Journal of Pharmacological and Toxicological Methods, 2005. **51**(3): p. 187-200.

122. Huynh, C. and N.W. Andrews, *The small chemical vacuolin-1 alters the morphology of lysosomes without inhibiting Ca2+-regulated exocytosis.* EMBO reports, 2005. **6**(9): p. 843-847.

123. Gayle, S., et al., *Identification of apilimod as a first-in-class PIKfyve kinase inhibitor for treatment of B-cell non-Hodgkin lymphoma.* Blood, The Journal of the American Society of Hematology, 2017. **129**(13): p. 1768-1778.

124. Wu, Y.-W., et al., *Membrane targeting mechanism of Rab GTPases elucidated by semisynthetic protein probes.* Nature Chemical Biology, 2010. **6**(7): p. 534-540.

125. Chao, Y.-K., et al., *TPC2 polymorphisms associated with a hair pigmentation phenotype in humans result in gain of channel function by independent mechanisms.* Proceedings of the National Academy of Sciences, 2017. **114**(41): p. E8595-E8602.

126. Oppelt, A., et al., *PIKfyve, MTMR3 and their product PtdIns5P regulate cancer cell migration and invasion through activation of Rac1.* Biochemical Journal, 2014. **461**(3): p. 383-390.

127. Compton, L.M., et al., *Active vacuolar H+ ATPase and functional cycle of Rab5 are required for the vacuolation defect triggered by PtdIns(3,5)P2 loss under PIKfyve or Vps34 deficiency.* American Journal of Physiology-Cell Physiology, 2016. **311**(3): p. C366-C377.

128. Tremel, S., et al., *Structural basis for VPS34 kinase activation by Rab1 and Rab5 on membranes.* Nature Communications, 2021. **12**(1): p. 1564.

129. Ikonomov, O.C., D. Sbrissa, and A. Shisheva, *Localized PtdIns 3,5-P2 synthesis to regulate early endosome dynamics and fusion.* American Journal of Physiology-Cell Physiology, 2006. **291**(2): p. C393-C404.

# 8 Appendix

## 8.1 Abbreviations

| | |
|---|---|
| µg | microgram |
| µL | microliter |
| µm | micromolar |
| ATP | Adenosine triphosphate |
| $A_{free}$ | free doner molecules |
| $Ca^{2+}$ | Calcium |
| $CaCl_2$ | Calcium Chloride |
| Cl | Chloride |
| CSCC | Cervical Squamous Cell Carcinoma |
| DMEM | dulbecco's modified eagle medium |
| DMSO | dimethylsulfoxide |
| EDTA | ethylenediaminetetraacetic acid |
| ED | doner FRET efficiency |
| EGTA | ethylene glycol tetraacetic acid |
| FRET | Föster resonance energy transfer |
| FBS | fetal bovine serum |
| GFP | green fluorescent protein |
| GAP | GTPase activating protein |
| GDI | GDP dissociation inhibitor |
| GDP | Guanosine diphosphate |
| GEF | Guanine nucleotide exchange factor |
| GTP | Guanosine triphosphate |

| | |
|---|---|
| GDI | GDP Dissociation inhibitor |
| GDF | GDI Displacement factor |
| GEF | guanine nucleotide exchange factor |
| GAP | GTPase-activating protein |
| H | hour |
| HCl | hydrochloric acid |
| HEK293 cell line | human embryonic kidney cells |
| $K^+$ | potassium |
| KO | knockout |
| LD | Longin domain |
| mg | milligram |
| mL | milliliter |
| mm | millimitter |
| min | minute |
| mV | millivoltage |
| mTq | mTurquoise2 |
| mVen | mVenus |
| MES | 2-(N-morpholino)ethanesulfonic acid |
| $Mg^{2+}$ | magnesium |
| MSA | methanesulfonate |
| MC1 | MON1-CCZ1 Complex |
| MCC | MON1-CCZ1-RMC1 Complex |
| MMP2 | matrix-metalloproteinase 2 |
| MMP17 | matrix-metalloproteinase 17 |
| $Na^+$ | sodium |

| | |
|---|---|
| NAADP | nicotinic acid adenine dinucleotide phosphate |
| NaCl | sodium chloride |
| NaOH | sodium hydroxide |
| pA | picoampere |
| Pen/strep | penicillin / streptomycin |
| pH | power of hydrogen |
| PI(3)P | Phosphatidylinositol 3 -phosphate |
| $PI(3,5)P_2$ | Phosphatidylinositol 3,5 -bisphosphate |
| $PI(4,5)P_2$ | Phosphatidylinositol 4,5 -bisphosphate |
| PI5-kinase | Phosphoinositide 5 -kinase |
| PIKfyve | FYVE finger -containing phosphoinositide kinase |
| PIP | phosphoinositide |
| Rpm | rotations per minute |
| REP | Rab Escort Protein |
| RabGGT | Rab Geranylgeranyl Transferase |
| TCA | tricyclic anti-depressant |

## 8.2 Chemicals

Unless otherwise specified, all reagents were procured from Sigma-Aldrich. The reagents were of 'ACS grade' or designated 'for molecular biology applications.' All solutions were prepared with ultrapure, deionized water (Millipore EQ700). For experiments requiring stringent purity, all solutions were sterilized by autoclaving.

Adenosine 5’-triphosphate (ATP) magnesium salt

Apilimod

Borate-Sodium tetraborate anhydrous

Boric acid $CaCl_2$-$2H_2O$

CaMSA

Complete protease inhibitor cocktail, EDTA-free (Roche, 04693132)

DMSO

Digitonin

Dulbecco´s modified Eagle medium (DMEM supplemented with 1 g/L glucose and pyruvate and Glutamax; Invitrogen, #21885-025)

Dulbecco's modified Eagle medium containing 25 mM glucose (DMEM supplemented with 4,5 g/L glucose and pyruvate and Glutamax; Invitrogen, #31966-021)

EGTA

Fetal bovine serum (FBS; Biochrom, #S0615)

Glucose

HCl

HEPES

KCl

KMSA

KOH

Methanesulfonic acid

NaCl

NaMSA

Pen-strep (penicillin 10,000 units/mL; streptomycin 10,000ug/mL; Biochrom)

Poly-L-Lysine hydrobromide

PBS

SG-094

PI(3,5)$P_2$-diC8 L-α-D-myo-Phowphatidylinositol 3,5-bisphosphate (A.G.Scientific)

TPC2-A1P

Vacuolin-1

## 8.3 Supplementary tables

Table 2: Primers used in qPCR

| | |
|---|---|
| TPC2_F | 5´-TGCATTGATCAGGCTGTGGT-3´ |
| TPC2_R | 5´-GAAGCTCAAAGTCCGTTGGC-3´ |
| ACTIN_F | 5´-TGCCGAGGATTTGGAAAAAGTG-3´ |
| ACTIN_R | 5´-TGGCCTCCCATCTCCTTCAT-3´ |

Table 3: sgRNA sequences

| | |
|---|---|
| $RNA_{CCZ1\text{-}1}$ | 5´-AAAGCACACAGCCGCACTCATGG-3´ |
| $RNA_{CCZ1\text{-}2}$ | 5´-CTTCGGCAAAAATCCAACGTTGG-3´ |
| $RNA_{RMC1}$ | 5´-TCGATCGAGCGGGAAGCACGGGG-3´ |

Table 4: Primers for validation of knockout cell lines

| | |
|---|---|
| *CCZ1*-F | 5´-TCACACCTGACAAGGTCAACA-3´ |
| *CCZ1*-R | 5´AGGACTGTTAATACCACCCGT-3´ |
| *RMC1*-F | 5´-GCAACTGGGCAAACC ATGAT-3´ |
| *RMC1*-R | 5´-GCCAAGATCACGACACTACCT-3´ |

# 9 Contributions

The following people contributed valuable knowledge to the present study and performed parts of experiments on a collaborative basis: FRET experiments (Figure 12A-b, Figure 13A-D, Figure 14A-F, Figure 16A-C, Figure 17A-E, Figure 20A-C, Figure 21A) were done in collaboration with Dr. Colin Feldmann and Prof. Dr. Christian Wahl-Schott (LMU Munich). Migration and proliferation assays (Figure 22D, 23A-B) were performed in collaboration with Lina Ouologuem and Dr. Kartin Bartel (LMU Munich). Alice Lin and Prof. Cheng-Chang Chen (NTU Taiwan) provided endolysosomal patch clamp experiments of Figure 19A and B.

# 10 Publications

1. Nagy, N.; Pal, M.; Kun, J.; Galik, B.; Urban, P.; Medvecz, M.; Fabos, B.; Neller, A.; Abdolreza, A.; Danis, J.; Szabo V.; **Yang Z.;** Fenske S.; Biel M.; et al**. Missing Heritability in Albinism: Deep Characterization of a Hungarian Albinism Cohort Raises the Possibility of the Digenic Genetic Background of the Disease.** Int. J. Mol. Sci. 2024, 25 (2), 1271.

2. Gibbs KD, Wang L, **Yang Z**, Anderson CE, Bourgeois JS, Cao Y, Gaggioli MR, Biel M, Puertollano R, Chen C-C, Ko DC. (2023). **Human variation impacting MCOLN2 restricts Salmonella Typhi replication by magnesium deprivation**. Cell Genomic 2023, 3 (5) :100290.

3. Li Y, Schön C, Chen CC, **Yang Z**, Liegl R, Murenu E, et al. **TPC2 promotes choroidal angiogenesis and inflammation in a mouse model of neovascular age-related macular degeneration**. Life Science Alliance (2021) 4(8). doi: 10.26508

## Presentations and Poster

Poster presentation at CRC/TRR 152 conference, 10/2022 in Homburg, Germany. “TPC2 promotes choroidal angiogenesis and inflammation in a mouse model of neovascular age-related macular degeneration” at CRC/TRR 152 conference.

Poster presentation at CRC/TRR 152 conference. 10/24 in München, Germany. “Ccz1 is essential for Rab7 dependent TPC2 channel activation” at CRC/TRR 152 conference.

# 11 Acknowledgements

First and foremost, I offer my deepest gratitude to **Prof. Dr. Martin Biel** for granting me the privilege of working in this remarkable research group. Your patience, trust, and unwavering encouragement over nearly six years have been a guiding light, especially in my darkest moments. Thank you for reminding me to stand proud and never surrender to the weight of doubt.

I am also greatly indebted to my former colleague, **Assist. Prof. Dr. Cheng-Chang Chen**, for illuminating the world of electrophysiology before my eyes. Your generosity with your time—despite the challenges of distance and time zones—never waned. I also extend heartfelt thanks to each and every colleague in the lab; your camaraderie, warmth, and shared enthusiasm turned my doctoral years into a joyous adventure rather than a solitary pursuit.

To my beloved wife and my parents, I owe an unrepayable debt for your boundless love and support. You bore with my frustrations, nourished me with comforting meals, and offered steadfast emotional shelter when I faltered. Your unconditional care carried me through the storms and helped me find my footing again and again.

Lastly, I wish to thank myself. Through every setback and tear, for every moment of resolve and each small triumph, I continued forward. Looking back now, I realize how these moments have shaped and strengthened me. This hard-earned growth will guide my future—both in my career and in the journey of personal discovery to come.